INVESTIGATION OF (PHOTO) ELECTROCATALYTIC CONVERSION OF DINITROGEN TO AMMONIA USING HYBRID PLASMONIC NANOSTRUCTURES

A Dissertation
Presented to
The Academic Faculty

By

Mohammadreza Nazemi

In Partial Fulfillment
of the Requirements for the Degree
Doctor of Philosophy in the
Woodruff School of Mechanical Engineering

Georgia Institute of Technology

May 2020

INVESTIGATION OF (PHOTO) ELECTROCATALYTIC CONVERSION OF DINITROGEN TO AMMONIA USING HYBRID PLASMONIC NANOSTRUCTURES

Approved by:

Dr. Mostafa A. El-Sayed, Advisor
School of Chemistry and Biochemistry
Georgia Institute of Technology

Dr. Todd A. Sulchek, Co-Advisor
Woodruff School of Mechanical Engineering
Georgia Institute of Technology

Dr. Younan Xia
School of Chemistry and Biochemistry
Georgia Institute of Technology

Dr. Paul A. Kohl
School of Chemical and Biomolecular Engineering
Georgia Institute of Technology

Dr. Ting Zhu
Woodruff School of Mechanical Engineering
Georgia Institute of Technology

Dr. Matthew T. McDowell
Woodruff School of Mechanical Engineering
Georgia Institute of Technology

Date Approved: March 9, 2020

A failure is not always a mistake. It may simply be the best one can do under the circumstances. The real mistake is to stop trying.

B.F. Skinner

ACKNOWLEDGEMENTS

I wish to take this opportunity to thank all those who have made a contribution to this work and without their help, I would not have been able to finish my Ph.D.

First and for most, I sincerely acknowledge my lovely advisor, Prof. Mostafa El-Sayed who kindly adopted me into his group and provided me with an excellent opportunity to pursue my projects of interest under his guidance and support. He not only taught me how to be a great scientist (of course, I cannot be such a fantastic scientist like him) but also taught me invaluable lessons during enjoyable conversations we had over the lunch or dinner in which I undoubtedly leverage them in my personal life. I am very grateful for all your advice and honored to be your 113th Ph.D. graduate in your long-lasting academic career. The legacy you have left for the scientific community is unbelievable and I am proud that I had this privilege to work with you and I can truly take you as my inspirational role model when I start my independent career.

I would like to greatly thank Prof. Todd Sulchek for accepting to be my co-advisor in the school of Mechanical Engineering. Without his help and positive attitude, I would not have been able to work in the school of Chemistry while being a graduate student in Mechanical Engineering. I would also like to thank his graduate student, Alan Liu for performing AFM measurements of our nanoparticles.

I am very thankful to my prominent committee members, Prof. Younan Xia, Prof. Paul Kohl, Prof. Ting Zhu, and Prof. Matthew McDowell for accepting to be in my thesis committee and for their scientific feedback on my Ph.D. research. In addition, it has been a pleasure for me to take Prof. Kohl's electrochemistry class, which ignited my interest in this field of research and also he kindly accepted me to take my teaching practicum on the same class with him. I really take it as a favor that he allowed me to teach a few lectures in his class and I am very grateful for that.

I acknowledge all of my friends and colleagues at the Laser Dynamics Laboratory. Most no-

tably, I am very thankful to Dr. Sajanlal Panikkanvalappil, who helped me to get started relatively quickly after joining the lab and teaching me how to synthesize plasmonic nanoparticles of various types and shapes. I am also very thankful to our collaborators including Prof. Meilin Liu and his graduate students Luke Soule and Ali Abdelhafiz, Prof. Vladimir Tsukruk and his graduate students Jing Zhou and Shuaidi Zhang and his postdoc, Dr. Saewon Kang.

I greatly acknowledge all staff members at the Institute for Electronics and Nanotechnology at Georgia Tech. Particularly noteworthy, I thank Walter Henderson, Eric Woods, Todd Walters, David Tavakoli, Rathy Monikandan, Dr. Yong Ding. Their guidance and support to operate all instruments were incredible which enabled me to get meaningful results in a timely manner. I also thank Dr. Leslie Gelbaum for helping me with NMR measurements and Ms. Tabassum Shah for performing ICPES measurements.

I am very grateful to our lab administrative support, Michele Yager for not only making sure our administrative work is always running smoothly without any delay but also has always been available to hear from me and give me her best advice. I would also like to thank Mike Riley for his assistance in making sure our lab is safe and functional.

During my Ph.D., I had the privilege to work with a great team of MBA (Pete Nicolay, Ian Schubert, and Michael Luo) and JD students (Amanda Guarisco, Aaron Savit) on my TIGER fellowship. I truly enjoyed interacting with all of you while we were working on the commercialization of my Ph.D. Technology. I am extremely grateful to our wonderful team mentors, Mr. Jonathan Goldman, Prof. Jonathan Giuliano, Prof. Nicole Morris, Prof. Robert Gemmell, and our industry mentor, Mr. Trevor Brown. You were all incredibly supportive and patient enough to walk us through various steps in the Tech to market process.

Last but not least, I would like to thank my family, especially my mother and father for their endless love, support, and guidance in the last almost seven years that I have been 7,000 miles away from them and did not get a chance to visit them even once. I hope I have made you proud and continue to do so. I would like to dedicate this dissertation to you.

TABLE OF CONTENTS

Acknowledgments iv

List of Tables ix

List of Figures xi

Chapter 1: Introduction, Background, and Motivation 1

1.1 Nanocatalysis using Metallic and Semiconductor Nanoparticles 1

1.2 Ammonia as a Medium for Intermittent Renewable Energy Storage 4

Chapter 2: Hollow Gold Plasmonic Nanoparticles for Electrochemical Ammonia Synthesis 9

2.1 Introduction 9

2.2 Experimental Methods 10

2.2.1 Nanoparticle Synthesis 10

2.2.2 Electrochemical Measurement 12

2.2.3 Ammonia quatification Measurements 13

2.2.4 Ammonia Faradaic Efficiency 13

2.2.5 Calculation of Nanoparticle Concentration 13

2.3 Results and Discussion 15

2.4 Conclusion 24

Chapter 3: Pore-size Controlled Hollow gold nanocages with tunable plasmonic properties for Ammonia Electrosynthesis 25

3.1 Introduction 25

3.2 Experimental Methods 25

3.2.1 Nanoparticle Synthesis 25

3.2.2 Determination of the Electrochemical Surface Area (ECSA) of the nanoparticle 26

3.3 Results and Discussion 27

3.4 Conclusion 37

Chapter 4: The Role of Oxidation of Silver in Bimetallic Gold-Silver Nanocages on Electrocatalytic Activity of Nitrogen Reduction Reaction 39

4.1 Introduction 39

4.2 Experimental Methods 39

4.2.1 Nanoparticle synthesis 39

4.2.2 Electrochemical Measurement 40

4.3 Results and Discussion 40

4.4 Conclusion 48

Chapter 5: The role of incorporating palladium in bimetallic Gold-Silver nanocages on Electrocatalytic Activity of Nitrogen Reduction Reaction 49

5.1 Introduction 49

5.2 Experimental Methods 51

5.2.1 Nanoparticle Synthesis 51

5.2.2 Production Energy Efficiency Calculation 51

5.2.3 Determination of the Electrochemical Surface Area (ECSA) of the Nanoparticle . . . 52

5.2.4 Turnover Frequency Calculation . . . 52

5.2.5 *Operando* Surface Enhanced Raman Spectroscopy (SERS) measurements . . . 54

5.3 Results and Discussion . . . 54

5.4 Conclusion . . . 70

Chapter 6: Plasmon-Enhanced photosynthesis of Ammonia using visible light responsive hybrid hollow plasmonic nanocages . . . 72

6.1 Introduction . . . 72

6.2 Experimental Methods . . . 75

6.2.1 Photochemical Nitrogen Reduction . . . 75

6.2.2 Photoelectrochemical Measurements . . . 77

6.2.3 Determination of Valence Band Energy Level (E_{VBM}) and Band Gap Energy (E_g) . . . 78

6.3 Results and Discussion . . . 79

6.4 Conclusion . . . 94

Chapter 7: Future Outlook . . . 95

Appendix A: Chemicals and Materials . . . 99

Appendix B: Instrumentation . . . 100

References . . . 114

LIST OF TABLES

3.1 Au, Ag concentrations, Au and Ag content (% at.) of nanoparticles are determined by inductively coupled plasma emission spectroscopy (ICPES). The electrochemical surface areas (ECSA) of nanoparticles are determined based on the reduction peak of Au oxide during cyclic voltammetry measurement in Ar-saturated 0.1M LiOH solution at a scan rate of 50 mV s^{-1}. Atomic content is calculated using Au and Ag concentrations divided by the molar mass of Au (196.97 g mol^{-1}) and Ag (107.87 g mol^{-1}). 30

3.2 Selectivity performance of AuHNCs with various LSPR peak values toward NRR 32

3.3 Electrochemical performance of NRR using AuHNCs-715 with various pH electrolytes at -0.4V vs. RHE. 35

4.1 Au, Ag concentrations, Au content (mass % and atomic %) of various hybrid hollow plasmonic nanoparticles that are determined by inductively coupled plasma emission spectroscopy (ICPES) and their corresponding LSPR peak position. Atomic content (at. %) is calculated using Au and Ag concentrations divided by the molar mass of Au (196.97 g mol^{-1}) and Ag (107.87 g mol^{-1}). 42

4.2 The shell composition of nanocages with various LSPR peak positions determined by EDX spectroscopy. 42

4.3 Selectivity performance of hybrid plasmonic nanoparticles with various LSPR peak positions toward NRR. 45

5.1 Au, Ag, and Pd concentrations of nanoparticles are determined by inductively coupled plasma emission spectroscopy (ICPES). The electrochemical surface areas (ECSA) of nanoparticles are determined based on the reduction peak of Au oxide and Pd oxide during CV measurements in Ar-saturated 0.1M LiOH solution at a scan rate of 50 mV s^{-1}. 57

5.2 Selectivity performance of trimetallic Au-Ag-Pd nanoparticles with LSPR peak positions at 750 nm and 850 nm toward NRR. 61

6.1 Au, Ag concentrations, Au content (mass % and at. %) of various type of nanoparticles (solid vs. hollow) and their corresponding LSPR peak position and transient photocurrent response. 81

6.2 The photocatalytic activity of Ag_2O-Au-685 photocatalyst after 2h illumination under full solar spectrum, visible light, and 685 nm bandpass filter with 15 nm FWHM. 86

LIST OF FIGURES

1.1 TEM images of single metal and bimetallic nanoparticles consist of Ag, Au, Pd, and/or Pt with various shapes. Silver nanocubes (AgNCs), gold nanospheres (AuNSs), gold nanocubes (AuNCs), gold-palladium nanocubes (AuPdNCs), hollow gold nanocages (AuHNCs), gold nanorods (AuNRs), gold-platinum nanorods (AuPtNRs), and gold-palladium nanorods (AuPdNRs) are among others presented here. 2

1.2 Schematic diagram of (photo) electrochemical systems for value-added chemicals production with various applications in energy and agriculture. 5

1.3 Background of various electrochemical approaches for nitrogen fixation in the literature. 7

1.4 Background of various photochemical approaches for nitrogen fixation in the literature. 8

2.1 A) UV-vis extinction spectra of the AgNCs and AuHNCs, the photograph shown in the inset is AuHNCs dispersed in DI water. B) XRD pattern of AuHNCs deposited on Si substrate. C) and D) are the TEM images of AuHNCs with different magnifications. The average edge length of the AuHNCs is 35 nm. 16

2.2 A) Schematic of electrochemical cell for NRR. The anode and cathode compartments are separated by a cation exchange membrane (CEM). B) Linear sweep voltammetry tests in an Ar and N_2 saturated environment in 0.5M $LiClO_4$ aqueous solution under ambient conditions. C) Ammonia yield rate and Faradaic efficiency at various potentials in 0.5M $LiClO_4$ at 20^{o}C, D) Cycling stability results of ammonia yield rate on AuHNCs. For each cycle CA test was carried out at -0.4V vs. RHE in 0.5M $LiClO_4$ at 20^{o}C. 18

2.3 A) UV-vis calibration curve for ammonia quantification using Nessler's method. Known concentration of ammonium ions are added to 0.5M $LiClO_4$ electrolyte and mixed thoroughly with 1 mL of 0.2M $KNaC_4H_6O_6$ and 1 mL of Nessler reagent and then the absorbance at 395 nm is measured by the UV-vis spectrophotometer. The value of blank electrolyte is subtracted from all other concentrations as background. 19

2.4 A) UV-vis absorption spectrum of AuHNCs in 0.5M $LiClO_4$ aqueous solution under N_2 saturated with and without applied potential and Ar gas with applied potential (-0.4V vs. RHE). B) Raman spectra of blank 0.5 M $LiClO_4$ aqueous solution, NRR sample, and standard NH_4^+ sample. C) Calibration curve of the ^{1}H NMR signal at 6.95 ppm for standard solutions of NH_4^+ (100, 150, 1000 μM) and NRR sample. D) ^{1}H NMR spectra (700 MHz) of NH_4^+ produced from the NRR experiment and standard NH_4^+ samples. ^{14}N produces a triplet with $\sim$52 Hz J coupling constant. 20

2.5 A) Ammonia yield rate and Faradaic efficiency of AuHNCs at various concentrations at -0.5V vs. RHE in 0.5M $LiClO_4$ aqueous solution under ambient conditions. B) Ammonia yield rate and Faradaic efficiency of AuHNCs at various temperatures at -0.4V vs. RHE in 0.5M $LiClO_4$ aqueous solution. 22

2.6 A) UV-vis extinction spectra of AuNSs, AuNCs, and AuNRs, B), C), and D) are the TEM images of AuNSs, AuNRs, and AuNCs, respectively. E) Ammonia yield rate and Faradaic efficiency for nanoparticles of various types and shapes at the potential of -0.4V vs. RHE in 0.5M $LiClO_4$ aqueous solution. 23

3.1 A) UV-vis extinction spectra of AgNCs and AuHNCs with various LSPR peak values, the photograph shown in the inset is AuHNCs dispersed in DI water. B), C), and D) are the TEM images of AuHNCs with LSPR peak values at 635nm, 715nm, and 795nm, respectively. The inset of each image is the magnified TEM image of a nanoparticle. 28

3.2 Cyclic voltammograms (CV) of AuHNCs with various peak LSPR values in Ar-saturated 0.1M LiOH aqueous solution at a scan rate of 50 mV s^{-1}. The CV measurements were conducted in the rotating disk electrode (RDE) setup at a rotation rate of 1500 rpm at room temperature. The observed shift in decreasing the reduction potential of Au oxide ($\sim$0.15V) when LSPR redshifts from 635 nm to 795 nm is attributed to the de-alloying process by removal of Ag in the cavity. The second peak in the reduction segment of the CV curve corresponds to the reduction of Ag oxide. The intensity of the peak is proportional to the Ag concentration which is the highest for AuHNCs-715. 29

3.3 A) Linear sweep voltammetry (LSV) tests of AuHNCs with LSPR peak values at 635nm, 715nm, and 795nm in an Ar and N_2 saturated 0.5 M $LiClO_4$ (aq.) under ambient conditions with the scan rate of 10 mV s^{-1}. B) Chronoamperometry (CA) results of AuHNCs with various LSPR peaks at -0.4 V vs. RHE in N_2 saturated 0.5M $LiClO_4$ (aq.). C) Ammonia yield rate and Faradaic efficiency for AuHNCs with various LSPR peak values at the potential of -0.4 V vs. RHE in 0.5M $LiClO_4$ (aq.). D) UV-vis absorption spectra of N_2 and Ar saturated 0.5 M $LiClO_4$ (aq.) after electrolysis at -0.4V vs. RHE for 12 h using Nessler's test for AuHNCs with various LSPR peak values. 31

3.4 A) UV-vis extinction spectra of AgNSs and AuHNSs with various LSPR peak values. B), C), and D) are the TEM images of AuHNSs with the LSPR peak values at 635nm, 715nm, and 795nm, respectively. The average diameter of nanoparticles is 55 nm. 33

3.5 Ammonia yield rate and Faradaic efficiency for AuHNSs with various LSPR peak values at the potential of -0.4V vs. RHE in 0.5M $LiClO_4$ (aq.). 34

3.6 A) Chronoamperometry (CA) results of AuHNCs-715 nm at a series of potentials. B) Ammonia yield rate and Faradaic efficiency at various potentials in 0.5M $LiClO_4$ (aq.). C) CA tests for the stability of the AuHNCs-715 nm at -0.4V vs. RHE in 0.5M $LiClO_4$ (aq.). For each cycle a CA test was carried out at -0.4V vs. RHE for 12 h. D) Cycling stability results of ammonia yield rate and Faradaic efficiency on AuHNCs-715 nm. For each cycle a CA test was carried out at -0.4V vs. RHE in 0.5M $LiClO_4$ (aq.). . . 35

3.7 The SEM images A) before and B) after the durability test. The electrode after the test was thoroughly washed with DI water and dried at room temperature before taking the measurement. 36

4.1 A) UV-vis extinction spectra of bimetallic Au-Ag nanocages with various LSPR peak positions before and after O_2 treatment. Before O_2 treatment, the bimetallic Au-Ag nanoparticles have the LSPR peak positions at 635 nm and 715 nm while after O_2 treatment the LSPR redshifts to 644 nm and 719 nm, suggesting the formation of Ag_2O in the cavity (Ag_2O-Au). B) SERS spectra of Ag_2O, Ag_2O-Au-685, and Ag-Au-670 nanoparticles. The TEM images of bimetallic Au-Ag nanocages with the LSPR peak position C) at 635 nm before O_2 treatment (Au-Ag-635) and D) at 644 nm after O_2 treatment (Ag_2O-Au-644). The TEM images of bimetallic Au-Ag nanocages with the LSPR peak position E) at 715 nm before O_2 treatment (Au-Ag-715) and F) at 719 nm after O_2 treatment (Ag_2O-Au-719). 41

4.2 A) HRTEM and STEM images of A) Ag-Au-635, B) Ag_2O-Au-644, C) Ag-Au-715, and D) Ag_2O-Au-719 nanocages. 43

4.3 A) Cyclic voltammograms (CV) of Ag_2O-Au nanocages with various LSPR peak positions in Ar-saturated 0.1M LiOH (aq.) solution at a scan rate of 50 mV s^{-1}. The CV measurements were conducted in the rotating disk electrode (RDE) setup at room temperature. B) Linear sweep voltammetry (LSV) tests of Ag_2O-Au with LSPR peak positions at 644nm and 719nm in an Ar and N_2 saturated 0.5 M $LiClO_4$ (aq.) solution under ambient conditions with the scan rate of 10 mV s^{-1}. 44

4.4 A) UV-vis extinction spectra of AgNCs before and after O_2 treatment. B) O 1s profiles of Ag nanocubes before and after O_2 treatment. All spectra were shift corrected using a standard reference C1s, C-C peak at 284.8 eV. C) Mott-Schottky plot of Ag_2O. A Mott-Schottky plot at a frequency of 1000 Hz was measured in 0.5 M $LiClO_4$ (aq.) solution under the dark condition. D) The TEM image of solid Ag_2O nanocubes. 46

4.5 A) Ammonia yield rate and FE for bimetallic Au-Ag nanocages before and after O_2 treatment with various LSPR peak positions at a potential of -0.4 V vs RHE in 0.5 M $LiClO_4$ (aq.) solution. B) Ammonia yield rate and FE at various applied potentials in a 0.5 M $LiClO_4$ (aq.) solution. 47

5.1 A) UV-vis extinction spectra of silver nanocubes, bimetallic Au-Ag nanocages, and trimetallic Au-Ag-Pd nanoparticles with the LSPR peak positions at 750 nm and 850 nm. TEM images of B) Au-Ag-650, C) Au-Ag-Pd-750, and D) Au-Ag-Pd-850. Silver nanocubes with the LSPR peak position at 412 nm are used as a template to synthesize various bimetallic and trimetallic nanoparticles. 55

5.2 STEM (A), HRTEM (B), and EDX elemental mapping (C, D, E, F) of a representative single Au-Ag-Pd-750 nanoparticle. STEM (G), HRTEM (H), and EDX elemental mapping (I, J, K, L) of a representative single Au-Ag-Pd-850 nanoparticle. 56

5.3 XPS spectra of A) Au 4f, B) Ag 3d, and C) Pd 3d of Au-Ag-Pd-850 nanoparticles. All spectra were shift corrected using a standard reference C1s, C-C peak at 284.8 eV. D) XRD pattern of Au-Ag and Au-Ag-Pd nanocages. The Pd diffraction peaks shift to higher 2θ angles due to the smaller lattice parameter (3.890 Å) compared to those of the Au (4.079 Å) and Ag (4.086 Å). 58

5.4 A) Cyclic voltammograms (CV) of Au-Ag-Pd-750 and Au-Ag-Pd-850 in Ar-saturated 0.1M LiOH (aq.) at a scan rate of 50 mV s^{-1}. The CV measurements were conducted in the rotating disk electrode (RDE) setup at the stagnant electrode condition at room temperature. B) Linear sweep voltammograms (LSV) of various catalysts in N_2-saturated 0.5 $LiClO_4$ (aq.). C) LSV tests of Au-Ag-Pd-750 and Au-Ag-Pd-850 in an Ar- and N_2-saturated 0.5 M $LiClO_4$ (aq.) under ambient conditions with the scan rate of 10 mV s^{-1}. 60

5.5 A) CA results of Au-Ag-Pd-750 and Au-Ag-Pd-850 nanocatalysts at a series of potentials. B) Ammonia yield rate and Faradaic efficiency at various potentials in 0.5 M $LiClO_4$ (aq.) solution using Au-Ag-Pd-750 and Au-Ag-Pd-850 nanocatalysts. C) Production energy efficiency and energy input at various applied potentials using Au-Ag-Pd-750 and Au-Ag-Pd-850 nanocatalysts. The intense bars (black bars show production energy efficiency and blue bars show energy input) represent Au-Ag-Pd-750 and the medium bars represent Au-Ag-Pd-850. D) CA test for the stability of the Au-Ag-Pd-850 at -0.4V vs. RHE in 0.5 M $LiClO_4$ (aq.) solution. E) 1H-NMR spectra of samples after electrochemical $^{15}N_2$ ($^{14}N_2$) reduction reaction at -0.4V vs. RHE for 4 h in 0.5M $LiClO_4$ (aq.) solution. 63

5.6 A) UPS spectra of trimetallic Au-Ag-Pd nanoparticles. A) The secondary electron cut-off ($E_{cut\text{-}off}$) and B) the Fermi edge (E_{FE}) are measured with He1 (21.22 eV) source radiation. The work function (ϕ) is calculated by 21.21 eV – ($E_{cut\text{-}off}$ – E_{FE}). The ϕ of Au-Ag-Pd-750 and Au-Ag-Pd-850 nanoparticles are determined to be 4.45 and 3.73 eV. 64

5.7 A) UV-vis absorption spectra of 0.5 M $LiClO_4$ (aq.) solution after electrolysis at -0.4V vs. RHE for 12 h using Au-Ag-Pd-850 nanoparticles obtained with indophenol blue method in various operating conditions (i.e., N_2, Ar, N_2 at OCV, N_2 with no catalyst). B) UV-vis absorption spectra of 0.5 M $LiClO_4$ (aq.) solution after electrochemical NRR with $^{14}N_2$ and $^{15}N_2$ at -0.4 V vs. RHE for 4 h. C) UV-vis absorption spectrum of 0.5 M $LiClO_4$ (aq.) solution after 72 h stability test at -0.4 V vs. RHE. 65

5.8 A) The TEM images A) before and B) after the electrocatalytic NRR stability test (72 h at -0.4V vs. RHE in 0.5M $LiClO_4$ (aq.) solution). 66

5.9 A) Schematic of the spectroelectrochemical setup for operando SERS measurements. B) CV curves of Au-Ag-Pd-850 in Ar- and N_2-saturated 0.5M $LiClO_4$ (aq.) solution at the scan rate of 2.5 mV s^{-1}. During the oxidation segment in Ar-saturated electrolyte, a strong peak centered on 0.3 V corresponds to the oxidation of hydrogen. This peak with the lower intensity and slight positive potential shift is also observed in N_2-saturated electrolyte. In addition, a new peak at around 0.05 V is observed in N_2-saturated electrolyte which might be attributed to the oxidation of N-containing species. . 67

5.10 A) *Operando* SERS using Au-Ag-Pd-850 nanoparticles in N_2-saturated 0.5M $LiClO_4$ (aq.) solution at the scan rate of 2.5 mV s^{-1} with 532 nm laser. B) *Operando* SERS using Au-Ag-Pd-850 nanoparticles in Ar-saturated 0.5M $LiClO_4$ (aq.) solution at the scan rate of 2.5 mV s^{-1} with 532 nm laser. C) and D) Low and high Raman shift of SERS spectra in N_2-saturated electrolyte (Figure 5.10A). 68

5.11 A) SERS spectrum of the standard ammonia solution (30 μM NH_4^+) in 0.5M $LiClO_4$ (aq.) solution. B) SERS spectrum of the standard hydrazine solution (60 μM N_2H_4 (aq.)) in 0.5M $LiClO_4$ (aq.) solution. 69

6.1 UV-vis extinction spectra of Ag_2O-Au nanocages with various LSPR peak values. B), C), and D) are the TEM images of Ag_2O-Au nanocages with LSPR peak values at 655nm, 685 nm, and 715 nm, respectively. As the LSPR peak redshifts from 655 nm to 715 nm, the pore size at the wall and corner of the nanocages increases. E) HR-TEM image of Ag_2O-Au with the LSPR peak value at 685 nm, the inset shows the Fast Fourier Transform (FFT) of the nanoparticle, confirming the formation of Ag_2O after oxygen treatment. F) Lattice spacing of Ag_2O (2.23 Å) and Au (2.68 Å) in the Ag_2O-Au-685 nanoparticle obtained from HRTEM. 80

6.2 A) XPS survey spectra, B) XPS spectra of Au 4f, C) Ag 3d, and D) O1s for Ag_2O, Ag_2O-Au, and Ag-Au nanoparticles. All spectra were shift corrected using a standard reference C1s, C-C peak at 284.8 eV. 82

6.3 A) Electronic band structure of Ag_2O and Ag_2O-Au photocatalysts for nitrogen reduction reaction B) Schematic of photochemical cell for NRR. C) Ammonia yield and solar-to-ammonia (STA) efficiency of various photocatalysts under one sun illumination for 2 h in a N_2 saturated pure water. D) Ammonia yield of Ag_2O-Au-685 under various operating conditions over 24 h. E) Ammonia yield for photocatalysts with various LSPR peak values before (Ag-Au) and after (Ag_2O-Au) oxygen treatment. F) Stability test of Ag_2O-Au-685 photoelectrode for ammonia production. Five consecutive tests are carried out for the period of 8 h (total 40 h) using Ag_2O-Au-685 photoelectrode. The electrolyte solution was replaced before starting each cycle. 83

6.4 UPS spectra of Ag_2O nanocubes and Ag_2O-Au nanocages. The UPS spectra of A) the secondary electron edge and B) the valance bands are measured with He1 (21.22 eV) source radiation. C) and D) Bandgap determination of Ag_2O nanocubes and Ag_2O-Au nanocages using Kubelka-Munk theory. 84

6.5 TEM images of Ag_2O-Au-685 nanocages A) before and B) after the stability test in the photocatalytic reaction. XPS spectra of Ag_2O-Au-685 photocatalyst before and after the stability test. C) XPS survey spectra, D) XPS spectra of O 1s, E) Au 4f, and F) Ag 3d. All spectra were shift corrected using a standard reference C1s, C-C peak at 284.8 eV. 88

6.6 Transient photocurrent response of Ag_2O-Au with various LSPR peak values. B) Transient photocurrent response of Ag_2O-Au-685 in N_2 and Ar saturated 0.5M $LiClO_4$ (aq.) solution under 1 sun illumination. Photocurent responses are measured at the open circuit voltage of the cell. C) Photoluminescence spectra of Ag_2O and Ag_2O-Au-685 photocatalysts. Both samples were excited with 375 nm excitation source. D) Nyquist plots of the Ag_2O-Au-685 under photoirradiation at an applied potential of 0.5 V (vs Ag/AgCl) in 0.5M $LiClO_4$ (aq.) solution. The equivalent circuit model in the inset comprises charge transfer resistance (R_{CT}), double layer capacitance (C_{DL}), and ohmic resistance (R_S). R_{CT} was obtained from the diameter of semicircles for each photocatalyst. 90

6.7 The schematic of the photoelectrochemical setup for performing transient photocurrent and EIS measurements. The electrolyte is N_2- or Ar-saturated 0.5M $LiClO_4$ (aq.) solution. Pt counter electrode and Ag/AgCl reference electrode were used for measurements. The light source is 300 W Xe lamp with one sun illumination intensity (100 mW cm^{-2}). 91

6.8 A) ^{1}H NMR spectra for the standard $^{14}NH_4^+$ solutions with various concentrations. B) Peak area calibration curve of the ^{1}H NMR signal at 6.93 ppm for standard solutions of $^{14}NH_4^+$ (25, 50, 75 μM). C) ^{1}H NMR spectra for the standard $^{15}NH_4^+$ solutions with various concentrations. D) Peak area calibration curve of the ^{1}H NMR signal at 6.97 ppm for standard solutions of $^{15}NH_4^+$ (25, 50, 75 μM). All peak areas were normalized to the DMSO-d^6 area peak at 2.49 ppm. 92

6.9 ^{1}H NMR spectra of samples after photochemical $^{15}N_2$ ($^{14}N_2$) reduction reaction under 1-sun illumination for 4 h using Ag_2O-Au-685 nanocages and standard $^{15}NH_4^+$ and $^{14}NH_4^+$ samples. 93

7.1 Input electricity cost for making one ton of green ammonia as a function of renewable electricity price. The input natural gas cost for making a ton of ammonia in the Haber-Bosch process is relatively constant and is about 150 dollars while for green ammonia there is a substantial room to decrease the renewable electricity price and therefore be cost competitive with the Haber-Bosch process. 96

SUMMARY

Meeting our future global energy needs in an environmentally responsible way is one of the most significant challenges in the twenty-first century. Currently, fossil fuels such as oil, gas, and coal satisfy more than 80% of the global energy demand. This results in more than 35 billion metric tons of carbon dioxide (CO_2) emission annually. It is imperative to harvest renewable energy sources (e.g., solar, wind) to serve as a way to diversify from traditional fossil fuels for combatting the environmental challenges associated with greenhouse gases. Due to the intermittent nature of renewable energy sources, the development of a cost-effective and sustainable method of storing this vast amount of energy on an industrial scale when supply exceeds demand in the grid is an urgent need. As the cost of renewably derived electricity continues to decrease given the rapid progress in technology and economies of scale, there is a growing interest in fuels and chemicals electrosynthesis. The thrust of my Ph.D. research has focused on developing novel electrochemical technologies to use renewable electricity as an energetic driving force to convert low energy molecules (N_2) to high value-added molecules (NH_3) that can be utilized as either fuels, energy storage molecules, and/or chemicals.

(photo) electrochemical nitrogen reduction reaction (NRR) for ammonia synthesis provides an attractive alternative to the long-lasting thermochemical process (Haber-Bosch) in a clean, sustainable, and decentralized way if the process is coupled to renewably derived electricity sources. In addition to ammonia's widespread utility as a precursor for making fertilizer, ammonia also holds great promise as a carbon-neutral liquid fuel for storing intermittent renewable energy sources as well as for power generation due to the compound's high energy density (5.6 MWh ton^{-1}) and hydrogen content (17.6 wt.%). Electrification of ammonia synthesis on a large scale requires an effective electrocatalyst that converts N_2 to NH_3 with a high yield and efficiency. The selectivity of N_2 molecules on the surface of the catalyst has been demonstrated to be one of the major challenges in enhancing the rate

of photo-electrochemical NRR in aqueous solution under ambient conditions. The rational design of electrode-electrolyte in the context of photo-electrochemical systems is required to overcome the selectivity and activity barrier in NRR.

The scientific thrusts of this Ph.D. dissertation to address a critical obstacle to achieving the overarching goal of distributed ammonia synthesis are as follows:

Thrust 1: Materials chemistry for the synthesis of a range of heterogeneous (photo) electrocatalysts including plasmonic and hybrid plasmonic-semiconductor nanostructures for selective and efficient conversion of N_2 to NH_3.

Thrust 2: Novel reactor design to study the redox processes in the photo-electrochemical energy conversion system and to benchmark nanocatalysts' selectivity and activity toward NRR.

Thrust 3: Performing *ex-situ* and *operando* spectroscopy, including surface-enhanced Raman spectroscopy (SERS) to probe the reaction mechanism and to identify intermediate species relevant to NRR at the electrode-electrolyte interface. In addition, nuclear magnetic resonance (NMR) spectroscopy measurements is carried out to quantify the trace amount of products after the catalytic reaction and to distinguish $^{15}NH_4^+$ from $^{14}NH_4^+$ in isotopic labeling experiments using $^{15}N_2$.

The outcomes of this dissertation generate an integrated scientific framework, combining materials chemistry, photo-electrochemistry, and spectroscopy to overcome the challenges associated with renewable energy storage and transport. It also contributes to future electrification, decarbonization, and sustainability of modern chemical industry.

CHAPTER 1

INTRODUCTION, BACKGROUND, AND MOTIVATION

1.1 Nanocatalysis using Metallic and Semiconductor Nanoparticles

Nanocatalysis has attracted great attention in the past two decades both in homogeneous solution-phase colloidal reactions and in heterogeneous supported nanoparticle gas-phase reactions. Nanoparticles are characterized by a high surface-to-volume ratio; resulting in an increase their efficiency in catalysis [1, 2, 3, 4, 5, 6]. Introducing sharp corners, edges as well as defect sites to the nanocatalysts further increase their catalytic efficiency [7]. Since the activity of the nanocatalyst depends on the number of high energy active centers [8], atoms located at the sharp tips are thermodynamically and catalytically more active because they are unsaturated in their chemical valency (i.e., atoms that do not have the complete number of bonds that they can chemically accommodate to act as active sites than smoother nanoparticles) [6, 9, 10, 11]. Sharp tips are prone to be rounded during the catalytic reactions. This causes a remarkable decrease in their efficacy. The shape change of the particles could be due to leaching or rearrangement of the surface atoms [9, 12]. There are two main categories of nanoparticles: solid and hollow. In nanocatalysis by solid nanoparticles, the catalytic reaction happens by involving the atoms from the surface of the nanocatalyst, while for hollow nanocatalysts the reaction takes place at the outer and/or the inner surfaces of the nanocatalyst. Therefore, the reaction could be accelerated in hollow nanocatalyst due to the higher surface area. Reactions using the hollow nanocatalyst could be assisted by several factors. First, the confinement of reactants within the cavity could increase the steady-state concentration of the species in the rate-determining step of the reaction, and second, in some cases, the inner surface might not be as well capped as the outer surface and thus be more catalytically active. Therefore, the rate of the reaction

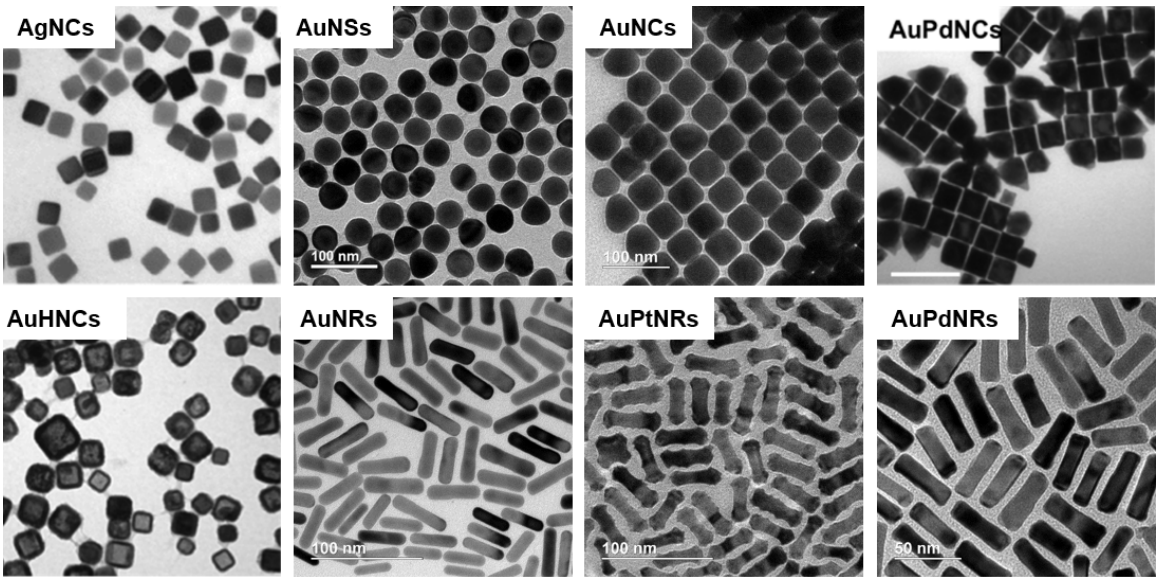

Figure 1.1: TEM images of single metal and bimetallic nanoparticles consist of Ag, Au, Pd, and/or Pt with various shapes. Silver nanocubes (AgNCs), gold nanospheres (AuNSs), gold nanocubes (AuNCs), gold-palladium nanocubes (AuPdNCs), hollow gold nanocages (AuHNCs), gold nanorods (AuNRs), gold-platinum nanorods (AuPtNRs), and gold-palladium nanorods (AuPdNRs) are among others presented here.

increases due to the cage effect. Since the wall thickness of the nanoreactor is small (a few nanometers), the electron can transfer across the wall during catalysis of electron transfer reactions. The surface to volume ratio of the hollow nanocatalyst is higher than any solid nanocatalysts, because the surface area of the cavity adds to the outer surface area of the nanocatalyst. This is another factor enhancing the catalytic properties of the hollow nanoparticles [13]. Although catalysis of nanoparticles has many advantages, there are still some drawbacks associated with the development of this type of nanocatalysts that has to be addressed. The reshaping of nanocatalysts during catalytic reaction, products deposition on the nanocatalyst surface, and capping materials on the surface of colloidal nanocatalyst could decrease nanocatalyst stability, activity, limit their recyclability, affect their fermi energy, and results in aggregation of nanocatalysts.

The galvanic replacement technique developed by Sun and Xia has allowed the synthesis of hollow metallic nanoparticles of various shapes [5]. Confinement of reacting materials within the hollow nanocatalysts has been demonstrated to enhance the catalytic

efficiency of various chemical reactions [14, 15, 13, 16, 17, 18]. This confinement is acquired either by designing the nanocatalyst to have a cavity, or by fixing the catalyst on the surface of the interior wall of an inert support. Nanocage catalysts made of a single metal (e.g., gold, platinum, or palladium) or two metals in a double shell arrangement have shown high catalytic efficiency due to the cage effect [14, 15, 13]. The idea of cage effect in catalysis was supported by comparing the catalytic activity of gold nanocages with that of the solid nanocatalysts of similar shapes [19, 20] (**Fig. 1.1**). To understand the mechanism of catalysis using hollow nanoparticles, two types of hollow nanocages with double shells, one with platinum around palladium and the other with palladium around platinum, and two single-shelled nanocages of platinum and palladium were synthesized [14]. The kinetic parameters (i.e., rate constant of the reaction, activation energy, entropy of activation, and frequency factor) of each double-shelled catalyst were comparable to those of the single-shelled nanocage of the same metal as the inside shell, indicating the reactions are taking place within the cavity. In addition, during catalysis using double shelled hollow nanoparticles with an inner surface made of gold plasmonic metal and a non-plasmonic outer layer of platinum, as the reaction proceeded and the dielectric function of the interior gold cavity changed, the plasmonic band of the interior gold shell shifted. This strongly suggested that the reaction had taken place primarily in the cavity [15]. The cage effect was also observed for palladium nanotubes, which showed a high catalytic efficiency for the Suzuki reaction [17]. Additionally, silver oxide prepared *in situ* on the interior wall of gold nanocages showed high photocatalytic activity for the decomposition of an organic dye as the reactive radicals were confined within the gold nanocage catalysts [21]. Gold nanoparticles encapsulated in silica nanospheres catalyzed the production of hydrogen from formic acid [22]. Nanocatalysts fixed on the inner wall of porous metal-organic frameworks (MOFs) showed high catalytic activity due to the confinement of the reactant inside the voids present in the structure of the MOFs [23]. Polymer nanofibers when used as a support for platinum and ruthenium nanocatalysts showed high catalytic efficiency due

to the cage effect [24]. Nickel, cobalt, iron, and their respective oxides encapsulated inside SiO_2 nanoshells effectively catalyzed reaction while maintaining thermal stability [25]. High electrocatalytic efficiency was also observed in hybrid inorganic nanostructures such as ruthenium and Cu_2S due to their electronic properties [26]. The kinetic parameters including the rate constant of the reaction, entropy of activation, and frequency factor for a nanocatalytic reaction are controlled by the following factors: i) the concentration of the nanocatalyst and reacting materials. ii) the number of successful collisions with the surface of the nanocatalyst in the rate determining step. iii) the electronic structure of the nanocatalyst including the d-band center which regulates the binding strength of adsorbates with the catalyst surface. iv) the active surface area of the nanocatalyst and and the reaction conditions (e.g., temperature and pressure). Due to the small size of nanocatalysts, which in some cases approaches the size of the reacting materials, the catalytic mechanisms are not clearly understood. Heterogeneous catalysis is possible when the reaction takes place on the surface of the nanocatalyst, while a homogeneous mechanism occurs when the catalysis proceeds through the formation of a complex between dissolved surface atoms in solution. Understanding these mechanisms would be greatly aided by determining which species were present on the nanoparticle surface during catalysis. Raman spectroscopy presents fingerprint vibrational spectra for molecules. Plasmonic nanoparticles can greatly enhance Raman signals through their enhancement of the electromagnetic fields of resonant light. This technique, known as surface-enhanced Raman spectroscopy (SERS), is sensitive down to the zeptomolar range (10^{-21}) [27]. The high sensitivity of SERS has made it possible to use this technique to probe catalytic reaction as it occurs on the surface of the plasmonic nanocatalyst [28, 29].

1.2 Ammonia as a Medium for Intermittent Renewable Energy Storage

Ammonia is one of the most widely produced commodities in the world, with 146 million tons being produced globally in 2015 with an estimated increase in production of 3-5%

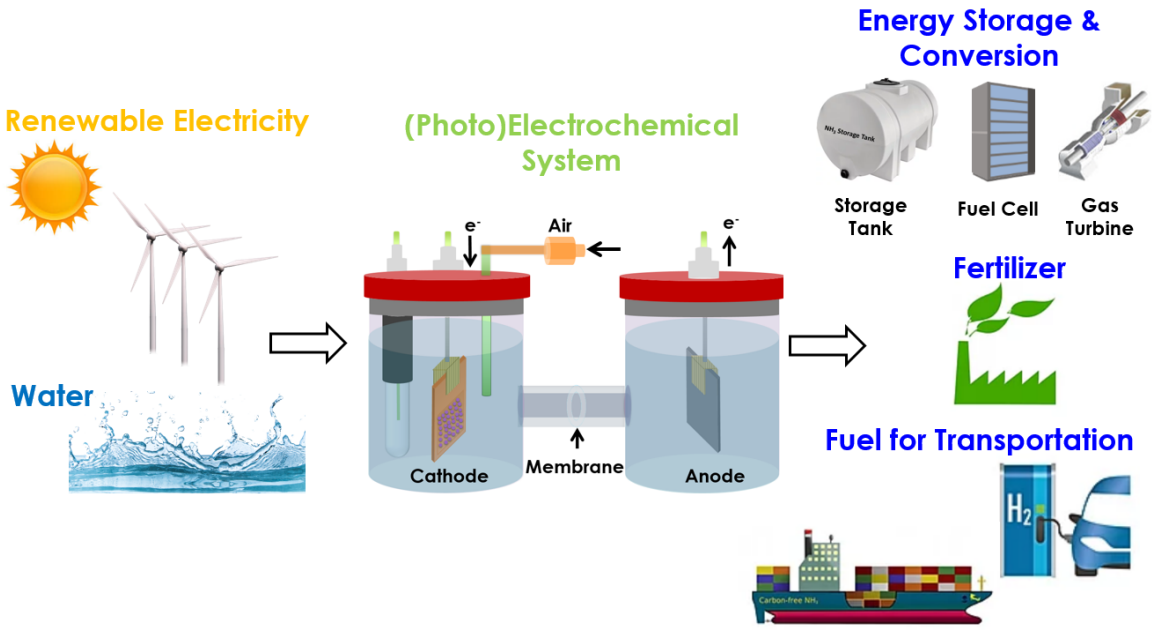

Figure 1.2: Schematic diagram of (photo) electrochemical systems for value-added chemicals production with various applications in energy and agriculture.

per year [30, 31]. Ammonia is used in numerous applications, most notably as a vital agrochemical and as a precursor for pharmaceutical products [32]. In addition to the compound's widespread utility, ammonia also holds great promise as a carbon-neutral liquid fuel for storing intermittent renewable energy sources when supply exceeds demand in the grid as well as for power generation due to the compound's high energy density and hydrogen content [33, 34]. Ammonia can be used directly in alkaline fuel cells (AFCs) or indirectly as an H_2 source in proton exchange membrane fuel cells (PEMFCs). Ammonia can be a substitute for H_2 as a combustion fuel with superior advantages in terms of energy density, ease of liquefaction, and high hydrogen content (for example, the hydrogen content in liquid ammonia is 17.6% by weight compared with 12.5% for methanol). The volumetric energy density of ammonia is 13.6 GJ m^{-3} ($\sim$10 atm at 298 K), which is compared with 5.3 GJ m^{-3} for hydrogen at 700 bar pressure [35]. Thus, sustainable nitrogen fixation lies at the nexus of food and energy chemistry (**Fig. 1.2**).

Conventional ammonia synthesis mainly relies on the Haber-Bosch process, which converts N_2 and H_2 to NH_3 at high operating pressures (150-250 bar) and temperatures (350-

550°C) over iron-based catalysts [30]. The extreme condition requirements for this process necessitate high cost demands for centralized infrastructure that should be coupled with the global distribution system. Additionally, this process consumes 3-5% of the global natural gas supply and 60% of global hydrogen production and emits 450 million metric tons of CO_2 annually [36].This mandates an alternative approach for sustainable and scalable ammonia synthesis under ambient conditions that can alleviate extreme condition requirements.

As the cost of renewably derived (e.g., solar and wind) electricity continues to decrease given the rapid progress in technology and economies of scale, there is a growing interest in NH_3 electrosynthesis from N_2 and H_2O under ambient conditions in an electrochemical cell [37]. Electrocatalytic fixation of nitrogen is a form of artificial synthesis that mimics the natural nitrogen enzymatic process [38]. This approach can provide an alternative pathway to the Haber-Bosch process for clean, sustainable, and distributed ammonia synthesis as well as the storage of surplus renewable energy in the form of NH_3 fuel at times of excess supply in the grid [39, 40]. Electrification of ammonia synthesis in a large scale requires an effective electrocatalyst that converts N_2 to NH_3 with a high yield and Faradaic efficiency (FE). To date, most studies have shown low electrocatalytic activity and selectivity for NH_3 production mainly due to the high energy required for N≡N cleavage and due to the competition with the hydrogen evolution reaction (HER) [41, 42, 43, 44, 45]. Furthermore, the use of molten salt systems and the electrochemical lithium cycling strategy aid in increasing the ammonia yield and FE; however, these strategies are not energetically efficient and usually require high temperatures (e.g., 450°C) [46, 47] (**Fig. 1.3** and **Fig. 1.4**). The selectivity of N_2 molecules on the surface of nanocatalysts over the kinetically favored hydrogen evolution reaction (HER) has been demonstrated to be one of the major challenges in enhancing the rate of electrochemical nitrogen reduction reaction (NRR) in aqueous solution under ambient conditions [48, 49]. In addition, achieving high ammonia yield rate is vital to make this process industrially feasible. Achieving high production energy

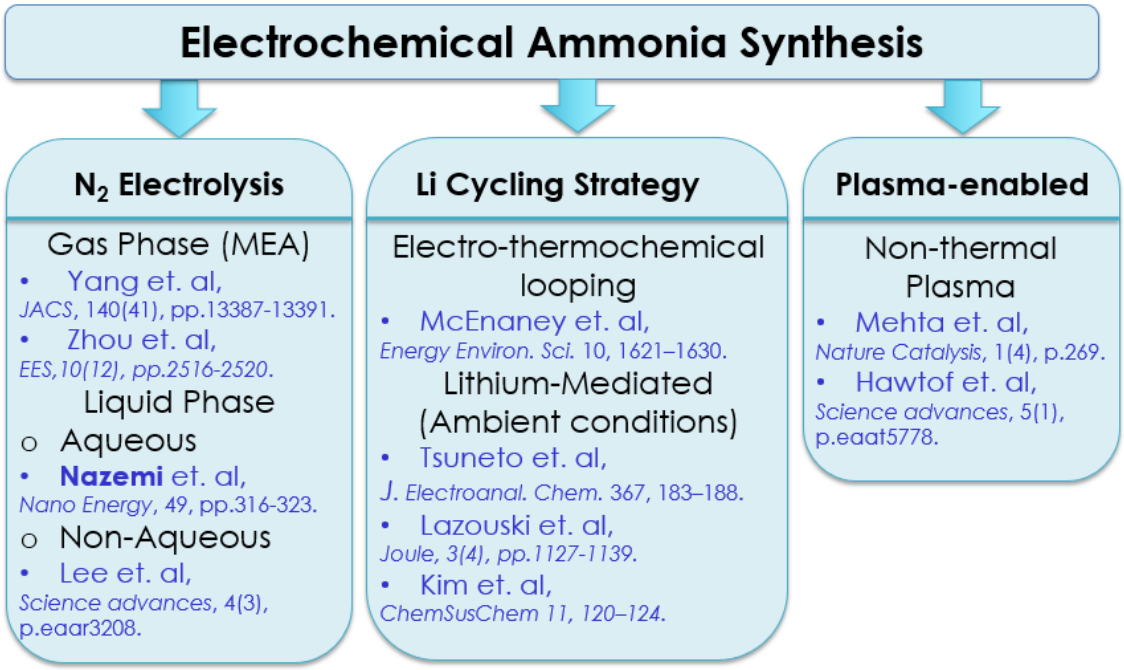

Figure 1.3: Background of various electrochemical approaches for nitrogen fixation in the literature.

efficiency (maintaining low overpotentials for the anodic and cathodic half reactions) is another important factor needs to be addressed [50]. It is important to note that while plasma electrolytic systems result in remarkably high N_2 selectivity and ammonia formation rate, it suffers from a very low energy conversion efficiency as a result of a high voltage input (i.e., 500 V) [51].

In the following chapters, the electrocatalytic activity of hollow Au plasmonic nanoparticles and solid Au plasmonic nanoparticles of various shapes (e.g., spheres, cubes, rods) for ammonia synthesis from N_2 and H_2O in an ionic aqueous solution under ambient and near ambient condtitions will be presented (Chapter 2). I further demonstrate the use of shape and pore-size controlled Au and bimetallic Au-Ag nanocages, with tunable localized surface plasmon resonance (LSPR) peak positions, as electrocatalysts for ammonia synthesis (Chapter 3). The role of oxidation of Ag in bimetallic Au-Ag nanocages on the rate of electrocatalytic conversion of N_2 to NH_3 will be discussed (Chapter 4). The photocatalytic activity of hybrid plasmonic-semiconductor nanostructures (i.e., Au-Ag_2O) for

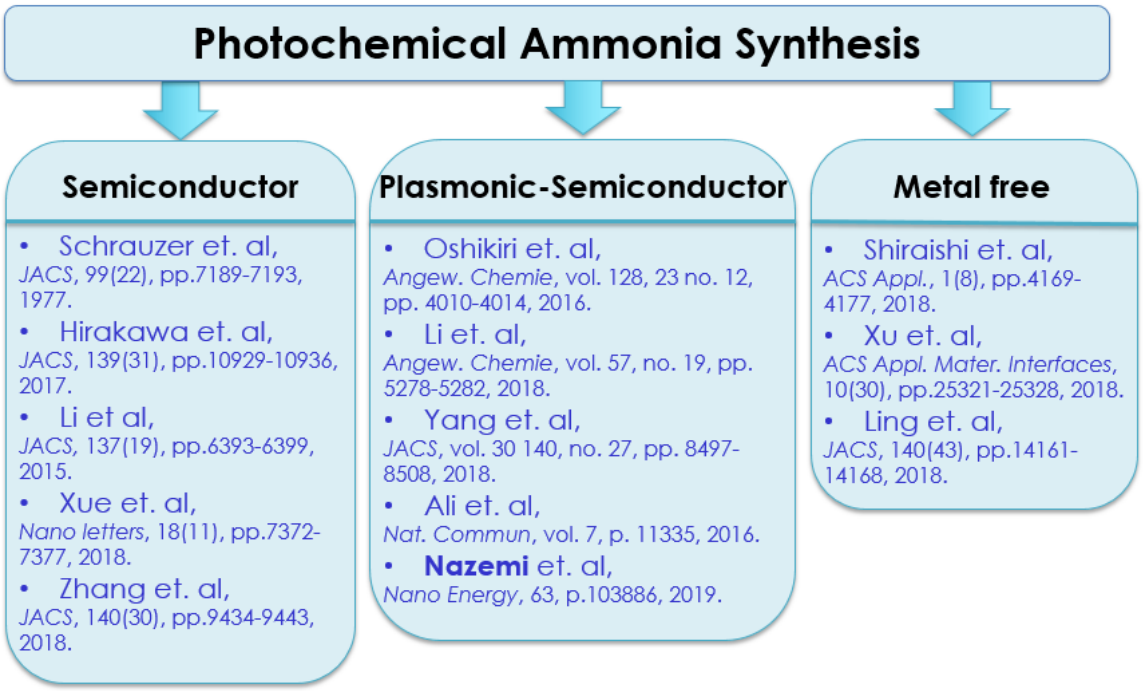

Figure 1.4: Background of various photochemical approaches for nitrogen fixation in the literature.

ammonia synthesis will be presented (Chapter 5). The role of incorporating palladium (Pd) in bimetallic Au-Ag nanocages on the electrocatalytic activity of the nitrogen reduction reaction (NRR) under ambient conditions will be discerned. Furthermore, *operando* surface-enhanced Raman spectroscopy (SERS) is used to probe the mechanism of NRR on the trimetallic nanostructures and to identify the intermediate species at the electrode-electrolyte interface (Chapter 6). Finally, conclusion and suggestions for future work will be discussed (Chapter 7). The chemical mechanisms and physical phenomena that enable photocatalytic and electrocatalytic conversion of nitrogen molecules to ammonia will be discerned in detail. One of the main aims of this dissertation is to investigate the mechanistic role of hollow nanoparticles by preparing and characterizing a variety of hybrid plasmonic nanocatalysts with semiconductors and catalytic metals using the plasmonic enhancing properties and surface-enhanced Raman Spectroscopy (SERS) to carefully monitor the mechanisms involved during the catalytic reaction.

CHAPTER 2

HOLLOW GOLD PLASMONIC NANOPARTICLES FOR ELECTROCHEMICAL AMMONIA SYNTHESIS

2.1 Introduction

Developing sustainable and environmentally friendly ammonia production methods that consume significantly less energy than the current industrial process is imperative. The use of nanocatalysis in an electrochemical system under ambient conditions can make an alternative route for ammonia production. An efficient catalyst should bond atoms and molecules with an intermediate strength so that catalysis will not be limited by weak adsoprtion of reactants or strong desorption of products. Gold (Au) has been known as one of the best catalysts for the electrochemical NRR through an associative mechanism where breaking of the triple bond of N_2 and hydrogenation of the N atoms occur simultaneously [52, 53]. It has been shown that N_2 adsorbs on the Au surface with further hydrogenation to form adsorbed N_2H_x species ($1 < x < 4$), where the rate determining step is N_2 dissociation (reduction of N_2^* to form NNH^*) [52, 53, 54]. Here, I aim to enhance the rate of electrochemical NRR under ambient conditions, notably using hollow Au nanocages (AuHNCs) as an effective electrocatalyst. The catalytic efficiency of AuHNCs are compared with similar concentrations of solid Au nanocubes (AuNCs), nanospheres (AuNSs), and nanorods (AuNRs) to prove that the enhanced rate of NRR using hollow nanocages is due to the increased surface area and the confinement of reactants in the cavity (cage effect).

2.2 Experimental Methods

2.2.1 Nanoparticle Synthesis

Synthesis of AgNC and AuHNC

Hollow gold nanoparticles with cubic shape are prepared by the galvanic replacement method using cubic silver nanoparticles as a template. Silver nanocubes (AgNCs) are prepared by a modified polyol reduction of $AgNO_3$. In a 100 mL round-bottomed flask, 35 mL of anhydrous ethylene glycol (EG) is stirred at 400 rpm and heated at 150^{o}C for 1 h in an oil bath. After 1 h heating of the EG, 0.35 gr of polyvinylpyrrolidone (PVP, MW 55000) dissolved in 5 mL EG is added at once to the reaction mixture. The temperature of the reaction mixture is then increased gradually until it reaches 155^{o}C. At this temperature, 0.4 mL of 3 mM solution of sodium sulfide ($Na_2S.9H_2O$) in EG is added 5 min after the addition of PVP. The solution of sodium sulfide must be prepared an hour before injection into the reaction mixture. Finally, 0.25 g of $AgNO_3$ dissolved in 5 mL of EG is added at once with stirring set to 200 rpm until the color changes from brownish yellow to pale yellow. Then the stirring and heating are stopped and the solution temperature is allowed to decrease to room temperature. To clean the AgNCs solution from the byproducts, extra PVP, and organic solvents, 20 mL of the AgNCs solution is diluted with 20 mL of acetone and centrifuged for 10 min at 10,000 rpm. The precipitated AgNCs are dispersed in the solution of 0.01 g PVP dissolved in 100 mL of DI water. To prepare AuHNCs, the cleaned AgNCs solution in DI water is heated and brought to boiling. Then, HAuCl4 (0.2 g L^{-1}) in DI water is injected to the AgNC solution under vigorous stirring (600 rpm) until the peak LSPR spectrum of the solution shifts to 660 nm. The solution is refluxed for 2 min with stirring until the LSPR remains fixed. The solution is cooled down and centrifuged at 10,000 rpm for 10 min. The precipitated nanoparticles are dispersed in DI water for future use.

Synthesis of AuNSs

AuNSs are prepared by the reduction of $HAuCl_4.3H_2O$ using PVP (MW 10,000) that acts as both a capping and a reducing agent. In a 150 mL flask, 100 mL of 0.085 mM $HAuCl_4$ in DI water is heated and brought to boiling. Under 500 rpm stirring, 0.65 g PVP is added. The reaction is allowed to proceed until the solution turns to red color and the LSPR peak becomes narrow. The solution is cooled down and centrifuged at 10,000 rpm for 10 min. The precipitated nanoparticles are dispersed in DI water for future use.

Synthesis of AuNCs

AuNCs are prepared using a modified surfactant-directed seed-mediated approach [55]. The seed particles are prepared using 7.75 mL of solution containing 7.50 mL of 0.1M cetyltrimethylammonium bromide (CTAB) and 0.25 mL of 0.01M $HAuCl_4$ in DI water. Next, 0.6 mL of an ice cold 0.01M $NaBH_4$ solution is added to the initial solution for the subsequent reduction of gold ions. The resulting solution is stirred for 2 min and remains undisturbed for an hour before use. The seed solution is then diluted 10 times with DI water. To prepare the growth solution, 4 mL of DI water, 0.8 mL of 0.1M CTAB, and 0.1 mL of 0.01 M $HAuCl_4$ are mixed thoroughly. A 0.6 mL of 0.1M ascorbic acid is added to the growth solution and mixed thoroughly until the solution turns colorless. Finally, 2.5 μL of the diluted seed solution is added to the growth solution and the reaction vessel is allowed to sit overnight. The AuNCs are centrifuged two times at 10,000 rpm for 10 min. The precipitated AuNCs are dispered in DI water for future use.

Synthesis of AuNRs

AuNRs are synthesized by the modified seed-mediated protocol [56]. Briefly, the seed nanoparticles are prepared by adding 0.25 mL of $HAuCl_4$ (0.01 M) to 7 mL of CTAB (0.1 M) followed by the addition of 0.01 M of ice-cold $NaBH_4$ (0.6 mL) solution in DI water. This solution is stirred for 2 min and left undisturbed for 1 h. In the subsequent step, 1 mL

of seed solution is added to the growth solution, which is prepared by mixing 100 mL of CTAB (0.1 M) with 4.25 mL of $HAuCl_4$ (0.01 M), 0.625 mL of $AgNO_3$ (0.01 M), and 0.675 mL of ascorbic acid (0.1 M). After the addition of the seed solution, the entire solution is kept undisturbed for 12 h. The resultant AuNRs are purified by centrifugation (10,000 rpm for 10 min) and redispersion in DI water.

2.2.2 Electrochemical Measurement

In order to prepare a working electrode (cathode), 300 μL of nanoparticles of known concentration and 1.5 μL of nafion solution (5% wt.) were sonicated and dropcasted onto a indium tin oxide (ITO) (1cm$\times$1cm) and then dried under N_2 atmosphere at 75^{o}C for 45 min. Electrochemical measurements were carried out at 20^{o}C, 35^{o}C, and 50^{o}C in the water bath in 0.5M $LiClO_4$ electrolyte (40 mL, each side) using a CHI instrument potentiostat (CHI, 700D) in the three-electrode setup. Pt mesh (1cm$\times$1cm) and Ag/AgCl reference electrode (3M, BASi, USA) were used as counter and reference electrodes. CEM was used to separate the anodic and cathodic compartments while protons produced at the anode can transport across the membrane to the cathode side where NRR occurs. The measured potentials vs. Ag/AgCl are IR-compensated and converted to the reversible hydrogen electrode (RHE) scale based on the following equation 2.1:

$$E_{RHE} = E_{Ag/AgCl} + \frac{2.3RT}{F}pH + E^o_{Ag/AgCl} \tag{2.1}$$

where E_{RHE} is the converted potential vs. RHE, $E^o_{Ag/AgCl}$=0.2027 at 20^{o}C with the slope of -1.01 $mV/^oC$, $E_{Ag/AgCl}$ is the experimentally measured potential against Ag/AgCl reference electrode, R is the gas constant (8.314 J mol^{-1} K^{-1}), and T is the operating temperature (K). The electrolyte is fed with N_2 or Ar gas for 2 h before starting the measurement at the flow rate of 20 mL min^{-1}.

2.2.3 Ammonia quatification Measurements

The quantity of ammonia is determined via a colorimetric method using Nessler reagent. In order to obtain the calibration curve, a known volume of the standard ammonia solution is added to the tube. Next, the tube is filled with 0.5M $LiClO_4$ electrolyte until the total volume reaches 10 mL. Then, 1 mL of 0.2M potassium sodium tartrate in DI water is added to each of the tubes. Finally, 1 mL of Nessler reagent is added to each of the tubes and mixed thoroughly. The tubes are kept undisturbed for 20 min for color development and then the absorbance at 395 nm is measured using an Ocean optics spectrophotometer (HR4000Cg-UV-NIR). The absorbance for the blank sample without adding standard NH_3 solution is subtracted from all samples for background correction.

2.2.4 Ammonia Faradaic Efficiency

To calculate the ammonia Faradaic efficiency, the amount of ammonia produced during the experiment is divided by the total charge applied to the electrodes. Based on this reaction ($N_2 + 6H^+ + 6e^- \rightarrow 2NH_3$), three electrons are required to produce one mole of NH_3. The Faradaic efficiency is calculated according to the following equation 2.2:

$$FE_{NH_3}(\%) = \frac{C \times V}{(i \times t)/(n \times F)} \tag{2.2}$$

where C is the ammonia concentration (mol L^{-1}), V is the volume of the electrolyte (0.04 L), i is the measured current (A), n is the number of electrons that is required to produce one mole of ammonia (eq.mol^{-1}), and F is the Faraday's constant (96485 C eq^{-1} or A.S eq^{-1}).

2.2.5 Calculation of Nanoparticle Concentration

The molar concentration of each nanoparticle (C) is determined by dividing the total number of gold atoms (N_{total}) in the sample over the average number of gold atoms per nanopar-

ticle (N) according to the following equation 2.3:

$$C = \frac{N_{total}}{NVN_A} \tag{2.3}$$

where V is the volume of the sample, and N_A is the Avogadro's constant (6.022×10^{23} mol^{-1}). The concentration of nanoparticles is measured using inductively coupled plasma emission spectroscopy (ICP-ES). The weight of the nanoparticle is determined from the high resolution TEM image. To calculate N, the mass of each nanoparticle (ρV$'$) is divided to the mass of one gold atom (M) based on the following equation 2.4

$$N = \frac{\rho V'}{M} \tag{2.4}$$

where ρ is the density of Au atom (19.3×10^{-21} g/nm^3), V' is the volume of each nanoparticle, and M is the mass of one gold atom, which is the ratio of the molecular weight of Au (197 g mol^{-1}) and Avogadro's constant.

$$Mass\ of\ one\ gold\ atom\ (M) = \frac{197\ g\ mol^{-1}}{6.022 \times 10^{-23}\ atom\ mol^{-1}} = 3.27 \times 10^{-22} \frac{g}{Au\ atom} \tag{2.5}$$

To calculate the mass of each nanoparticle, the diameter of nanoparticle is determined from the TEM image. For instance, the average diameter of Au nanospheres (AuNSs) is 35 nm. Therefore the mass of the nanosphere is calculated by multiplying the volume of the nanosphere (πd^3/6) and the density of Au according to equation 2.6

$$Mass\ of\ AuNS = 19.3 \times\ 10^{-21} \frac{g}{nm^3} \times \pi\ \times\ \frac{35^3}{6} = 4.33 \times\ 10^{-16}\ g \tag{2.6}$$

Then, the number of Au atoms per nanoparticle is calculated by dividing Equation 2.5 and 2.6:

$$N = \frac{Mass\ of\ AuNS}{Mass\ of\ one\ gold\ atom} = \frac{4.33 \times 10^{-16}\ g}{3.27 \times 10^{-22}\ \frac{g}{Au\ atom}} = 1324989.119\ Au\ atom \quad (2.7)$$

Finally, the value of Au concentration obtained from ICP-ES (e.g., for AuNSs: 8.28 mg L^{-1}) is divided by the average number of Au atoms per nanoparticle to determine the concentration of nanoparticles in the sample, which gives ∼32 pM.

2.3 Results and Discussion

AuHNCs are prepared from a silver solid nanocube (AgNC) template by the galvanic replacement technique [5, 57]. In this method the sacrificial metal template (i.e., Ag) is replaced with the nanocage metal (i.e., Au) if the oxidation potential of the metal template is higher than that of the nanocage metal. The replacement of three Ag atoms of the template with one Au atom ($3Ag(s) + AuCl_4^-(aq.) \rightarrow Au(s) + 3Ag^+(aq.) + 4Cl^-(aq.)$) creates a hollow structure with holes at the wall and corners of the nanocage. The size of the AuHNCs is tuned by varying the size of the AgNCs. AgNCs with localized surface plasmon resonance (LSPR) peak position at 429 nm are prepared by a modified polyol reduction method (Figure 1A). The AgNCs are then washed with acetone, centrifuged (10,000 rpm, 10 min) and dispersed in DI water. Hydrogen tetrachloroaurate (0.5 mM) in DI water is injected into the AgNC solution under vigorous stirring (600 rpm) until the LSPR peak position shifts to 660 nm (**Figure 2.1A**). The X-ray diffraction (XRD) pattern of AuHNCs deposited on the Si substrate is composed of various surface index facets that provide active sites for electrochemical NRR (**Figure 2.1B**). The average edge length of AuHNCs is 35 nm, obtained from transmission electron microscopy (TEM) analysis (**Figure 2.1C and D**). Electrochemical NRR experiments are conducted in H-type cells where anodic and cathodic compartments are separated by a proton conductive cation exchange mem-

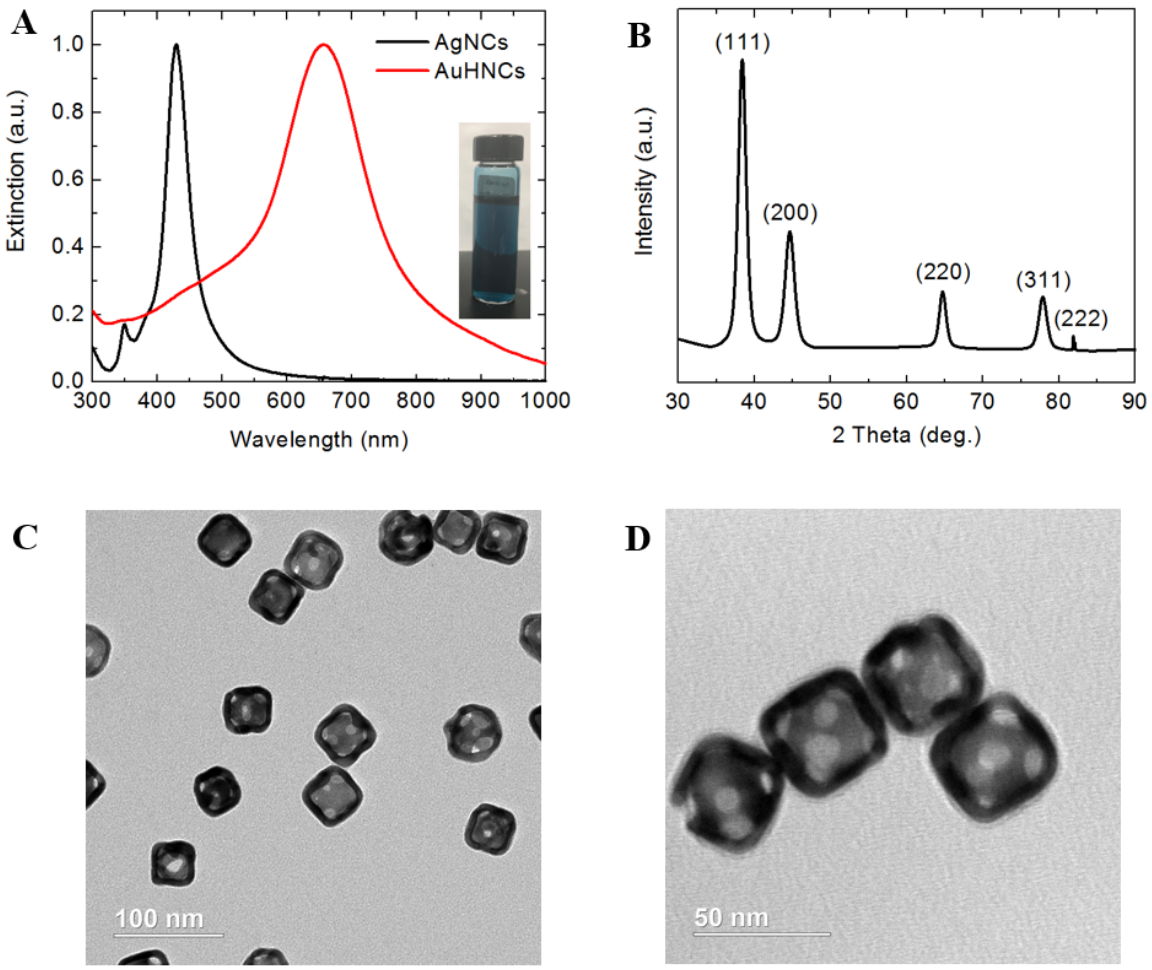

Figure 2.1: A) UV-vis extinction spectra of the AgNCs and AuHNCs, the photograph shown in the inset is AuHNCs dispersed in DI water. B) XRD pattern of AuHNCs deposited on Si substrate. C) and D) are the TEM images of AuHNCs with different magnifications. The average edge length of the AuHNCs is 35 nm.

brane (**Figure 2.2A**). The electrolyte is 0.5M $LiClO_4$ aqueous solution. Perchlorate anion (ClO_4^-) is selected for NRR due to the minimal and unselective adsorption of the ClO_4^- on the low index facets of Au nanoparticles surface [58]. Li^+ is selected for its superior ability to activate N_2 at ambient conditions [43, 47]. The primary reaction at the anodic compartment is:

$$3H_2O \rightarrow \frac{3}{2}O_2 + 6H^+ + 6e^- \tag{2.8}$$

where water is oxidized to produce oxygen gas and protons (H^+). The protons produced at the anode are transported through the proton conductive membrane to the cathode part

where supplied N_2 gas and protons will produce NH_3:

$$N_2 + 6H^+ + 6e^- \rightarrow 2NH_3 \tag{2.9}$$

The overall reaction is:

$$N_2 + 3H_2O \rightarrow 2NH_3 + \frac{3}{2}O_2 \tag{2.10}$$

Linear sweep voltammetry (LSV) tests are performed in an Ar and N_2 saturated environment to qualitatively distinguish between HER and NRR (**Figure 2.2B**). As the potential moves below -0.4V vs. RHE, a notable enhancement in current density is observed under the N_2 saturated environment. This is attributed to the reaction between AuHNCs as a cathodic electrocatalyst and N_2 to produce NH_3. The greatest difference in the LSV curves of N_2 and Ar saturated environments is found at the potential between -0.4V to -0.8V vs. RHE, at which it is expected that the highest NRR activity in this potential range will be achieved. Moving toward potentials more negative than -0.8V vs. RHE yields no further difference in current density between Ar and N_2 (**Figure 2.2B**). This indicates that HER is the only reaction at the cathode. Chronoamperometry (CA) tests at a series of potentials are conducted to determine the ammonia yield rate and Faradaic efficiency. The calibration curve for the ammonia assay using the Nessler reagent is shown in **Figure 2.3**. The electrochemical NRR obtains higher selectivity within the potential range of -0.4V to -0.6V vs. RHE, with the highest ammonia yield rate (3.98 μg cm^{-2} h^{-1}) at -0.5V and Faradaic efficiency (30.2%) at -0.4V. Although in this potential range (-0.4V to -0.6V), the ammonia yield rate increases as the negative applied potential increases, Faradaic efficiency decreases, which is attributed to the compromise between increasing current density and competitive selectivity toward HER rather than NRR. It is known that H atoms occupy the active sites on Au that prevents N_2 adsorption and reduction on the catalytic surface [52, 59]. At negative applied potential below -0.6V, both ammonia yield rate and Faradaic efficiency decrease considerably (ammonia yield rate: 1.54 μg cm^{-2} h^{-1}, Faradaic efficiency:

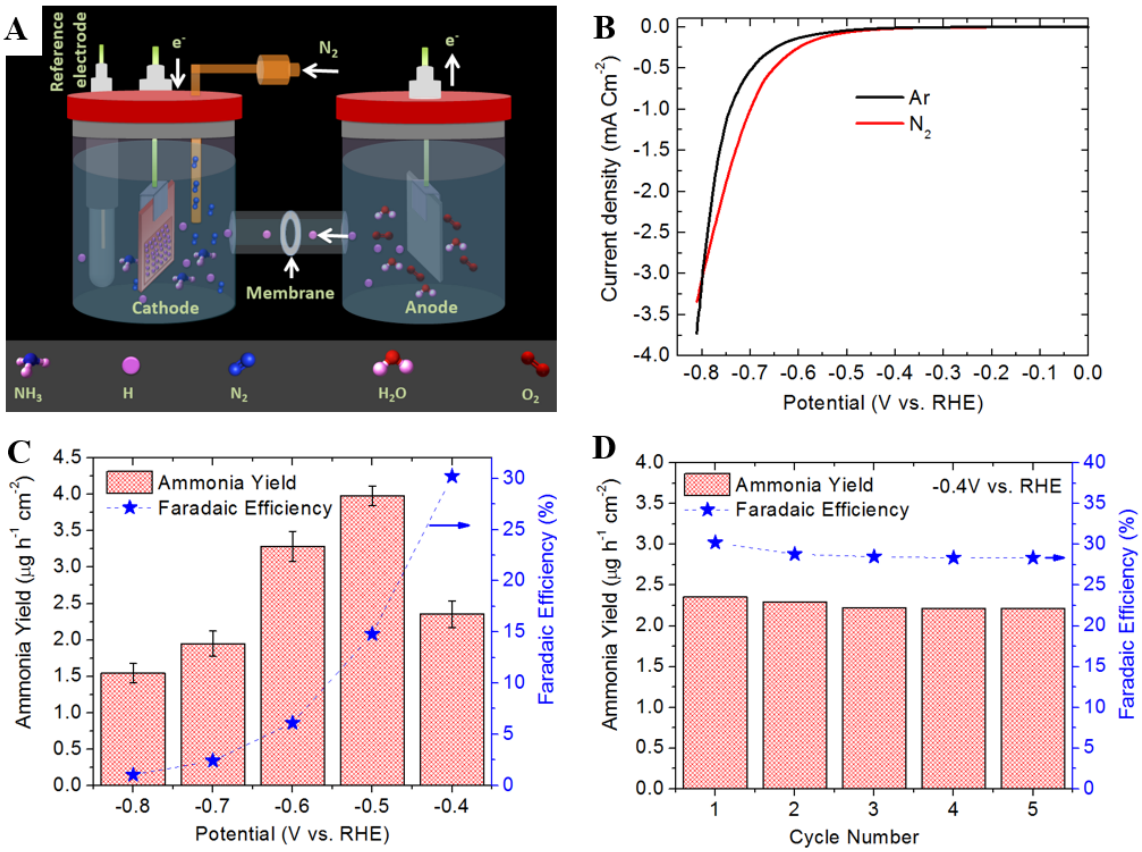

Figure 2.2: A) Schematic of electrochemical cell for NRR. The anode and cathode compartments are separated by a cation exchange membrane (CEM). B) Linear sweep voltammetry tests in an Ar and N_2 saturated environment in 0.5M $LiClO_4$ aqueous solution under ambient conditions. C) Ammonia yield rate and Faradaic efficiency at various potentials in 0.5M $LiClO_4$ at 20°C, D) Cycling stability results of ammonia yield rate on AuHNCs. For each cycle CA test was carried out at -0.4V vs. RHE in 0.5M $LiClO_4$ at 20°C.

1.1% at -0.8V vs. RHE), which suggests that HER is the dominant reaction at the cathode (**Figure 2.2C**). To evaluate the durability of AuHNCs, CA tests are performed at -0.4V vs. RHE for 5 consecutive cycles, each for 12 h. The electrocatalyst shows an excellent stability with a minor decrease in ammonia yield rate and Faradaic efficiency (93.8% performance retention) after the 5th recycling tests (**Figure 2.2D**).

To further verify the electrochemical NRR activity using AuHNCs, extensive control experiments are carried out with Ar gas and with no potential applied to the electrodes under N_2 gas (open circuit voltage). Under conditions similar to those in **Figure 2.2C**, except using Ar gas instead of N_2 and with N_2 but no potential applied, significantly smaller

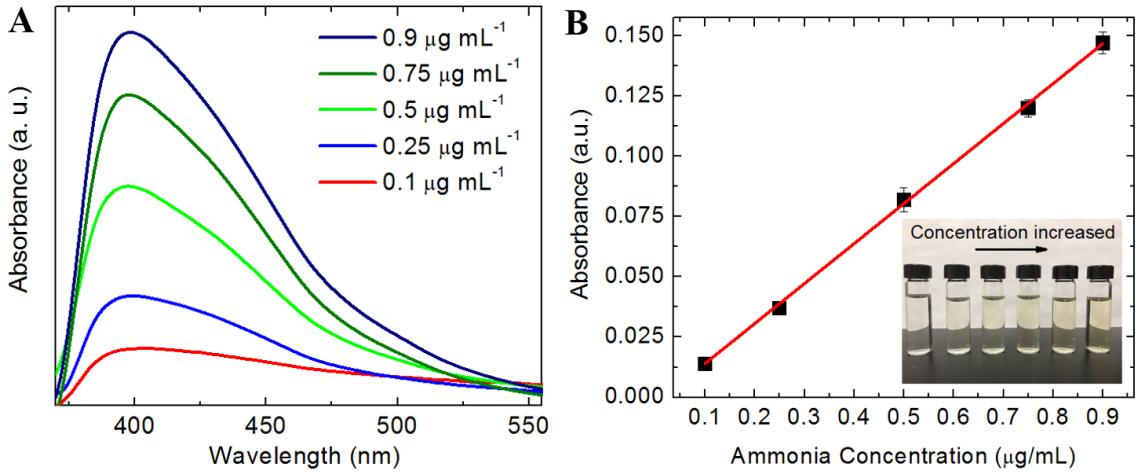

Figure 2.3: A) UV-vis calibration curve for ammonia quantification using Nessler's method. Known concentration of ammonium ions are added to 0.5M $LiClO_4$ electrolyte and mixed thoroughly with 1 mL of 0.2M $KNaC_4H_6O_6$ and 1 mL of Nessler reagent and then the absorbance at 395 nm is measured by the UV-vis spectrophotometer. The value of blank electrolyte is subtracted from all other concentrations as background.

amounts of NH_3 yield are achieved (**Figure 2.4A**). This confirms that the results with the N_2 gas under applied potential are not due to the sources of contamination (e.g., laboratory, equipment, membrane). The formation of ammonia during the electrochemical NRR experiments is further validated by surface-enhanced Raman spectroscopy (SERS) [60, 61]. Here, the solution collected from the electrochemical experiment, which showed the highest ammonia Faradaic efficiency (-0.4V vs. RHE at 20°C), was mixed with AuNCs, and the SERS spectrum was collected under 785 nm laser excitation (**Figure 2.4B**). We also conducted a control experiment, where we collected the SERS spectrum for 0.5M $LiClO_4$ under the same operating condition, as the SERS band corresponds to the ligand molecules on the AuNCs surface; as well as $LiClO_4$ could possibly interfere with the Raman features of ammonia. In comparison to the SERS spectra collected from the control experiment, a new Raman band at 3062 cm^{-1} appeared for the sample analyzed after the electrochemical experiment, which is attributed to the NH_4^+ moiety present in the electrolyte [62, 63]. This was further validated by collecting the Raman spectrum from crystalline NH_4F, which showed a corresponding mode of vibration for NH_4^+ at around 3075 cm_{-1}. The observed

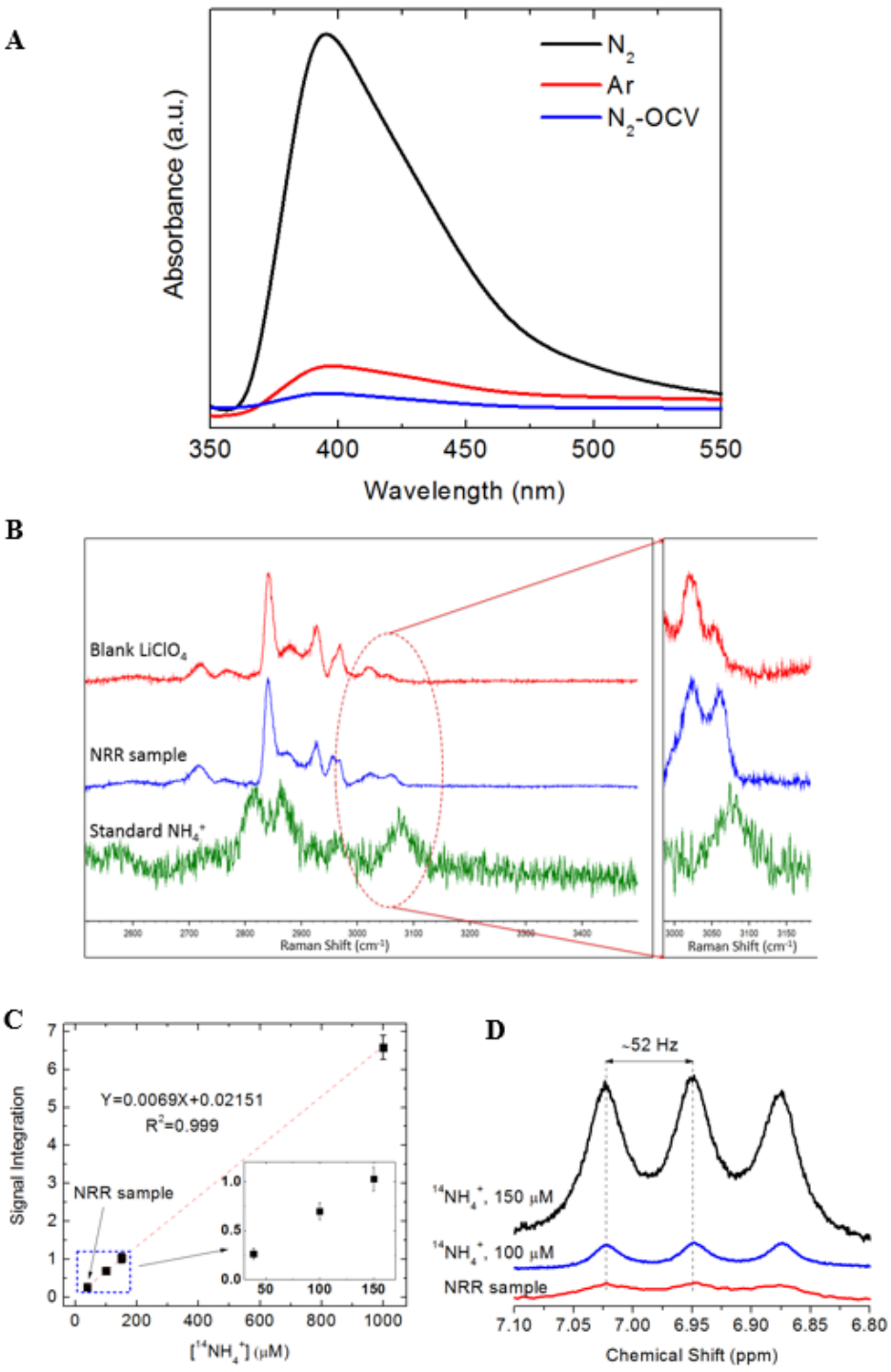

Figure 2.4: A) UV-vis absorption spectrum of AuHNCs in 0.5M $LiClO_4$ aqueous solution under N_2 saturated with and without applied potential and Ar gas with applied potential (-0.4V vs. RHE). B) Raman spectra of blank 0.5 M $LiClO_4$ aqueous solution, NRR sample, and standard NH_4^+ sample. C) Calibration curve of the ^1H NMR signal at 6.95 ppm for standard solutions of NH_4^+ (100, 150, 1000 μM) and NRR sample. D) ^1H NMR spectra (700 MHz) of NH_4^+ produced from the NRR experiment and standard NH_4^+ samples. ^{14}N produces a triplet with $\sim$52 Hz J coupling constant.

shift in the Raman band corresponds to NH_4^+ in SERS spectrum in comparison to the normal Raman spectrum could be attributed to the plasmon-enhanced electromagnetic field effect as well as the modifications in the adsorption (physisorption and chemisorption) orientation of these molecules at the nanoparticle surface. This result points towards the fact that ammonia formed during the electrochemical experiment largely exists as ammonium ions (NH_4^+) in the electrolyte. Furthermore, ^{1}H NMR spectra obtained from the sample in the NRR experiment lie at a chemical shift of triplet coupling of $^{14}N_2$ similar to that of standard $^{14}NH_4^+$ samples (J- coupling: $\sim$52 Hz), which further confirms that the ammonia formation is solely originated from N_2 (**Figure 2.4C**). The ammonia production at -0.4V vs. RHE at 20^{o}C quantified from the ^{1}H NMR analysis is 38.6 μM (**Figure 2.4D**). This is compared with 41.5 μM of ammonia, measured by UV-vis spectra using Nessler's test.

By increasing the concentration of AuHNCs from 0.9 μg mL^{-1} to 1.8 μg mL^{-1} (Figure S7) on the Si substrate (1 cm^2) at -0.5V vs. RHE, both the ammonia yield rate and the Faradaic efficiency increase from 1.88 μg cm^{-2} h^{-1} and 3.12% to 3.98 μg cm^{-2} h^{-1} and 14.8% (**Figure 2.5A**). This is due to the increase in the number of nanoparticles participating in the NRR, which results in an increase in the total active surface area on the substrate. By increasing the electrochemical NRR temperature from 20^{o}C to 50^{o}C at -0.4V vs. RHE, the ammonia yield rate and Faradaic efficiency increase from 2.35 μg cm^{-2} h^{-1} and 30.22% to 2.82 μg cm^{-2} h^{-1} and 40.55% (**Figure 2.5B**). Based on the Arehenius equation, the reaction rate increases expotentially with the temperature. The mass transport rate is faster at higher temperatures, while the N_2 solubility decreases at higher temperatures. For these experiments, faster kinetics plays a major role in enhancing the NRR rate at higher temperatures. The ammonia yield rate and Faradaic efficiency can be further enhanced by using ionic liquids (e.g., [C4mpyr][eFAP]) that offer significantly higher N_2 solubility compared to the aqueous solution [64].

To further investigate the cage effect using AuHNCs, the NRR rate is evaluated using solid Au nanoparticles of various shapes (i.e., rods, spheres, cubes) with similar nanopar-

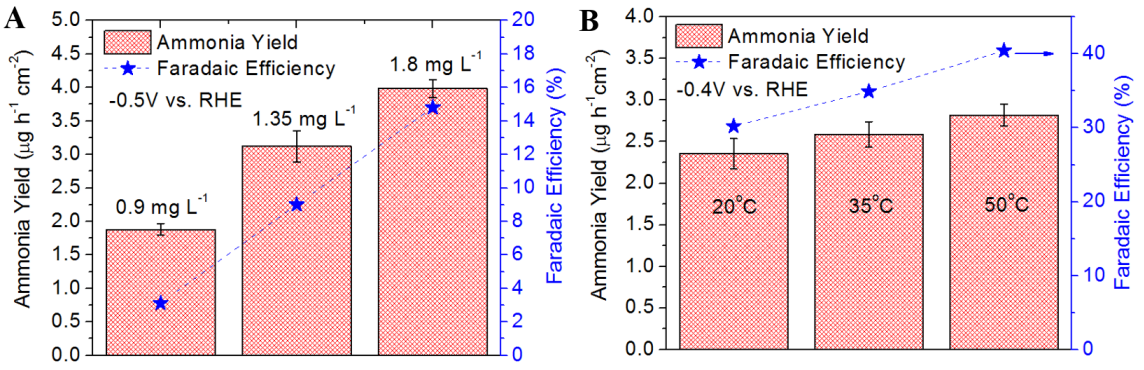

Figure 2.5: A) Ammonia yield rate and Faradaic efficiency of AuHNCs at various concentrations at -0.5V vs. RHE in 0.5M $LiClO_4$ aqueous solution under ambient conditions. B) Ammonia yield rate and Faradaic efficiency of AuHNCs at various temperatures at -0.4V vs. RHE in 0.5M $LiClO_4$ aqueous solution.

ticle concentrations. The LSPR of AuNSs and AuNCs lies at 535 nm and two plasmon peaks for AuNRs are observed which are attributed to the transverse (512 nm) and longitudinal (746 nm) modes (**Figure 2.6A**). The average diameter and edge length of AuNSs and AuNCs, respectively are 35 nm while AuNRs have an average length and width of 42 nm and 12 nm as obtained from TEM images (**Figure 2.6B, C, D**). The ammonia yield rate and Faradaic efficiency are significantly lower using solid Au nanoparticles compared to the AuHNCs (**Figure 2.6E**). The lowest ammonia yield rate and Faradaic efficiency are obtained for AuNRs (0.99 μg cm^{-2} h^{-1}, 10.69%). A minor increase in the NRR rate is observed using AuNSs (ammonia yield rate: 1.19 μg cm^{-2} h^{-1}, Faradaic efficiency: 11%) and AuNCs (ammonia yield rate: 1.27 μg cm^{-2} h^{-1}, Faradaic efficiency: 11.35% for AuNCs). This is in accordance with our previous findings, which suggest that nanoparticles with sharper edges and corners yield higher catalytic activity [13]. This is due to the increased number of valency-unsatisfied surface atoms (atoms that do not have the full number of bonds that they can chemically accomodate) in nanoparticles with sharper edges, providing more active sites for catalytic reaction than smoother nanoparticles [13].

The significant enhancement in the NRR rate using AuHNCs is attributted to the entrapment of N_2 molecules within the cavity, as these likely experience high frequency collisions

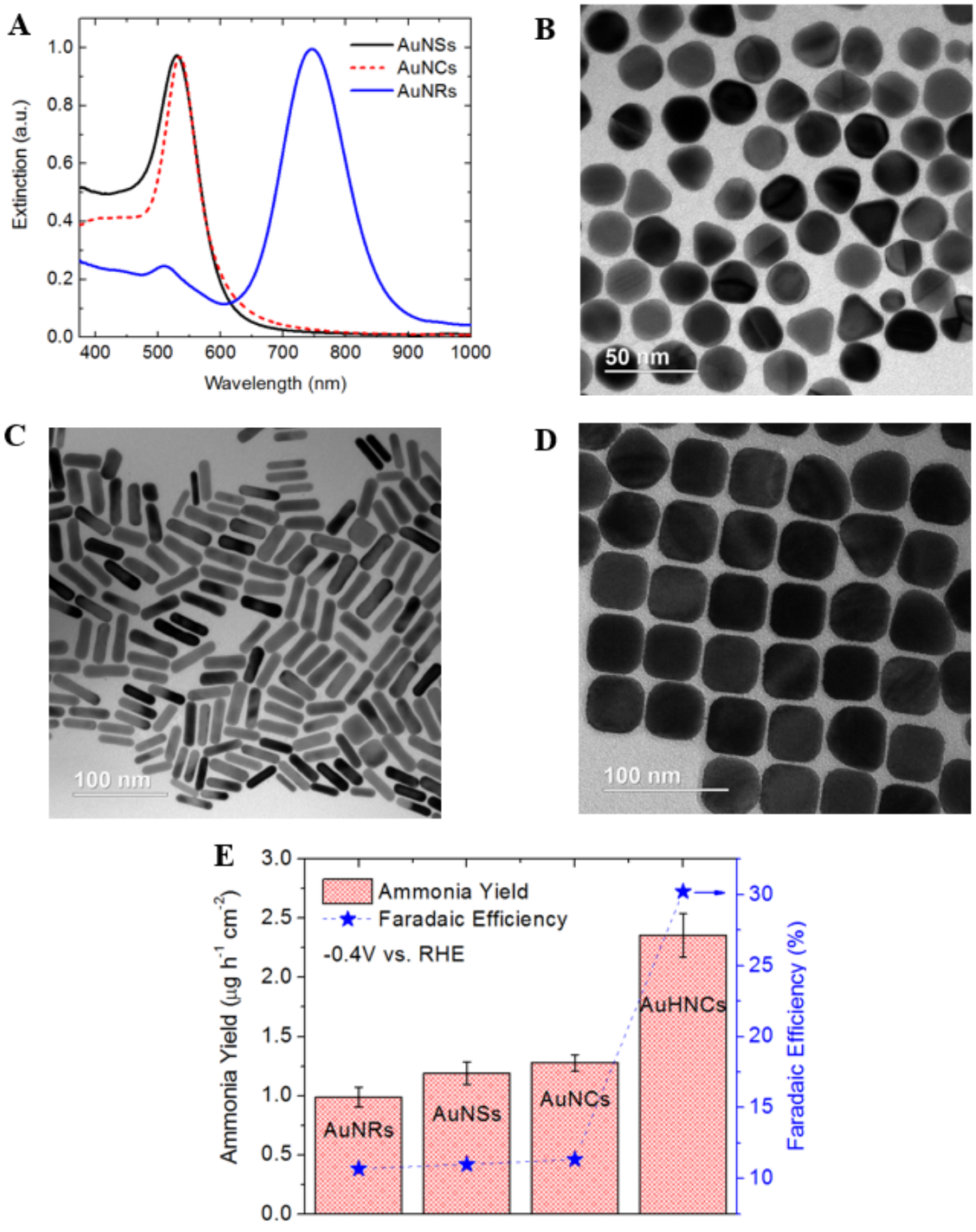

Figure 2.6: A) UV-vis extinction spectra of AuNSs, AuNCs, and AuNRs, B), C), and D) are the TEM images of AuNSs, AuNRs, and AuNCs, respectively. E) Ammonia yield rate and Faradaic efficiency for nanoparticles of various types and shapes at the potential of -0.4V vs. RHE in 0.5M $LiClO_4$ aqueous solution.

with the hollow Au interior surface of the cages. This increases the residence time of N_2 molecules at the nanoparticle inner surface, which facilitates the conversion of N_2 to NH_3. In addition, the presence of less capping material (i.e., polyvinylpyrrolidone (PVP)) on the inner surface than the outer surface of the AuHNCs can enhace the NRR catalytic activity.

2.4 Conclusion

Electrocatalytic activity of NRR under ambient conditions was studied using AuHNCs as an effective electrocatalyst in 0.5M $LiClO_4$ aqueous solution. The highest ammonia yield rate (3.9 μg cm^{-2} h^{-1}) is achieved at -0.5V vs. RHE, while the highest ammonia Faradaic efficiency (30.2%) is obtained at -0.4V vs. RHE using AuHNCs. At higher applied potentials, both ammonia yield rate and Faradaic efficiency decreased due to the intrinsic competition between NRR and HER. By increasing the electrochemical operating temperature from 20°C to 50°C at -0.4V vs. RHE, the ammonia yield rate and Faradaic efficiency were improved to 2.82 μg cm^{-2} h^{-1} and 40.55% from 2.35 μg cm^{-2} h^{-1} and 30.2%, which is attributed to the faster mass transport rate. By increasing the concentration of AuHNCs from 0.9 μg mL^{-1} to 1.8 μg mL^{-1} on the Si substrate, the ammonia yield rate and Faradaic efficiency increased from 1.88 μg cm^{-2} h^{-1} and 3.12% to 3.98 μg cm^{-2} h^{-1} and 14.8% at -0.5V vs RHE. It was demonstrated that due to the increase in the surface area, the higher number of successful collisions of reactants with the interior Au surface in the cavity (cage effect), and presence of less capping materials inside the cavity, AuHNCs offer superior electrocatalytic activity (three-fold enhancement) compared to the solid nanoparticles with the same concentration. The unique electrocatalytic activity of AuHNCs in NRR can open a new avenue for clean and sustainable ammonia electrosynthesis from N_2 and water under ambient conditions with high ammonia yield rate and Faradaic efficiency.

CHAPTER 3
PORE-SIZE CONTROLLED HOLLOW GOLD NANOCAGES WITH TUNABLE PLASMONIC PROPERTIES FOR AMMONIA ELECTROSYNTHESIS

3.1 Introduction

In this chapter, I aim to find the optimum size and density of pores in the walls of hollow Au nanocages (AuHNCs) by tuning their LSPR peak position; in this way, I aim to enhance the rate of electro-reduction of N_2 to NH_3. The interdependency between the pore size/density, the LSPR peak position, the silver content in the cavity, and the total surface area of the nanoparticle will be discussed for further optimization of hollow plasmonic nanocatalysts in electrochemical NRR.

3.2 Experimental Methods

The detailed procedure to synthesize AgNCs and AuHNCs was reported in experimental methods of Chapter 2. Here, the procedure for the synthesis of silver nanospheres (AgNSs) and hollow Au nanospheres (AuHNSs) are discussed.

3.2.1 Nanoparticle Synthesis

Synthesis of AgNSs

In a 100 mL round-bottom glass flask, 50 mL of EG is stirred and heated at 145°C for 20 min. Then, 0.4 g of PVP (MW 55,000) is added to the hot EG. $AgNO_3$ (0.2 g) dissolved in 5 mL of EG is added at once at a stirring speed of 500 rpm. The solution turns yellow due to the reduction of Ag ions into silver nanoparticles. By increasing the time of heating of the solution, the LSPR peak position redshifts and the size of AgNSs increase. The reduction of Ag salt is completed after approximately 7 min. The AgNSs is then quenched

using ice-water solution to avoid increasing the size of AgNSs. The same procedure that was used for AgNCs is used to clean AgNSs.

Synthesis of AuHNSs

The precipitated AgNSs are dispersed in a solution of 0.01 g PVP dissolved in 100 mL of DI water. Then the solution in water is heated and brought to boiling. $HAuCl_4$ solution (aq., 0.2 g L^{-1}) is injected slowly into the hot Ag solution until the LSPR peak position of the solution shifts to the desired value of 635nm, 715nm, and 795nm. The solution is refluxed with stirring for 2 min until the LSPR becomes fixed. The solution is cooled and cleaned by centrifugation at 10,000 rpm for 10 min. The precipitated nanoparticles are dispersed in DI water for future use. The AuHNCs with LSPR peaks at 635 nm, 715 nm, and 795 nm have optical densities (ODs) of 1.5, 2.6, and 2.0. The AuHNSs with LSPR peaks at 635 nm, 715 nm, and 795 nm have ODs of 0.8, 1.4, and 1.0.

3.2.2 Determination of the Electrochemical Surface Area (ECSA) of the nanoparticle

The electrochemical surface areas (ECSA) of AuHNCs with various pore sizes were determined by cyclic voltammetry (CV) tests in Ar-saturated 0.1M LiOH aqueous solution (200 mL) in a rotating disk electrode (RDE) setup at a rotation rate of 1500 rpm with a scan rate of 50 mV s^{-1}. A polished glassy-carbon disk electrode (0.2 cm^2 area) mounted on an interchangeable RDE holder (Pine Instruments) was used as the working electrode. A platinum coil and a single junction Ag/AgCl reference electrode (4M KCl with AgCl solution, Pine Instruments) were used as counter and reference electrodes. To mitigate any interferences on CV measurements, both counter and reference electrodes were separated from the main cell by an electrolyte bridge. Prior to measuring CVs for $ECSA_{Au}$ calculation, the working electrode was conditioned by conducting CV tests for 50 cycles at a scan rate of 200 mV s^{-1} to remove possible surface impurities and achieving stable current density response. Then, 20 μL of AuHNCs with 0.1 μL of nafion solution (5% wt.) were sonicated and dispersed on

a polished glassy-carbon electrode with Au loadings of 0.12, 0.19, and 0.27 μg_{Au} $cm^{-2}{}_{disk}$ for AuHNCs-635, AuHNCs-715, and AuHNCs-795. To more uniformly disperse nanoparticles on the glassy carbon, nanoparticles were dried on the glassy-carbon with the rotation rate of 600 rpm at room temperature. The $ECSA_{Au}$ of the catalyst is determined from the charge associated with the reduction peak of Au oxide after double layer correction and is normalized to the Au loading on the working electrode and charge density of 386 μC cm^{-2} according to the equation 5.3:

$$ECSA(\frac{cm^2_{Au}}{g_{Au}}) = \frac{Q(\mu\ C\ cm^{-2})}{386\ \mu\ C\ cm^{-2}_{Au} \times electrode\ loading\ (g_{Au}\ cm^{-2})} \tag{3.1}$$

where Q (μC cm^{-2}) is the charge associated with the reduction peak of Au oxide after double layer correction and calculated according to the equation 5.4:

$$Q = \frac{\int iV}{\nu} \tag{3.2}$$

where i is the current density (μA cm^{-2}), V is the potential (V), and v (V s^{-1}) is the scan rate.

3.3 Results and Discussion

AuHNCs with various LSPR peak values (i.e., 635nm, 715nm, and 795nm) are prepared by adding hydrogen tetrachloroaurate (0.5 mM $HAuCl_4$ (aq.)) in solid Ag nanocubes (AgNCs) that are dispersed in DI water using the galvanic synthetic method [5, 21]. By increasing the amount of Au^{3+} ions added to the AgNCs template with the initial LSPR peak position at 445 nm, the core Ag atoms are etched and the resulting LSPR peak value of AuHNCs redshifts (**Figure 3.1A**).

The first stage of this synthesis after adding Au^{3+} to the template solution is the formation of nanoboxes with walls composed of Ag-Au alloy at the LSPR peak value of 635nm (**Figure 3.1B**). As more Au^{3+} is added to the boxlike AuHNCs solution, the de-alloying

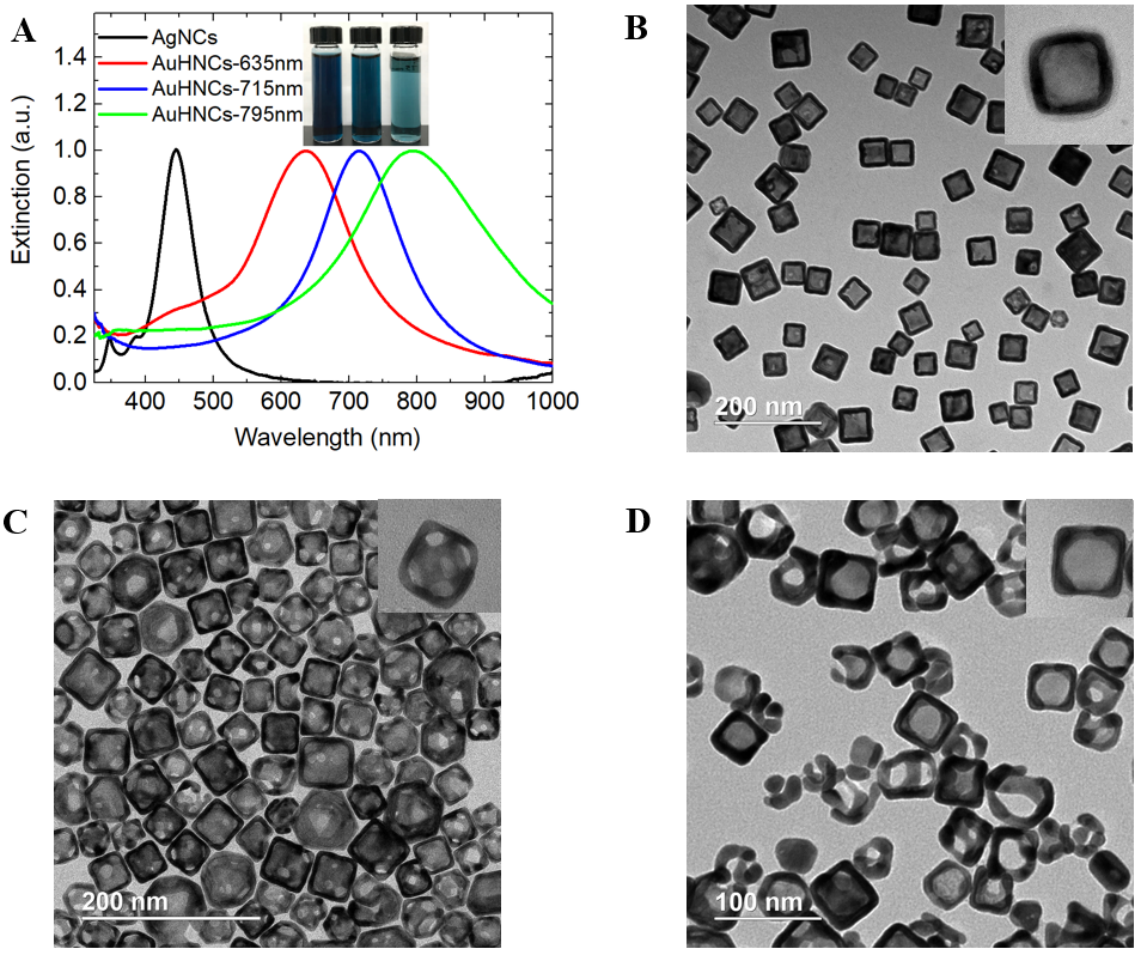

Figure 3.1: A) UV-vis extinction spectra of AgNCs and AuHNCs with various LSPR peak values, the photograph shown in the inset is AuHNCs dispersed in DI water. B), C), and D) are the TEM images of AuHNCs with LSPR peak values at 635nm, 715nm, and 795nm, respectively. The inset of each image is the magnified TEM image of a nanoparticle.

process of Ag atoms from the Ag-Au walls is initiated. Numerous pores are formed at the walls and corners of AuHNCs at the LSPR peak value of 715nm (**Figure 3.1C**). By further adding Au^{3+} to the porous AuHNCs, the pore size increases while the pore density decreases and the LSPR peak value redshifts to 795nm (**Figure 3.1D**). By shifting the LSPR peak value from 635nm to 715nm, the small peak in UV-vis spectrum around 445nm disappears, indicating the removal of Ag from the interior surface of the cavity (**Figure 3.1A**). The Au and Ag concentrations of all synthesized nanoparticles are determined by inductively coupled plasma emission spectroscopy (ICPES). It is observed Au content (mass %)

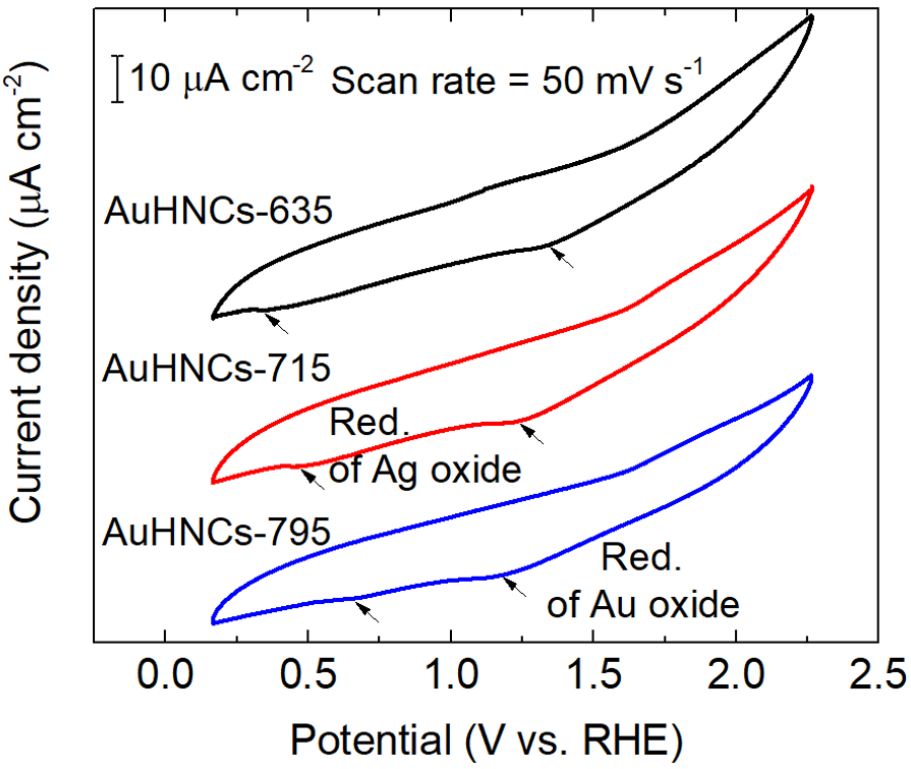

Figure 3.2: Cyclic voltammograms (CV) of AuHNCs with various peak LSPR values in Ar-saturated 0.1M LiOH aqueous solution at a scan rate of 50 mV s^{-1}. The CV measurements were conducted in the rotating disk electrode (RDE) setup at a rotation rate of 1500 rpm at room temperature. The observed shift in decreasing the reduction potential of Au oxide ($\sim$0.15V) when LSPR redshifts from 635 nm to 795 nm is attributed to the de-alloying process by removal of Ag in the cavity. The second peak in the reduction segment of the CV curve corresponds to the reduction of Ag oxide. The intensity of the peak is proportional to the Ag concentration which is the highest for AuHNCs-715.

in nanoparticles increases from 33.0 to 64.7 as the LSPR peak position shifts from 635 nm to 795 nm (**Table 3.1**). In addition, the electrochemical surface areas (ECSA) of nanocages are determined in the three-electrode setup by performing cyclic voltammetry (CV) in Ar-saturated 0.1M LiOH solution at a scan rate of 50 mV s^{-1}. The $ECSA_{Au}$ is calculated from the reduction peak of Au oxide after double layer correction and a charge density of 386 μC cm^{-2} (**Figure 3.2** and **Table 3.1**). AuHNCs-715 has the highest $ECSA_{Au}$ (26.6 m^2 g^{-1}) while AuHNCs-795 has the lowest $ECSA_{Au}$ (21.3 m^2 g^{-1}). Although AuHNCs-795 has the highest Au concentration among all nanoparticles (**Table 3.1**), it has the lowest $ECSA_{Au}$. This is attributed to the simultaneous reduction of Au and Ag atoms in the final stage of

Table 3.1: Au, Ag concentrations, Au and Ag content (% at.) of nanoparticles are determined by inductively coupled plasma emission spectroscopy (ICPES). The electrochemical surface areas (ECSA) of nanoparticles are determined based on the reduction peak of Au oxide during cyclic voltammetry measurement in Ar-saturated 0.1M LiOH solution at a scan rate of 50 mV s^{-1}. Atomic content is calculated using Au and Ag concentrations divided by the molar mass of Au (196.97 g mol^{-1}) and Ag (107.87 g mol^{-1}).

Catalyst	Au Conc. (μg mL^{-1})	Ag Conc. (μg mL^{-1})	Au Content (mass %)	Au Content (at. %)	$ECSA_{Au}$ (m^2 g^{-1})
AuHNCs-635	1.20	2.44	33.0	21.2	23.4
AuHNCs-715	3.91	3.45	53.1	38.3	26.6
AuHNCs-795	5.40	2.95	64.7	50.1	21.3

synthesis when the LSPR redshifts from 715nm to 795nm which changes the porosity of the nanocages and increases the void size. The smaller peak observed for the reduction of Au oxide compared to previous studies [65, 66] is due to the significantly smaller Au loading (e.g., 0.39 μg_{Au} $cm^{-2}{}_{disk}$ for AuHNCs-715) which is necessary when economic feasibility of using this electrocatalyst for ammonia synthesis is investigated.

An H-type cell, in which anodic and cathodic compartments are separated by a proton exchange membrane, was set up to carry out electrochemical NRR. The electrolyte is the 0.5M $LiClO_4$ aqueous solution. Thermodynamically, the NRR occurs at approximately the same potential as the HER ($E^0{}_{RHE}$=0.05V for NRR, $E^0{}_{RHE}$=0V for HER). Using a Li^+ cation is beneficial due to its strong ability to activate N_2 at ambient conditions and retard the HER process [67]. Water oxidation is the primary reaction at the anode, and N_2 gas is purged to the cathode where the protons produced by water oxidation are transported from the anode to the cathode side through the proton exchange membrane, after which they react with N_2 and produce NH_3. Linear sweep voltammetry (LSV) tests are carried out in Ar and N_2 saturated electrolyte to evaluate the selectivity performance ($\frac{I_{N_2}-I_{Ar}}{I_{N_2}} \times 100$) of AuHNCs with various values of LSPR peak toward NRR. Faradaic current is obtained by subtracting the capacitive current from the actual current recorded from LSV tests. For all electrocatalysts, current density differs between Ar, and N_2 within the potential window

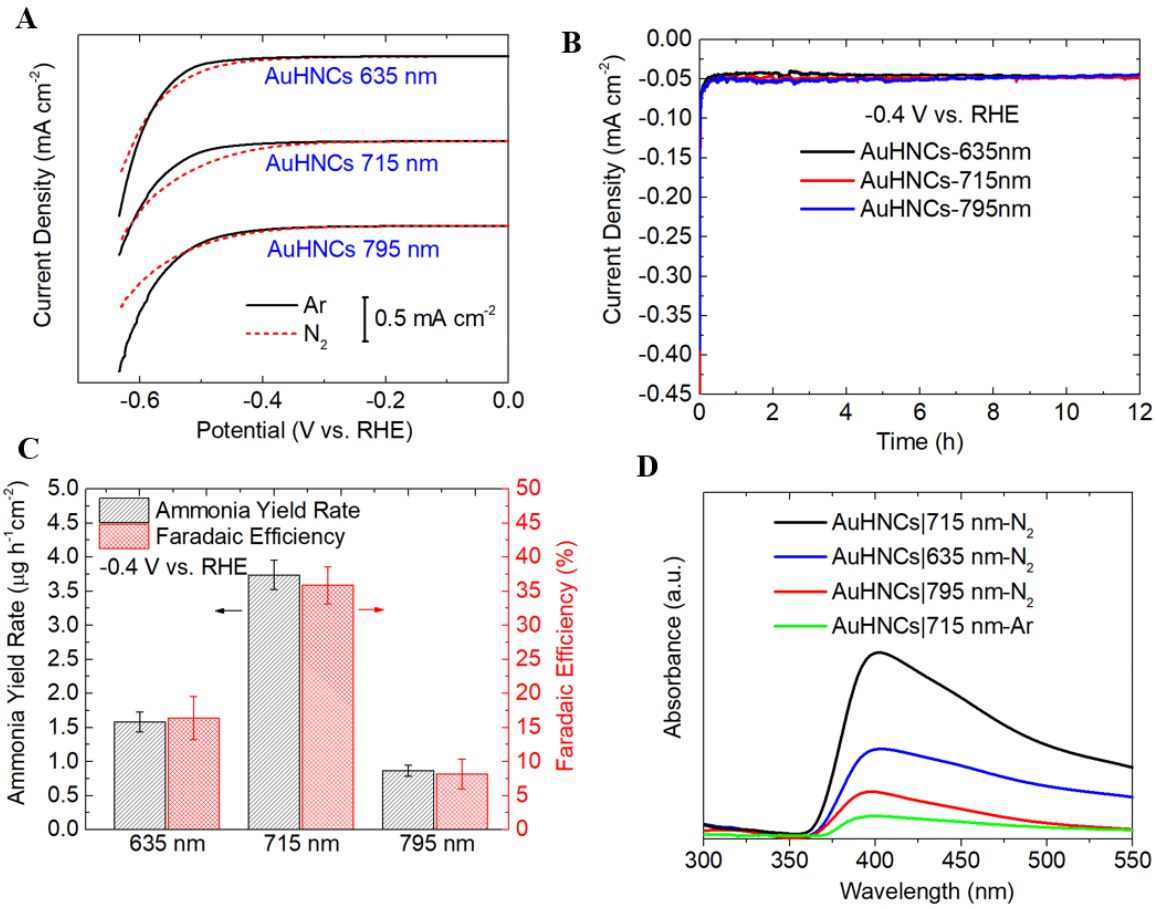

Figure 3.3: A) Linear sweep voltammetry (LSV) tests of AuHNCs with LSPR peak values at 635nm, 715nm, and 795nm in an Ar and N_2 saturated 0.5 M $LiClO_4$ (aq.) under ambient conditions with the scan rate of 10 mV s^{-1}. B) Chronoamperometry (CA) results of AuHNCs with various LSPR peaks at -0.4 V vs. RHE in N_2 saturated 0.5M $LiClO_4$ (aq.). C) Ammonia yield rate and Faradaic efficiency for AuHNCs with various LSPR peak values at the potential of -0.4 V vs. RHE in 0.5M $LiClO_4$ (aq.). D) UV-vis absorption spectra of N_2 and Ar saturated 0.5 M $LiClO_4$ (aq.) after electrolysis at -0.4V vs. RHE for 12 h using Nessler's test for AuHNCs with various LSPR peak values.

of -0.3V to -0.6V vs. RHE (**Figure 3.3A**). Beyond this potential window, the HER is the dominant reaction. The highest selectivity toward the NRR (65.3% at -0.4V vs. RHE) is achieved using AuHNCs-715. This is compared with 48.7% and 27.4% at -0.4V vs. RHE for AuHNCs-635 nm and AuHNCs-795 nm. The complete selectivity performance of electrocatalysts at three different potentials is provided in Table 3.2. The highest N_2 selectivity for AuHNCs-715 is attributed to the compromise between the pore size, the active surface area of the nanoparticle, and the Ag content in the cavity of AuHNCs. Although by in-

Table 3.2: Selectivity performance of AuHNCs with various LSPR peak values toward NRR

Electrocatalyst	Potential (V vs. RHE)		
	-0.3	-0.4	-0.5
AuHNCs-635	52.3	48.7	45.1
AuHNCs-715	55.6	65.3	56.3
AuHNCs-795	20.2	27.4	11.0

creasing the pore size, the active surface area of nanoparticle decreases, the presence of Ag in the cavity of AuHNCs with smaller pore sizes (i.e., AuHNCs-635) decreases the selectivity of an electrocatalyst toward NRR, as Ag enhances H_2 evolution. It is noted that all electrochemical experiments are conducted in O_2-free environment to avoid the formation of Ag_2O in the cavity. As the NRR primarily happens within the cavity, the AuHNCs that have smaller pore size but that have Ag within the cavity (AuHNCs-635) result in lower selectivity for NRR compared with AuHNCs that have bigger pore size but do not have Ag in the cavity (AuHNCs-715). Further increasing the pore size decreases the NRR selectivity due to both the decrease of the surface area and the inefficient confinement of reactants within the cavity (AuHNCs-795). The pore size should be engineered so that reactants can diffuse in and products can diffuse out of the cavity while not losing the surface area notably, due to the increase in the pore size in the walls of the nanocages. Therefore, the optimization of the pore size plays a crucial role in confining the reactants in the small region within the cavity and increasing their collision frequency with the interior surface of the electrocatalyst.

Chronoamperomtry (CA) tests are conducted at -0.4V vs. RHE to evaluate the electrocatalytic activity and to determine the ammonia yield rate and FE for AuHNCs-635, AuHNCs-715, and AuHNCs-795 (**Figure 3.3B**). The highest ammonia yield rate (3.74 μg cm^{-2} h^{-1}) and FE (35.9%) are achieved using AuHNCs-715 while the lowest ammonia yield rate (0.87 μg cm^{-2} h^{-1}) and FE (8.2%) are obtained for AuHNCs-795 (**Figure 3.3C**). This is in line with the trend of the selectivity performance of electrocatalysts for NRR

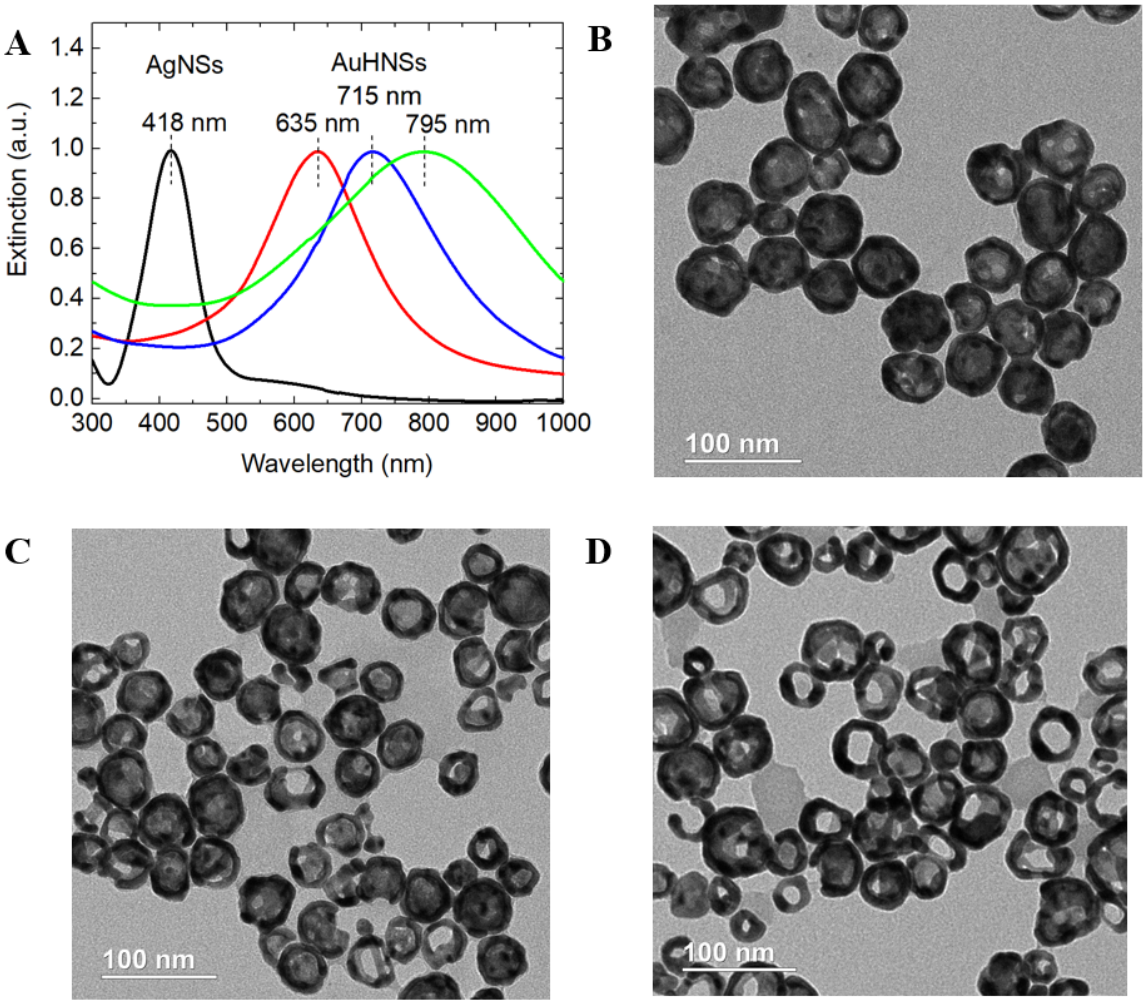

Figure 3.4: A) UV-vis extinction spectra of AgNSs and AuHNSs with various LSPR peak values. B), C), and D) are the TEM images of AuHNSs with the LSPR peak values at 635nm, 715nm, and 795nm, respectively. The average diameter of nanoparticles is 55 nm.

(**Figure 3.3A**). A small amount of NH_3 is detected ($\sim$0.34 μg cm^{-2} h^{-1}, $\sim$9% of N_2 gas) when N_2 gas is replaced with Ar under the same applied potential using AuHNCs-715, which indicates that the majority of NH_3 in these experiments originated from the N_2 source (**Figure 3.3D**). Hollow Au nanospheres (AuHNSs) with LSPR peak values and electrolysis operating conditions similar to those of AuHNCs (**Figure 3.3C**) are evaluated for electrochemical NRR (**Figure 3.4**). The same trend as AuHNCs but lower electrocatalytic activity for NRR is observed using AuHNSs. The highest ammonia yield rate (2.77 μg cm^{-2} h^{-1}) and FE (29.3%) are achieved using AuHNSs-715; these values are lower than AuHNCs-

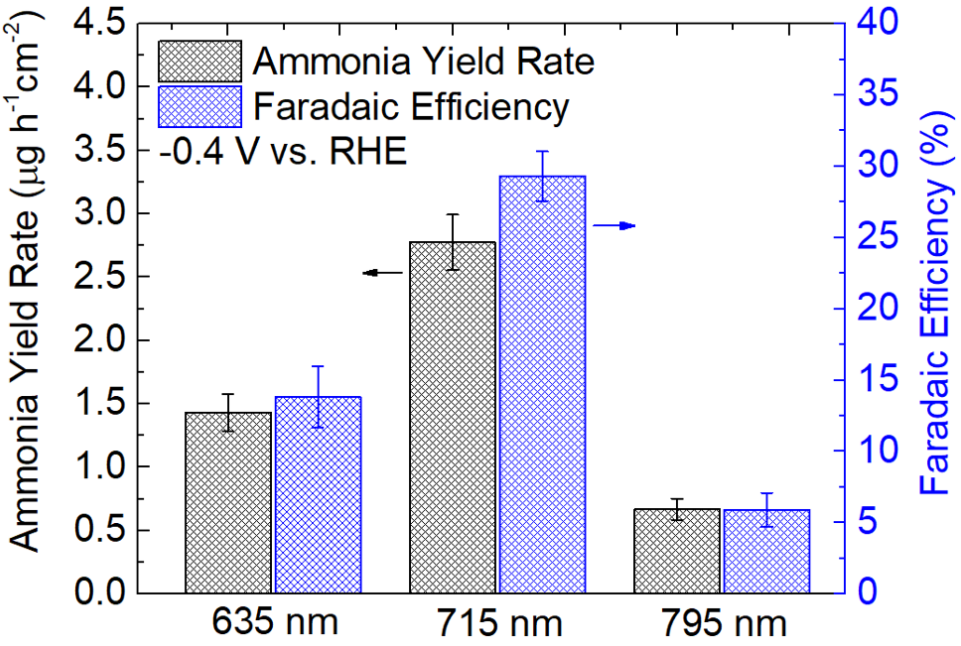

Figure 3.5: Ammonia yield rate and Faradaic efficiency for AuHNSs with various LSPR peak values at the potential of -0.4V vs. RHE in 0.5M $LiClO_4$ (aq.).

715 (3.74 μg cm^{-2} h^{-1}, FE=35.9%) (**Figure 3.5**). This could be attributed to small variations in the sizes of the nanospheres, cavity volume, pore sizes, and lack of sharp corners and edges in AuHNSs.

The role of pH on the electrocatalytic activity of NRR is evaluated using AuHNCs-715. It is found that operating the N_2 electrolysis in both acidic (0.5M $LiClO_4$+ 0.001M $HClO_4$, pH=3) and alkaline electrolyte (0.1M LiOH, pH=13) decreases the rate of ammonia production (Figure S6). This is attributed to the favorable HER in acidic conditions and higher thermodynamic potential for ammonia formation in the alkaline environment ($N_2(g) + 6H_2O + 6e^- \rightarrow 2NH_3(g) + 6OH^-$, $E_{RHE}^0 = -0.77V$). Moreover, decreasing the concentration of Li^+ in the alkaline electrolyte (0.1M) compared with neutral and acidic electrolytes (0.5M) results in a remarkable decrease of the NH_3 yield rate (**Table 3.3**). It is noted that an anion exchange membrane (AEM) is used for the electrolysis of N_2 in the alkaline solution to enable the transport of hydroxide anions (OH^-) from the cathode to the anode side for stable electrolysis.

Table 3.3: Electrochemical performance of NRR using AuHNCs-715 with various pH electrolytes at -0.4V vs. RHE.

Electrolyte	NH_3 Yield Rate (μg cm^{-2} h^{-1})	Average Current Density (μA cm^{-2})	Faradaic Efficiency (%)
0.5M $LiClO_4$ + 0.001M $HClO_4$ (pH=3)	3.10±0.15	57.1	25.7
0.5M $LiClO_4$ (pH=8)	3.74±0.22	49.2	35.9
0.1M LiOH (pH=13)	0.71±0.06	46.2	7.2

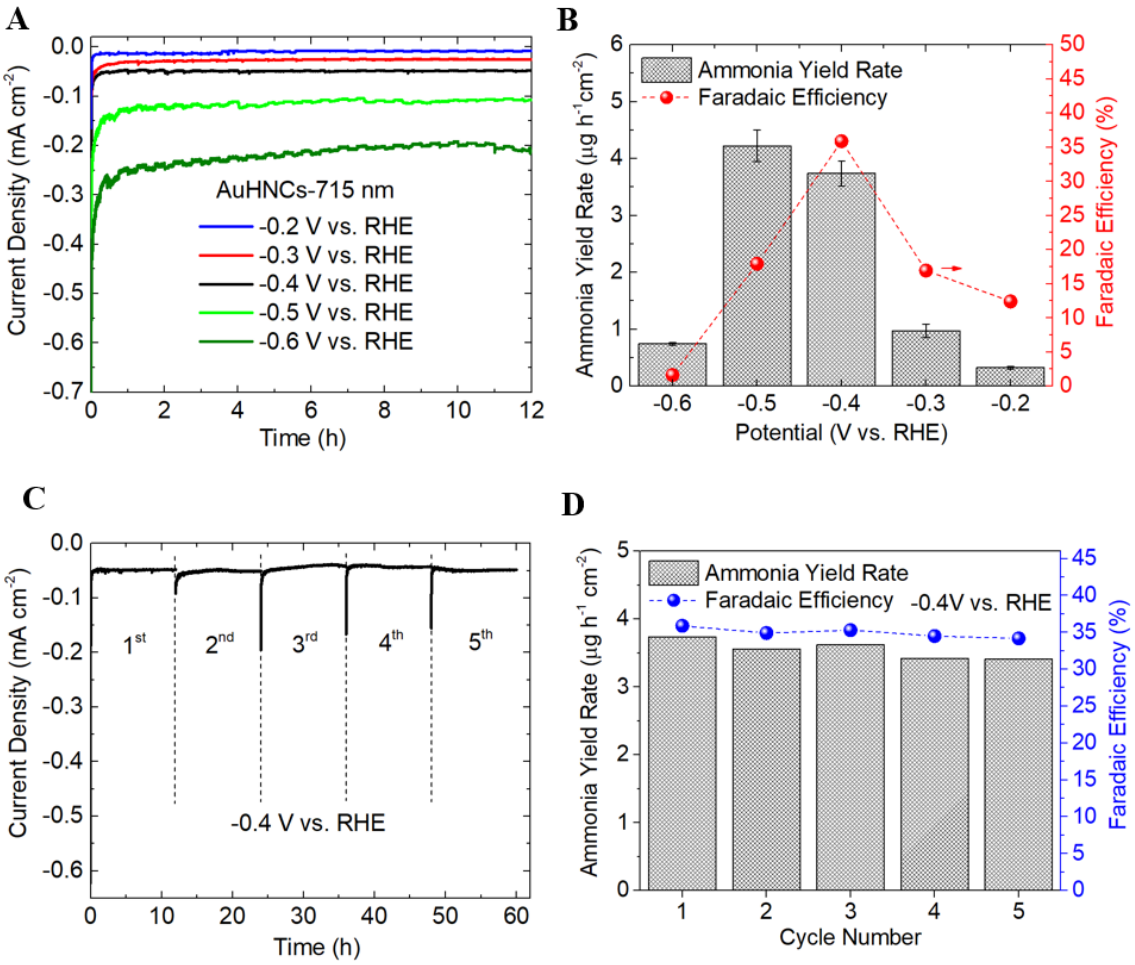

Figure 3.6: A) Chronoamperometry (CA) results of AuHNCs-715 nm at a series of potentials. B) Ammonia yield rate and Faradaic efficiency at various potentials in 0.5M $LiClO_4$ (aq.). C) CA tests for the stability of the AuHNCs-715 nm at -0.4V vs. RHE in 0.5M $LiClO_4$ (aq.). For each cycle a CA test was carried out at -0.4V vs. RHE for 12 h. D) Cycling stability results of ammonia yield rate and Faradaic efficiency on AuHNCs-715 nm. For each cycle a CA test was carried out at -0.4V vs. RHE in 0.5M $LiClO_4$ (aq.).

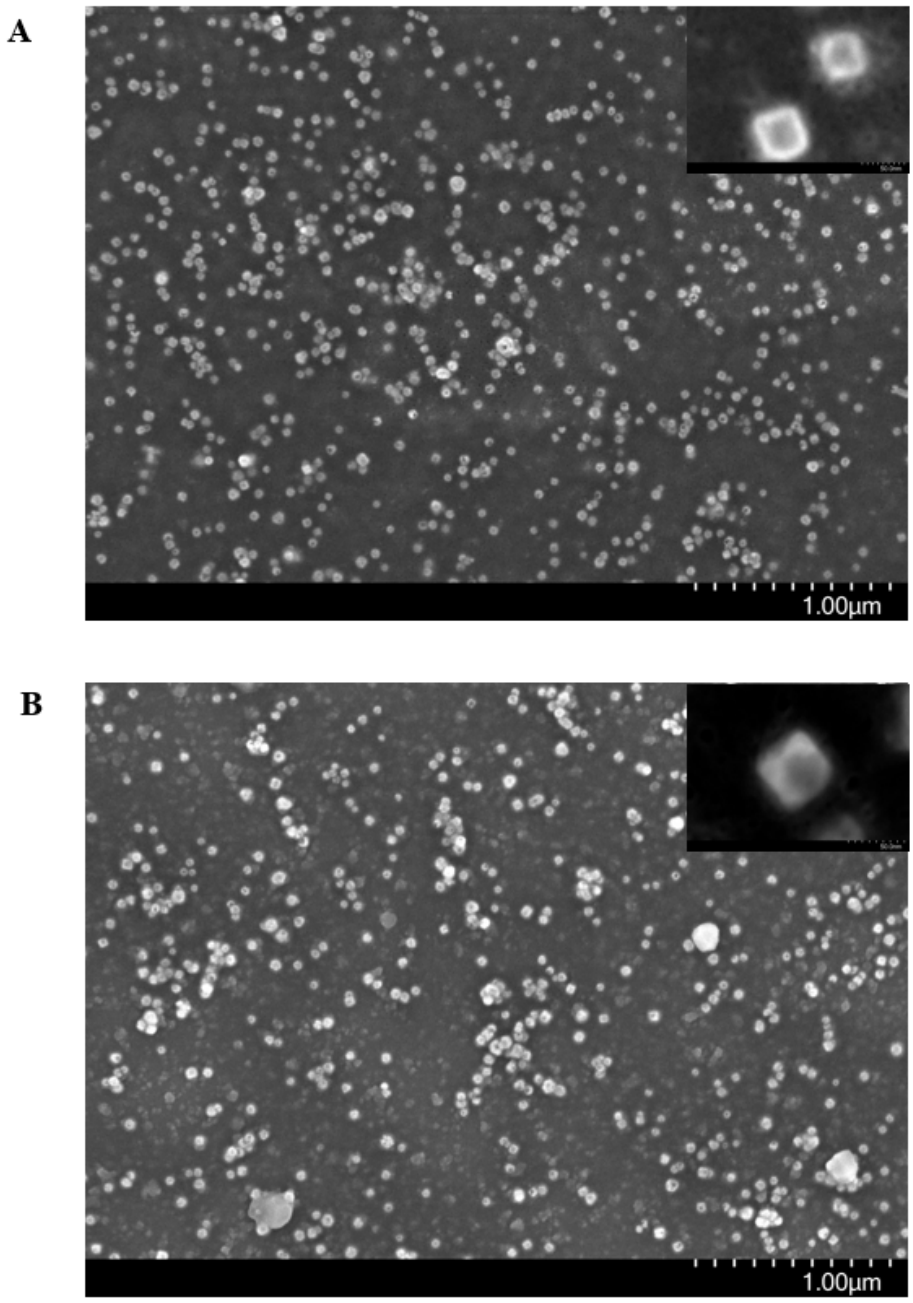

Figure 3.7: The SEM images A) before and B) after the durability test. The electrode after the test was thoroughly washed with DI water and dried at room temperature before taking the measurement.

CA tests are performed using AuHNCs-715 to determine the ammonia yield rate and FE at a series of applied potentials (**Figure 3.6A,B**). The highest ammonia yield rate (4.22 μg cm^{-2} h^{-1}) is obtained at -0.5V vs. the RHE with the FE of 17.9%. The higher ammonia

yield rate but lower FE at -0.5V, compared with -0.4V, is due to the compromise between achieving higher current density and higher selectivity toward HER. Moving toward more positive potentials than -0.4V and more negative potentials than -0.5 V, both NH_3 yield rate and FE decrease, which is consistent with the LSV results, in which selectivity of the electrocatalyst decreases toward NRR. The stability of AuHNCs-715 is evaluated for 60 h by conducting 5 consecutive cycles, each for 12 h, at -0.4V (**Figure 3.6C**). The electrocatalyst could maintain the continous NH_3 formation with stable NH_3 yield rate and FE (**Figure 3.6D**). In addition, the SEM images before and after the durability test show the morphology of supported nanoparticles is reasonably maintanied after 60 h of CA test (**Figure 3.7**).

3.4 Conclusion

Electrosynthesis of NH_3 from N_2 and H_2O under ambient conditions using AuHNCs with various values of pore size/density by tuning the LSPR peak position from 635 nm to 795 nm. The interdependency between the LSPR peak position, Ag content in the interior surface of the hollow Au nanoparticles, pore size/density, and total surface area of the nanoparticle on the electrocatalytic activity of NRR was studied. It was found that the presence of Ag in the cavity for AuHNCs-635 decreases the electrocatalytic activity of NRR. This was attributed to the higher activity of Ag toward HER. Additionally, increasing the pore size by redshifting the LSPR peak value to 795 nm for AuHNCs-795 is not beneficial for increasing the NH_3 yield rate and FE. This is due to the decrease of the active surface area of the nanoparticle and inefficient confinement of reactants in the cavity when the pore size increases. Among all electrocatalysts with various shapes (i.e., cube, sphere) and LSPR peak values (i.e., 635nm, 715nm, 795nm), the highest NH_3 yield rates (3.74 μg cm^{-2} h^{-1}) and FE (35.9%) are achieved using AuHNCs-715 at -0.4V vs. RHE.

Although future work requires overcoming the challenge of maintaining high NH_3 FE at high current densities and suppressing HER, the findings in this chapter leads to empirical

structure-activity trends for ammonia synthesis by an array of hollow nanocatalysts with tunable plasmonic properties.

CHAPTER 4
THE ROLE OF OXIDATION OF SILVER IN BIMETALLIC GOLD-SILVER NANOCAGES ON ELECTROCATALYTIC ACTIVITY OF NITROGEN REDUCTION REACTION

4.1 Introduction

In chapters 2 and 3, I discussed the use of bimetallic hollow Au-Ag nanocages as an effective electrocatalyst for electrosynthesis of ammonia in an ionic aqueous solution. The chemical stability of the electrocatalyst during electrochemical NRR is of paramount importance when considering the feasibility of electrochemical NRR for industrial applications. In this chapter, I aim to investigate the role of oxidation of Ag in bimetallic Au-Ag nanocages with various localized surface plasmon resonance (LSPR) peak positions by preparing Ag_2O-Au nanocages through the facile oxidation process to mimic the possible oxidation of Au-Ag electrocatalyst at the presence of O_2 in the electrolyte during electrochemical NRR. I further aim to discern the role of Ag on the selectivity and activity of the electrocatalyst toward NRR compared to active sites of Au surface in bimetallic Au-Ag nanocages.

4.2 Experimental Methods

4.2.1 Nanoparticle synthesis

Silver nanocubes (AgNCs) and Ag-Au nanocages with various LSPR peak positions are prepared by a modified polyol reduction of $AgNO_3$ and galvanic replacement techniques [68, 69]. For O_2 treatment of prepared nanoparticles, 5 mL of cleaned nanoparticle (e.g., Ag-Au-635) dispersed in DI water is transferred to the glass vial equipped with an inlet and outlet for purging gas. Then, pure O_2 gas is bubbled through the glass vial with the flow

rate of 20 mL min^{-1} for 6h. The Ag_2O-Au nanocages with LSPR peak positions at 644 nm, 719 nm have optical densities (ODs) of 1.4 and 2.4.

4.2.2 Electrochemical Measurement

A Mott-Schottky plot for Ag_2O-Au nanocubes at a frequency of 1000 Hz was obtained in 0.5M $LiClO_4$ aqueous solution under the dark condition. Cyclic voltammograms (CV) of nanoparticles were conducted in the three-electrode setup using a rotating disk electrode.

4.3 Results and Discussion

Bimetallic porous Au-Ag nanocages with various LSPR peak positions are prepared by adding $HAuCl_4$ (aq.) solution to the solid silver nanocubes (AgNCs) solution through the galvanic replacement method. By oxygenating the Au-Ag nanocages through purging the solution with pure oxygen gas, Ag is oxidized to form silver (I) oxide (Ag_2O) at room temperature, an extremely stable metal oxide semiconductor at ambient conditions. After oxygen treatment of the Au-Ag nanocages, the LSPR peak position slightly redshifts (e.g., 9 nm for Au-Ag-635), suggesting the formation of Ag_2O in the cavity and successful synthesis of Ag_2O-Au nanocages (**Figure 4.1A**). Furthermore, the SERS spectrum of Ag_2O shows distinct peaks at 460, 685, 817, 964, 1083 cm^{-1}, which are all attributed to the Ag-O vibrational modes (**Figure 4.1B**). These peaks with slight shift are observed for Ag_2O-Au nanocages, while no pronounced SERS peak is observed for the Au-Ag nanocages, further confirming the formation of Ag_2O after oxygen treatment of Au-Ag nanocages (**Figure 4.1B**) [70]. The size and density of pores in the walls of hollow Au-Ag nanocages are controlled by tuning their LSPR peak position. By increasing the amount of Au^{3+} ions added to the Ag-NCs template, Ag atoms are etched and replaced by Au atoms. This results in the LSPR peak position to redshift from 635 nm to 715 nm and the pore size at the walls and corners of the nanocages to increase (**Figure 4.1C, E**). The pore size and morphology of nanocages did not change significantly after the O_2 treatment of Au-Ag nanocages (**Figure 4.1D, F**).

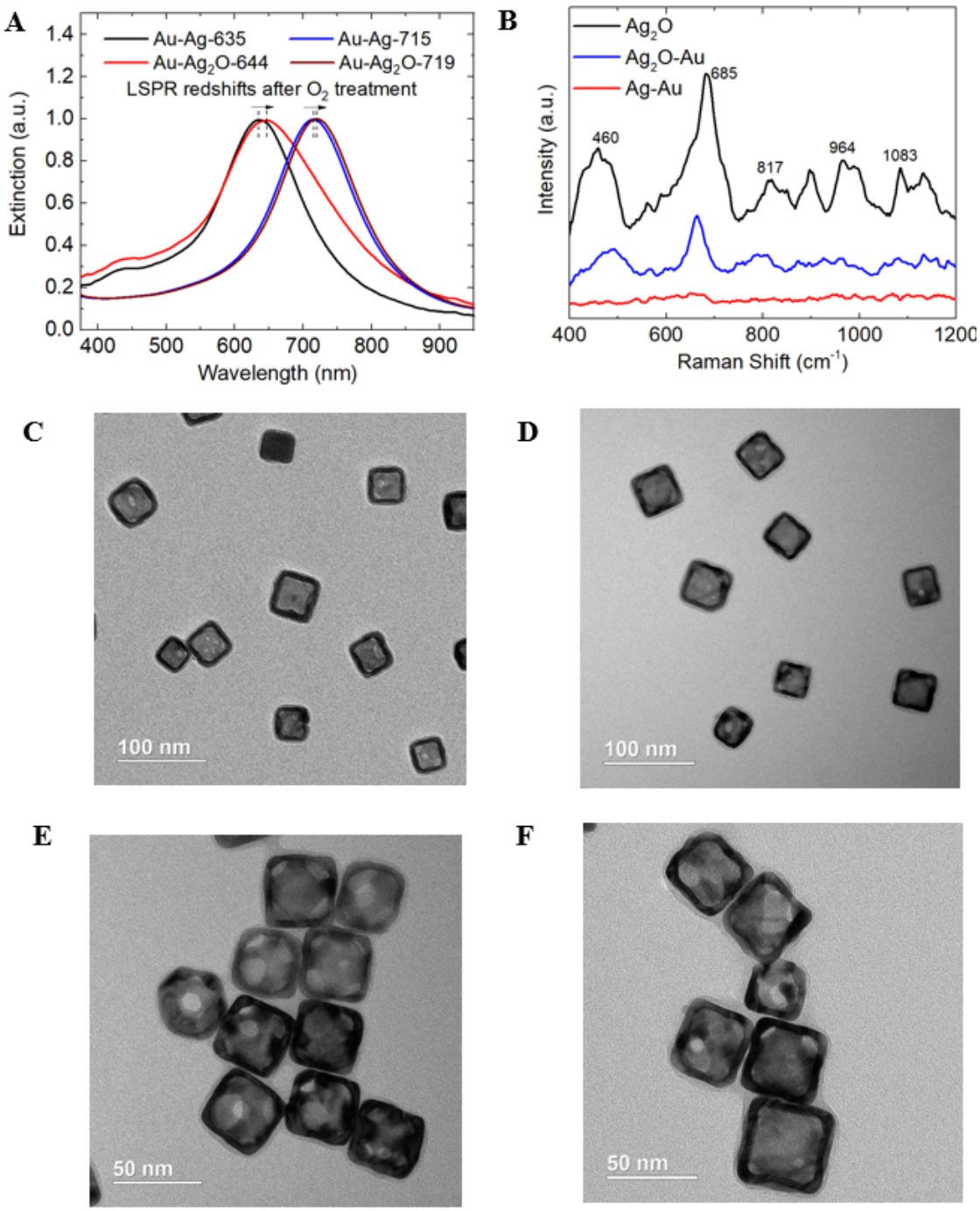

Figure 4.1: A) UV-vis extinction spectra of bimetallic Au-Ag nanocages with various LSPR peak positions before and after O_2 treatment. Before O_2 treatment, the bimetallic Au-Ag nanoparticles have the LSPR peak positions at 635 nm and 715 nm while after O_2 treatment the LSPR redshifts to 644 nm and 719 nm, suggesting the formation of Ag_2O in the cavity (Ag_2O-Au). B) SERS spectra of Ag_2O, Ag_2O-Au-685, and Ag-Au-670 nanoparticles. The TEM images of bimetallic Au-Ag nanocages with the LSPR peak position C) at 635 nm before O_2 treatment (Au-Ag-635) and D) at 644 nm after O_2 treatment (Ag_2O-Au-644). The TEM images of bimetallic Au-Ag nanocages with the LSPR peak position E) at 715 nm before O_2 treatment (Au-Ag-715) and F) at 719 nm after O_2 treatment (Ag_2O-Au-719).

Table 4.1: Au, Ag concentrations, Au content (mass % and atomic %) of various hybrid hollow plasmonic nanoparticles that are determined by inductively coupled plasma emission spectroscopy (ICPES) and their corresponding LSPR peak position. Atomic content (at. %) is calculated using Au and Ag concentrations divided by the molar mass of Au (196.97 g mol^{-1}) and Ag (107.87 g mol^{-1}).

Electrocatalyst	LSPR (nm)	Au Conc. (μg mL^{-1})	Ag Conc. (μg mL^{-1})	Au Content (Mass %)	Au content (Atom %)
Ag-Au	635	1.2	2.44	33.0	21.2
Ag_2O-Au	644				
Ag-Au	715	3.91	3.45	53.1	38.3
Ag_2O-Au	719				

Table 4.2: The shell composition of nanocages with various LSPR peak positions determined by EDX spectroscopy.

Nanoparticle	Ag (at. %)	Au (at. %)	O (at. %)
Ag-Au-635	73.63	5.96	20.41
Ag_2O-Au-644	65.82	5.68	28.50
Ag-Au-715	67.78	10.67	21.55
Ag_2O-Au-719	61.69	10.94	27.37

The detailed information regarding the LSPR peak positions before and after oxygen treatment of bimetallic Au-Ag nanocages and the Au and Ag content of nanoparticles which are determined by inductively coupled plasma emission spectroscopy (ICPES) are provided in **Table 6.1**.

Energy dispersive X-ray (EDX) spectroscopy was performed on a single nanocage particle to determine the shell composition (**Figure 4.2 and Table 4.2**) [71, 72]. EDX revealed the O (at. %) content of Au-Ag nanocages increases after O_2 treatment (**Table 4.2**). Since the areas are selected from the shell of nanocages to determine the surface composition, there is a discrepancy between EDX and ICPES values which are obtained from the bulk analysis. The initial O content before O_2 treatment of nanocages is attributed to the chemisorbed oxygen caused by the external –OH group or the water molecule adsorbed on

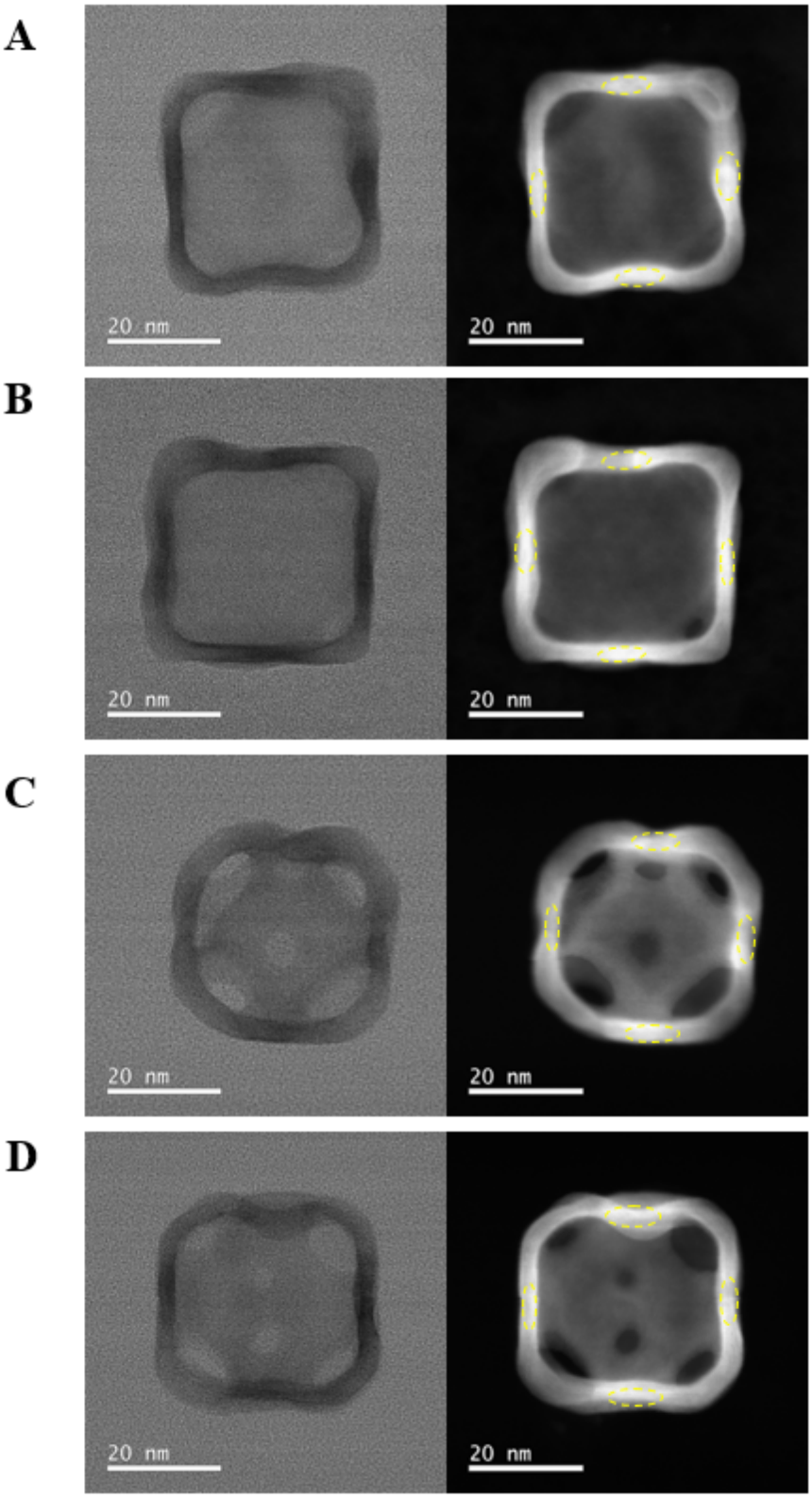

Figure 4.2: A) HRTEM and STEM images of A) Ag-Au-635, B) Ag_2O-Au-644, C) Ag-Au-715, and D) Ag_2O-Au-719 nanocages.

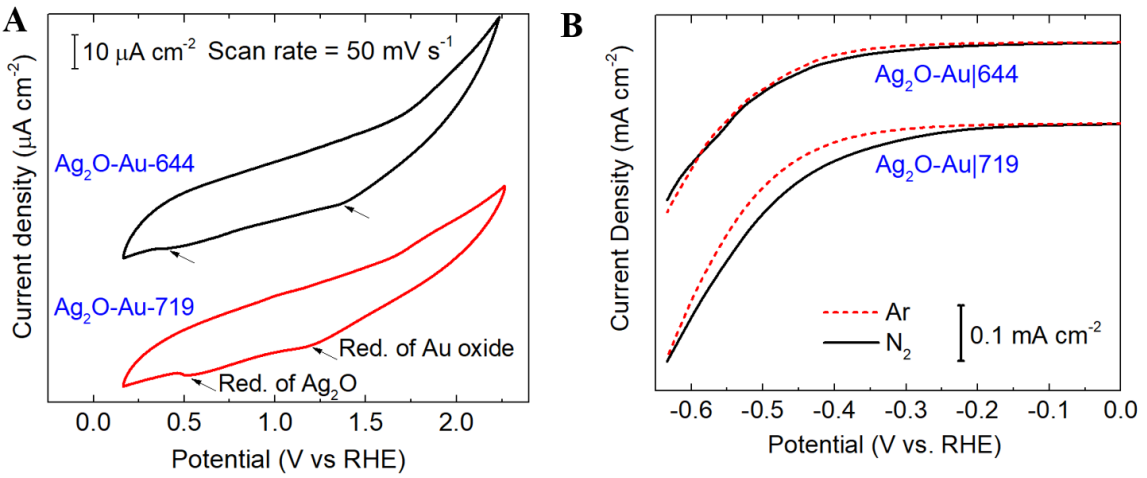

Figure 4.3: A) Cyclic voltammograms (CV) of Ag_2O-Au nanocages with various LSPR peak positions in Ar-saturated 0.1M LiOH (aq.) solution at a scan rate of 50 mV s^{-1}. The CV measurements were conducted in the rotating disk electrode (RDE) setup at room temperature. B) Linear sweep voltammetry (LSV) tests of Ag_2O-Au with LSPR peak positions at 644nm and 719nm in an Ar and N_2 saturated 0.5 M $LiClO_4$ (aq.) solution under ambient conditions with the scan rate of 10 mV s^{-1}.

the surface (**Table 4.2**).

Cyclic voltammograms of Ag_2O-Au nanocages are obtained in the three-electrode setup using rotating disk electrode (RDE) apparatus in an Ar-saturated 0.1M LiOH aqueous solution at a rotation rate of 1500 rpm and a scan rate of 50 mV s^{-1}. The peaks observed at potentials around 0.5 V vs. RHE, correspond to the reduction of silver (I) oxide in Ag_2O-Au-644 and Ag_2O-Au-719 nanocages. These reduction peaks are slightly larger compared to our previous study using Au-Ag-635 and Au-Ag-715 nanocages while the reduction peak for Au oxide at potential around 1.2 V vs. RHE remained relatively unchanged (**Figure 4.3A**) [68]. This observation suggests the effective conversion of Ag to Ag_2O after O_2 treatment of bimetallic Au-Ag nanocages and successful synthesis of Ag_2O-Au with various LSPR peak positions. This also informs that O_2 treatment of Ag in bimetallic Au-Ag nanocages to form Ag_2O is more effective than electrochemical oxidation of Ag. Linear sweep voltammetry (LSV) tests are carried out in Ar and N_2 saturated 0.5 M $LiClO_4$ (aq.) electrolyte in an H-type cell where a proton exchange membrane separates anodic and cathodic compartments. A neutral pH electrolyte is selected based on the

Table 4.3: Selectivity performance of hybrid plasmonic nanoparticles with various LSPR peak positions toward NRR.

Electrocatalyst	Potential (V vs. RHE)		
	-0.3	-0.4	-0.5
Ag-Au-635	52.3	48.7	45.1
Ag_2O-Au-644	46.4	36.7	9.1
Ag-Au-715	55.6	65.3	56.3
Ag_2O-Au-719	51.7	48.2	32.1

optimization of electrolyte's pH to obtain the highest electrocatalytic NRR activity [68]. The selectivity performance of Ag_2O-Au nanocages with various LSPR peak positions is evaluated toward NRR. Faradaic current is obtained by subtracting the capacitive current from the actual current recorded from LSV tests. For both electrocatalysts, the higher current density was achieved in N_2-saturated electrolyte compared to Ar-saturated electrolyte within the potential window of -0.2V to -0.5V vs. RHE (**Figure 4.3B**). In addition, within this potential window, the selectivity decreases for both electrocatalysts (i.e., Ag_2O-Au-644 and Ag_2O-Au-719) after O_2 treatment of bimetallic Au-Ag nanocages (**Table 5.2**). This clearly reveals the role of Ag in promoting the selectivity toward NRR. For instance, at the potential -0.4V vs. RHE, the selectivity decreases from 65.3% to 48.2% after O_2 treatment of Au-Ag-715 nanocages to make Ag_2O-Au-719. If Au atoms were the only active sites for NRR in bimetallic Au-Ag nanocages, the selectivity should remain unchanged after O_2 treatment of Au-Ag nanocages, as Au is a stable metal catalyst even after oxygenation. Since Ag_2O is a p-type semiconductor, at the reduction potentials (e.g., -0.4V vs. RHE) for NRR, it acts as a resistor rather than conductor, and therefore it is not an active site for NRR. However, Au atoms serve as primary active sites for NRR since for all potentials studied; higher selectivity has been achieved using Ag_2O-Au-719 compared to Ag_2O-Au-644 (**Table 5.2**). This is attributed to the higher Au content in Ag_2O-Au-719 compared to Ag_2O-Au-644 which were revealed by both ICPES and EDX analysis (**Table 6.1 and 4.2**). It is important to note that as potential moves from -0.3V to -0.5V, the selectivity toward

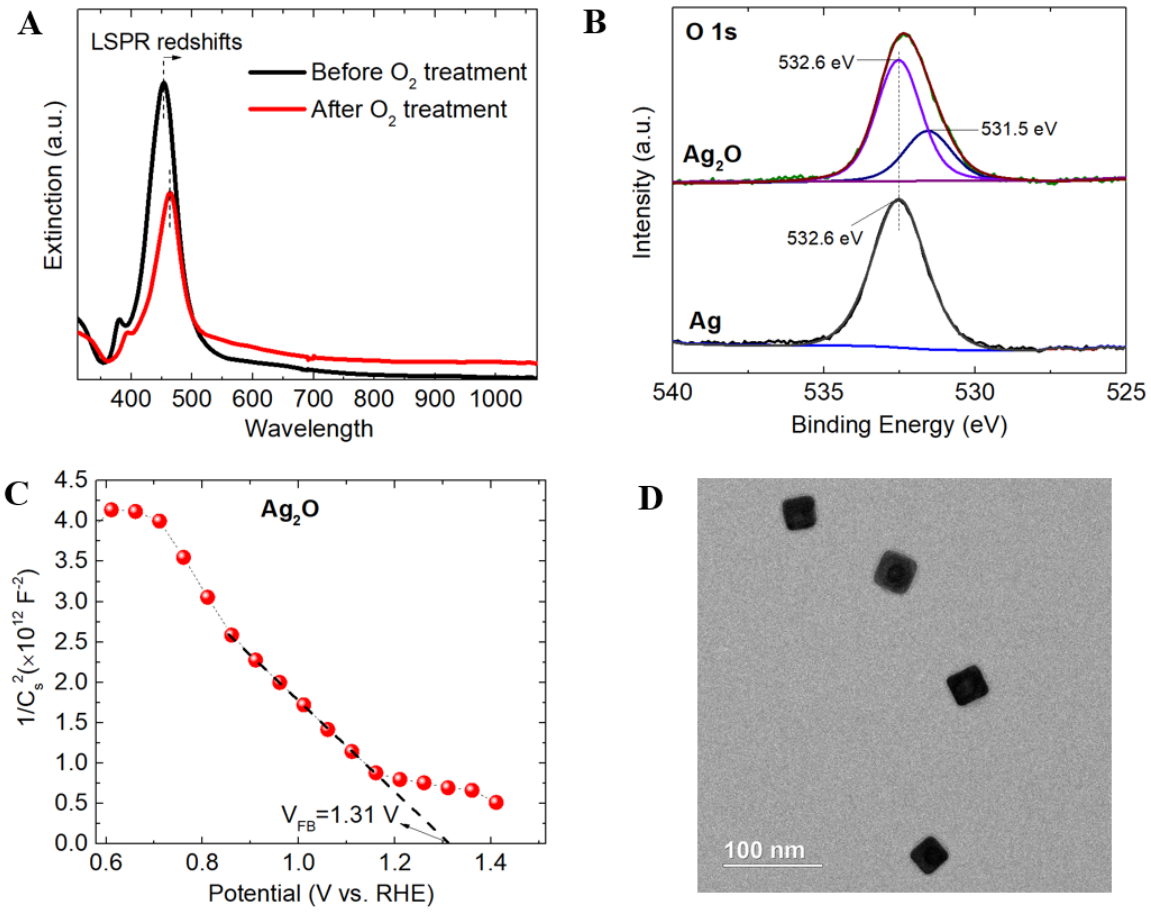

Figure 4.4: A) UV-vis extinction spectra of AgNCs before and after O_2 treatment. B) O 1s profiles of Ag nanocubes before and after O_2 treatment. All spectra were shift corrected using a standard reference C1s, C-C peak at 284.8 eV. C) Mott-Schottky plot of Ag_2O. A Mott-Schottky plot at a frequency of 1000 Hz was measured in 0.5 M $LiClO_4$ (aq.) solution under the dark condition. D) The TEM image of solid Ag_2O nanocubes.

NRR decreases from 51.7% to 32.7% for Ag_2O-Au-719 and from 46.4% to 9.1% for Ag_2O-Au-644. Moving toward more negative potentials than -0.6V, hydrogen evolution reaction (HER) becomes dominant. To determine the Fermi level of Ag_2O and better understand its response to the external applied potential, Ag_2O nanocubes are synthesized by O_2 treatment of AgNCs at the LSPR peak position of 445 nm. After O_2 treatment, the extinction spectra dampens and the LSPR peak position redshifts (11 nm), confirming the formation of Ag_2O nanocubes (**Figure 4.4A**). Furthermore, the O 1s profile for Ag nanocubes after O_2 treatment is deconvoluted into two peaks centered at 531.5 eV and 532.6 eV which are

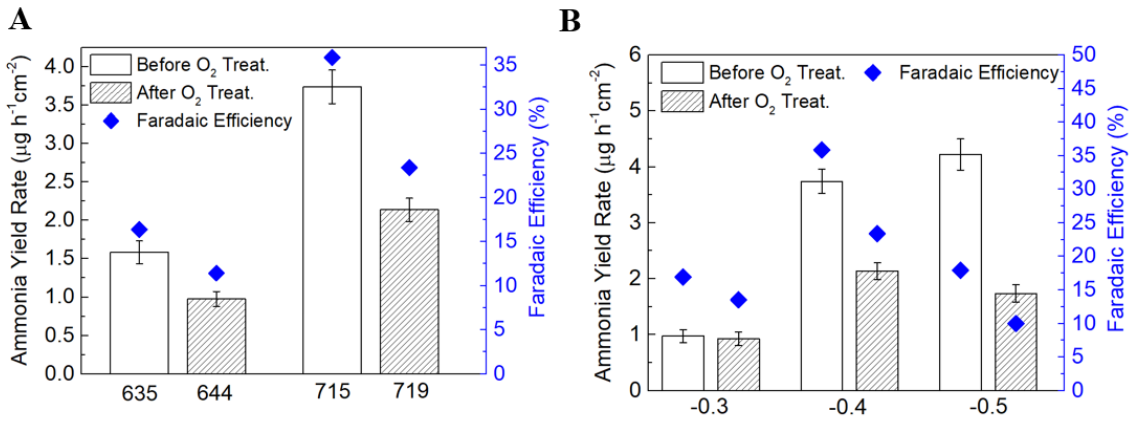

Figure 4.5: A) Ammonia yield rate and FE for bimetallic Au-Ag nanocages before and after O_2 treatment with various LSPR peak positions at a potential of -0.4 V vs RHE in 0.5 M $LiClO_4$ (aq.) solution. B) Ammonia yield rate and FE at various applied potentials in a 0.5 M $LiClO_4$ (aq.) solution.

attributed to the lattice oxygen atoms of Ag_2O and the chemisorbed oxygen caused by the external –OH group or the water molecule adsorbed on the surface (**Figure 4.4B**) [73, 74]. The latter peak is also observed in the O 1s profile for Ag nanocubes. The Mott–Schottky (MS) test is performed to determine the flat band potential (E_{fb}) and to confirm the semiconductor type of Ag_2O (**Figure 4.4C**). The E_{fb} is determined to be 1.31 V vs. RHE. The negative slope of the MS curve confirms that Ag_2O is a p-type semiconductor. At potentials more negative than E_{fb} for a p-type semiconductor such as Ag_2O, depletion region exists, and at potentials more positive than E_{fb} for a p-type semiconductor, accumulation region arises. In the depletion region for Ag_2O (the potential window for NRR is in the depletion region of Ag_2O), there are a few charge carriers available for charge transfer, and therefore electron transfer reactions happen very slowly. This behavior of Ag_2O is in line with the selectivity performance of Ag_2O-Au-644 and Ag_2O-Au-719 in which by sweeping the potential to more negative potentials (more negative from E_{fb}), the selectivity toward NRR continuously decreases (**Table 5.2**). The TEM image of solid Ag_2O nanocubes reveals the morphology of Ag nanocubes is maintained after the O_2 treatment of nanoparticles (**Figure 4.4D**).

Chronoamperometry (CA) tests are performed at -0.4V vs. RHE to determine the

ammonia yield rate and Faradaic efficiency (FE) for Ag_2O-Au-644 and Ag_2O-Au-719 nanocages (**Figure 4.5A**). The ammonia yield rate and FE decrease from 1.58 μg cm^{-2} h^{-1} and 16.4% to 0.98 μg cm^{-2} h^{-1} and 11.4% after O_2 treatment of Au-Ag-635 (**Figure 4.5A**). Higher ammonia yield rate and FE are obtained using Ag_2O-Au-719 (2.14 μg cm^{-2} h^{-1} and 23.4%) compared to Ag_2O-Au-644 which is consistent with the selectivity performance of these two electrocatalysts for NRR. Again, these results further confirm that although Ag acts as an active site for NRR, it has lower NRR activity compared to Au atoms. In addition, CA tests are performed using Ag_2O-Au-719 to determine the ammonia yield rate and FE at a series of applied potentials (**Figure 4.5B**). The same trend is observed for various applied potentials in which the ammonia yield rate and Faradaic efficiency decrease after O_2 treatment of bimetallic Au-Ag nanoparticles, with the highest ammonia yield rate and Faradaic efficiency, achieved at -0.4V vs. RHE (**Figure 4.5B**).

4.4 Conclusion

The chemical stability of the electrocatalyst during electrochemical NRR was evaluated by preparing Ag_2O-Au nanocages with two LSPR peak positions at 644 nm and 719 nm through the O_2 treatment of bimetallic Au-Ag nanocages. Electrocatalytic NRR activities of both Ag_2O-Au-644 and Ag_2O-Au-719 nanocages are lower than Au-Ag-635 and Au-Ag-715, suggesting the role of Ag in promoting the selectivity and activity for NRR. It was also observed that Au has higher activity toward NRR compared to Ag, as by redshifting the LSPR from 644 nm to 719 nm, the electrocatalytic NRR activity increased. This is attributed to the higher Au content in Ag_2O-Au-719 nanocages compared to Ag_2O-Au-644. This chapter emphasized the importance of an O_2-free electrolyte and careful synthesis and treatment of bimetallic Au-Ag nanocages to avoid the formation of Ag_2O in the cavity which causes a significant reduction in the electrocatalytic NRR activity.

CHAPTER 5

THE ROLE OF INCORPORATING PALLADIUM IN BIMETALLIC GOLD-SILVER NANOCAGES ON ELECTROCATALYTIC ACTIVITY OF NITROGEN REDUCTION REACTION

5.1 Introduction

Single-atom and hybrid Au electrocatalysts have shown relatively high activity due to the ability of Au to strongly adsorb and break N≡N through the associative mechanism, with further sequential hydrogenation to form adsorbed N_2H_x species ($1<x<4$); the rate-determining step is N_2 dissociation (reduction of N_2^* to generate N_2H^*) [52, 54, 75, 76, 77, 78]. It has been demonstrated that the rate-determining step kinetics is accelerated on transition metal hydrides, where H^* species on the catalyst surface directly react with the dissolved nitrogen in the electrolyte to form N_2H_x [79, 80, 81]. In addition, a lithium mediated strategy ($Li^+ \xrightarrow{e^-} Li \xrightarrow{N_2} Li_3N \xrightarrow{H_2O} NH_3$) on the transition metal catalyst could enhance the electrochemical NRR activity at low temperatures due to lithium's unique ability to break the nitrogen triple bond, followed by hydrogenation to generate ammonia [82, 83, 84].

In Chapters 2, 3, and 4, the use of shape and pore-size controlled Au and bimetallic Au-Ag nanocages, with tunable localized surface plasmon resonance (LSPR) peak positions, as electrocatalysts for ammonia synthesis in an ionic aqueous solution with Faradaic efficiency $>35\%$ was studied. The optimization of the structure, morphology, and composition is critical to enhancing the rate of electro-reduction of N_2 to NH_3. It was found that Au is catalytically more active than Ag in both photo- and electrochemical NRR. Therefore, it is desired to replace Ag with another catalytic transition metal with higher NRR activity. This new metal must correctly modify the electronic structure of the nanoparticles by shift-

ing the d-band center to ensure the optimum binding energy of an adsorbed species on the catalyst surface [85]. It was demonstrated that the electrochemical NRR takes place on the surface of Pd catalyst through the formation of Pd hydrides (PdH_x) at low overpotentials, followed by surface hydrogenation reactions [81]. The formation of PdH_x could weaken Pd-H bonding (proton adsorption strength on the Pd surface), leading to enhanced binding of Pd surface with N_2 and N-containing adsorbates. In this chapter, the role of incorporating palladium into bimetallic Au-Ag nanostructures on the electrocatalytic NRR activity in 0.5M $LiClO_4$ (aq.) solution will be discussed. Since the reduction potential of Pd ($\sim$0.65 V vs. RHE) is higher than that of Ag ($\sim$0.5 V vs. RHE) but lower than that of Au ($\sim$1.2 V vs. RHE), Ag can only be replaced with Pd in the galvanic replacement process after the addition of Pd salt (K_2PdCl_4 (aq.)) in the bimetallic Au-Ag nanostructures template. The red shifting of the LSPR peak position of the trimetallic nanostructures indicates either the replacement of Ag with Pd or the growth of Pd on Au. Energy input (MWh ton^{-1} NH_3) and production energy efficiency (%) of ammonia in the N_2 electrolysis system will be presented and the results will be compared with the state-of-the-art Haber-Bosch system.

In-situ and *operando* surface-enhanced spectroscopy is a technique well suited to probe electrochemical reactions at the electrode/electrolyte interface, and several studies have shown a great success for studying electrocatalytic water splitting and CO_2 reduction reactions [86, 87, 88]. Recently, surface-enhanced infrared absorption spectroscopy (SEIRAS) was used to determine electrocatalytic NRR mechanisms on Au and Pt surfaces [53]. *Operando* surface enhanced Raman spectroscopy (SERS) allows for the detection of intermediate species even in low abundance and is used for the determination of NRR mechanisms using trimetallic Au-Ag-Pd nanostructures.

5.2 Experimental Methods

5.2.1 Nanoparticle Synthesis

Bimetallic porous Au-Ag nanocages with an LSPR peak position at 650 nm are synthesized by adding $HAuCl_4$ (aq.) solution to a solid silver nanocubes (AgNCs) solution through the galvanic replacement method [89]. The Au-Ag nanocages are cleaned by centrifugation two times at 10,000 rpm for 10 min. Then, K_2PdCl_4 (0.006 M (aq.)) is gradually injected to the 100 ml Au-Ag solution (0.5 mL per 5 min) at room temperature (20°C) under constant shaking in a 150 ml round-bottomed flask until the LSPR peak positions redshifts to 750 nm and 850 nm (approximately 1.5 mL of K_2PdCl_4 (aq.) for Au-Ag-Pd-750 and 2.5 mL of K_2PdCl_4 for Au-Ag-Pd-850). Unlike the galvanic replacement of Au^{3+} ions and Ag that takes place at the water boiling temperature, the galvanic replacement of Ag with Pd^{2+} takes place at room temperature, as the reaction of Pd ions with Ag is more active compared to that of the Au ions. The resulting trimetallic Au-Ag-Pd nanoparticles are washed two times by centrifugation at 12,000 rpm for 10 min. The precipitated nanoparticles are dispersed in DI water for future use.

5.2.2 Production Energy Efficiency Calculation

The production energy efficiency (η_{PEE}) of the electrolysis system is calculated according to the equation 5.1:

$$\eta_{PEE}\,(\%) = \frac{\Delta\, G\ for\ ammonia\ generation\ (J\ mol^{-1}) \times\ ammonia\ generated\ (mol)}{\int IVdt\ (J)} \times\ 100 \tag{5.1}$$

The free energy for NH_3 generation (ΔG) is 339 kJ mol^{-1} and $\int IVdt$ (J) is the electricity consumed in the process (energy input). Here, V (V) is the full cell potential and is calculated according to the equation 5.2:

$$V = (E_{anode} - E_{cathode}) + IR \tag{5.2}$$

The cathode potentials (NRR) were measured in the three-electrode set up for each condition. The anode potential is estimated as the sum of the thermodynamic potential for water oxidation (1.23 V vs. RHE) and OER overpotential ($\sim$0.45V on the Pt mesh) [90]. The resistance (R) between the anode and the cathode in our setup is measured to be 75 Ω. This indicates that even for the case with the highest average current density (0.4 mA cm^{-2} at -0.5V vs. RHE using Au-Ag-Pd-850), the resistive losses (IR) will be $\sim$30 mV.

5.2.3 Determination of the Electrochemical Surface Area (ECSA) of the Nanoparticle

The ECSA of the catalyst is determined from the charge associated with the reduction peak of Pd oxide (PdO) after double-layer correction and is normalized to the Pd loading on the working electrode and the charge density of 424 μC cm^{-2} according to the following equation 5.3:

$$ECSA\ (\frac{cm^2_{Pd}}{g_{Pd}}) = \frac{Q\ (\mu\ C\ cm^{-2})}{424\ \mu\ C\ cm^{-2}_{Pd} \times electrode\ loading\ (g_{Pd}\ cm^{-2})} \tag{5.3}$$

where Q (μC cm^{-2}) is the charge associated with the reduction peak of Pd oxide after double layer correction and is calculated according to the equation 5.4:

$$Q = \frac{\int iV}{\nu} \tag{5.4}$$

where i is the current density (μA cm^{-2}), V is the potential (V), and v (V s^{-1}) is the scan rate.

5.2.4 Turnover Frequency Calculation

The turnover number (TON) per active Pd, Au, and Ag sites in trimetallic nanoparticles is determined by dividing the total moles of ammonia produced within 72 h to the total moles

of active sites (i.e., Pd, Au, and Ag) according to the equation 5.11:

$$TON = \frac{N_{ammonia}}{N_{Pd} + N_{Au} + N_{Ag}} \tag{5.5}$$

The concentration of each element in the nanoparticle is provided in Table 5.1. By dividing the concentration of each atom by the molecular weight, the concentration with the unit of mol L^{-1} is obtained. The volume of the nanoparticle drop-casted on the substrate is 300 μL.

$$N_{Pd} = \frac{2.77\ mg\ L^{-1}}{106.42 \times 1000\ mg\ mol^{-1}} \times 300 \times 10^{-6} L \simeq 7.81 \times 10^{-9}\ mol \tag{5.6}$$

$$N_{Au} = \frac{1.29\ mg\ L^{-1}}{196.97 \times 1000\ mg\ mol^{-1}} \times 300 \times 10^{-6} L \simeq 1.965 \times 10^{-9}\ mol \tag{5.7}$$

$$N_{Ag} = \frac{1.35\ mg\ L^{-1}}{107.87 \times 1000\ mg\ mol^{-1}} \times 300 \times 10^{-6} L \simeq 3.755 \times 10^{-9}\ mol \tag{5.8}$$

The total moles of active sites is:

$$N_{total} = N_{Pd} + N_{Au} + N_{Ag} = 7.81 \times 10^{-9} + 1.965 \times 10^{-9} + 3.755 \times 10^{-9} = 1.353 \times 10^{-8} mol \tag{5.9}$$

It is important to note that, this calculation is valid with the assumption that all Pd, Au, Ag atoms are fully converted by aqua regia (HCl+HNO_3 (3:1) vol. %) to their ionic form for the ICPES measurement. The total amount of ammonia produced using Au-Ag-Pd-850 nanoparticles over 72 h is:

$$N_{ammonia} = \frac{13.62\ \mu g\ cm^{-2}\ h^{-1} \times 72\ h \times 1\ cm^2}{17 \times 10^6\ \mu g\ mol^{-1}} = 5.77 \times 10^{-5} mol\ of\ NH_3 \tag{5.10}$$

The TON within 72 h is:

$$TON = \frac{5.77 \times 10^{-5}\ mol\ of\ NH_3}{1.353 \times 10^{-8}\ mol\ of\ active\ sites} = 4264.6 \tag{5.11}$$

The TOF is defined as TON per unit time, which is given by:

$$TOF = \frac{4264.6}{72} \sim 59\ h^{-1} \tag{5.12}$$

5.2.5 *Operando* Surface Enhanced Raman Spectroscopy (SERS) measurements

Spectroelectrochemistry is a powerful technique that combines spectroscopy and electrochemistry. A potentiostat is used to apply potential on a SERS active substrate that is then monitored by changes in a spectrum. The spectroelectrochemical cell is developed to *operando* probe the trace of NH_3 and possible intermediate species produced at the electrode/electrolyte interface. The *Operando* SERS cell consisted of machined Teflon parts and fittings outfitted with an Au counter electrode, an Ag/AgCl reference electrode, an Au working electrode with an area of 0.01 cm^2. 1μl of prepared nanoparticles was drop casted onto Au and left to dry under ambient conditions for 2 hours. Before each test, the electrolyte solution (0.5 M $LiClO_4$ (aq.)) was purged with N_2 or Ar for 30 minutes. For all *operando* SERS measurements, a Renishaw RM1000 spectromicroscopy system was used with an air-cooled Ar laser (Mellos Griot) with a wavelength of 532 nm and a laser power of 12 mW. An Olympus LMPlanFI 20×/NA0.40 objective was used to focus the beam. The objective gave a spot size diameter of 2 μm. The slit size was 10 μm to minimize any distortion of the peaks. The WiRE^{TM} software by Renishaw was used to set an acquisition time of 10 s per scan. Cyclic voltammetry (CV) tests were carried out at the potential range of 0.97 to -0.63 V vs. RHE with the scan rate of 2.5 mV s^{-1} in N_2- or Ar-saturated 0.5M $LiClO_4$ (aq.) solution.

5.3 Results and Discussion

Bimetallic porous Au-Ag nanocages with an LSPR peak position at 650 nm are synthesized by the galvanic replacement method by adding $HAuCl_4$ (aq.) solution to a solution of solid silver nanocubes (AgNCs) (**Figure 5.1A and B**) [91]. Trimetallic Au-Ag-Pd nanos-

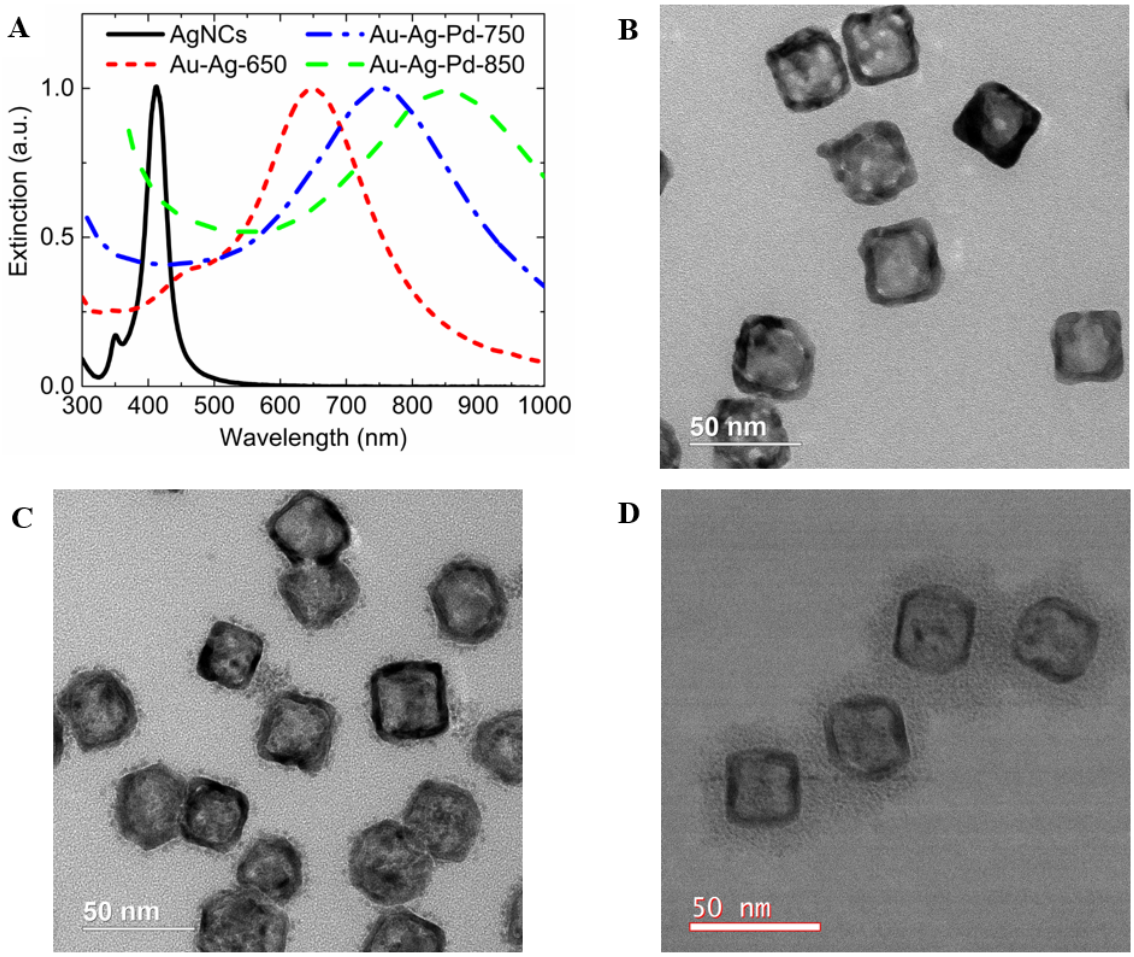

Figure 5.1: A) UV-vis extinction spectra of silver nanocubes, bimetallic Au-Ag nanocages, and trimetallic Au-Ag-Pd nanoparticles with the LSPR peak positions at 750 nm and 850 nm. TEM images of B) Au-Ag-650, C) Au-Ag-Pd-750, and D) Au-Ag-Pd-850. Silver nanocubes with the LSPR peak position at 412 nm are used as a template to synthesize various bimetallic and trimetallic nanoparticles.

tructures are synthesized by adding K_2PdCl_4 (aq.) solution to the porous bimetallic Au-Ag nanocages dispersed in DI water with the LSPR peak at 650 nm. The volume of the Pd^{2+} precursor added to the Au-Ag template, and subsequent reduction of Pd^{2+} to Pd^0 (two Ag atoms are replaced with one palladium atom), is controlled by measuring the redshift in the LSPR peak positions of nanoparticles. As the amount of Pd salt solution increases, the amount of redshift and the LSPR bandwidth increases (**Figure 5.1A**). Excessive addition of Pd salt results in aggregation and collapsing of the nanocages. The LSPR peak of the resulting trimetallic Au-Ag-Pd redshifts from 650 nm to 850 nm; indicating the replacement

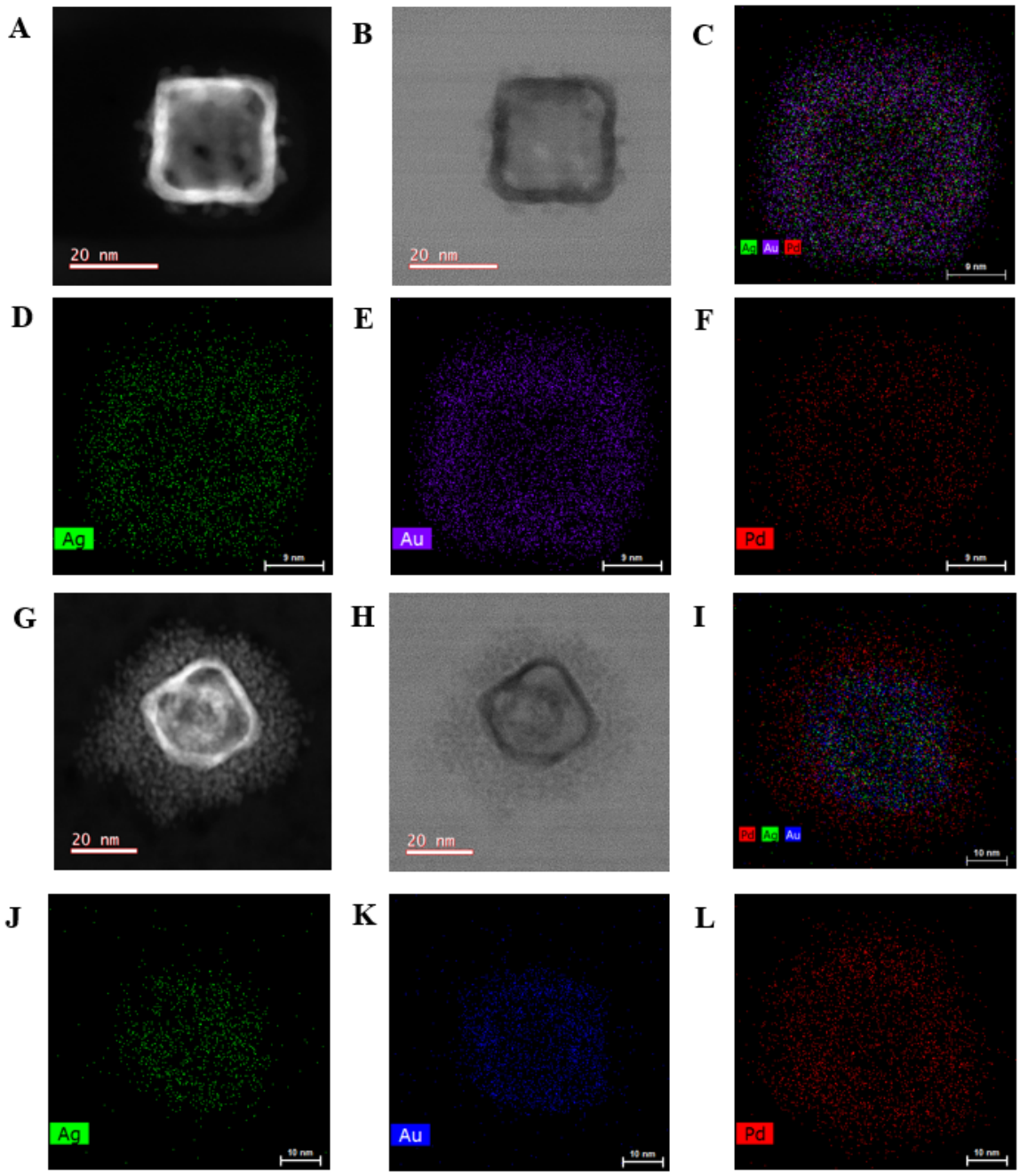

Figure 5.2: STEM (A), HRTEM (B), and EDX elemental mapping (C, D, E, F) of a representative single Au-Ag-Pd-750 nanoparticle. STEM (G), HRTEM (H), and EDX elemental mapping (I, J, K, L) of a representative single Au-Ag-Pd-850 nanoparticle.

of the remaining Ag atoms in the Au-Ag nanocages with Pd atoms (galvanic replacement) or the growth of Pd on Au (**Figure 5.1**). Due to the lattice mismatch between Pd (3.890 Å) and Au (4.079 Å), when Pd^{2+} precursor is added to the solution of Au-Ag nanocages,

Table 5.1: Au, Ag, and Pd concentrations of nanoparticles are determined by inductively coupled plasma emission spectroscopy (ICPES). The electrochemical surface areas (ECSA) of nanoparticles are determined based on the reduction peak of Au oxide and Pd oxide during CV measurements in Ar-saturated 0.1M LiOH solution at a scan rate of 50 mV s^{-1}.

Electrocatalyst	Ag Conc. (μg mL^{-1})	Au Conc. (μg mL^{-1})	Pd Conc. (μg mL^{-1})	Au Content (at. %)	Pd content (at. %)	$ECSA_{Au}$ (m^2 g^{-1})	$ECSA_{Pd}$ (m^2 g^{-1})
Ag-Au-650	2.68	1.32	NA	21.25	NA	23.3	NA
Au-Ag-Pd-750	1.88	1.31	1.23	18.66	32.43	20.8	291.4
Au-Ag-Pd-850	1.35	1.29	2.77	14.52	57.72	22.2	345.4

islands of palladium are formed on the Au surface. By further addition of the Pd salt solution, the islands are grown more, building a highly rough and porous surface (**Figure 5.1C and D**).

Scanning transmission electron microscopy (STEM) and energy dispersive X-ray (EDX) spectroscopy are performed on a single trimetallic nanostructure to determine the structure, the elemental composition, and distribution of Au-Ag-Pd-750 and Au-Ag-Pd-850 nanoparticles (**Figure 5.2**). For Au-Ag-Pd-750, Pd islands are distributed in the Au-Ag nanocages structure, indicating the successful incorporation of Pd into bimetallic Au-Ag nanocages, and the synthesis of trimetallic Au-Ag-Pd nanoparticles (**Figure 5.2A-F**). By increasing the amount of Pd salt solution and red shifting the LSPR peak from 750 nm to 850 nm, a continuous porous layer of Pd is formed at the exterior surface of the nanoparticles (**Figure 5.2G-L**). In addition, inductively coupled plasma emission spectroscopy (ICPES) measurements reveal that by adding the Pd salt solution into the Au-Ag nanocages, the Au content remains relatively unchanged while the Ag content decreases from 2.68 mg L^{-1} to 1.35 mg L^{-1} when the LSPR peak redshifts from 650 nm to 850 nm (**Table 5.1**). This indicates that the galvanic replacement of Ag atoms with Pd ions is one of the mechanisms for the reduction of Pd^{2+} to Pd^0 in which the concentration of Pd increases to 1.23 mg L^{-1} and 2.77 mg L^{-1} as the LSPR peak redshifts to 750 nm and 850 nm. The stoichiometric balance between Ag and Pd (Pd^{2+} (aq.) + $2Ag^0$ (s) $\rightarrow$ Pd^0 (s) + $2Ag^+$ (aq.)) and the Pd and Ag contents in Table 5.1 reveal that the reduction of Pd^{2+} to Pd^0 is also accomplished through the layer by

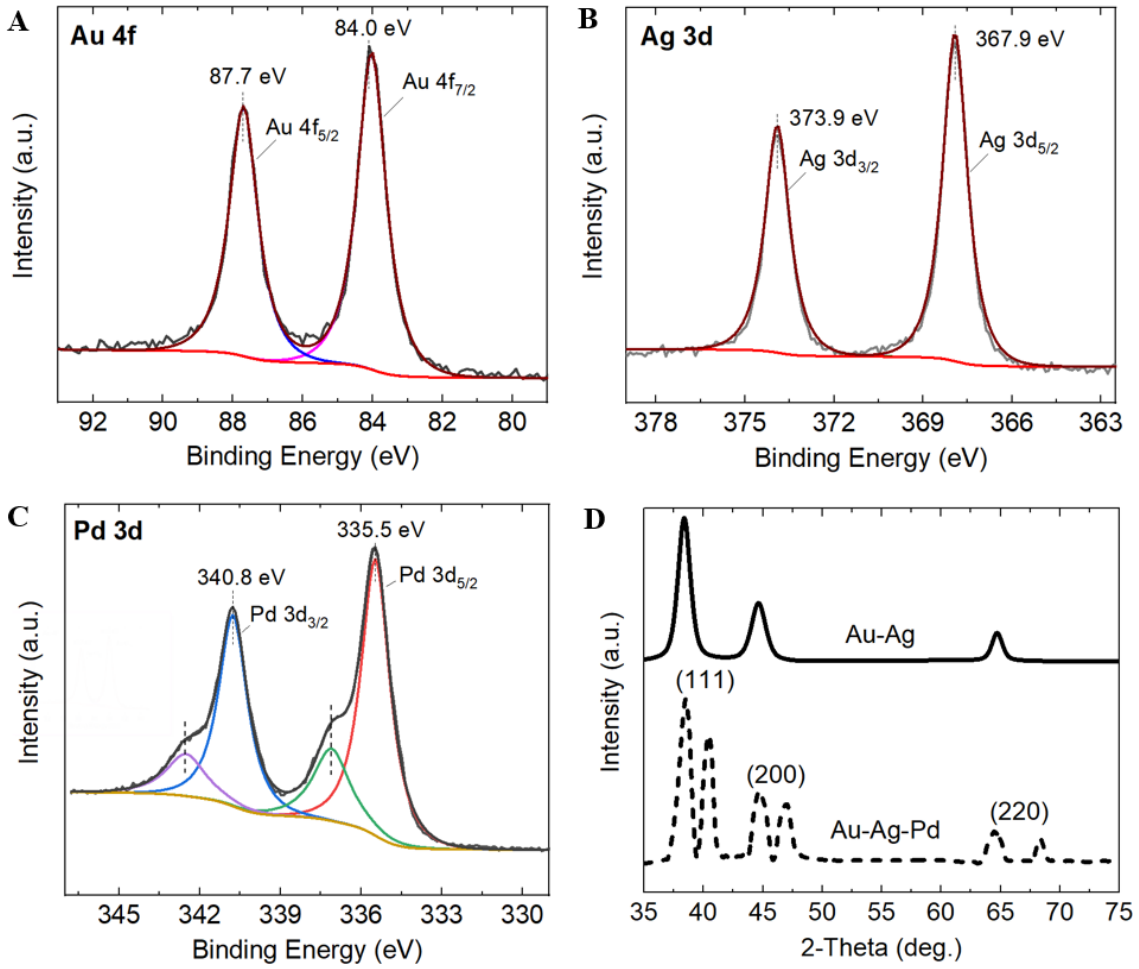

Figure 5.3: XPS spectra of A) Au 4f, B) Ag 3d, and C) Pd 3d of Au-Ag-Pd-850 nanoparticles. All spectra were shift corrected using a standard reference C1s, C-C peak at 284.8 eV. D) XRD pattern of Au-Ag and Au-Ag-Pd nanocages. The Pd diffraction peaks shift to higher 2θ angles due to the smaller lattice parameter (3.890 Å) compared to those of the Au (4.079 Å) and Ag (4.086 Å).

layer growth on Au atoms (**Figure 5.2I**) [92, 93].

X-ray photoelectron spectroscopy (XPS) results of Au-Ag-Pd-850 nanoparticles reveal a spin-orbit doublet for Au 4f at 84.0 eV and 87.7 eV, indicating that the zero-valence state of Au (Au^0) is preserved after the addition and reduction of the Pd^{2+} precursor in bimetallic Au-Ag nanocages (**Figure 5.3A**). The Ag 3d doublet energy peaks at 367.9 eV and 373.9 eV slightly shifts to lower binding energy (0.2 eV) compared to the Ag 3d doublet in bimetallic Au-Ag nanocages; this is attributed to the interaction and charge distribution of metallic Ag_0 and Pd precursors that occur after galvanic replacement (**Figure 5.3B**) [94].

The Pd 3d spectrum is deconvoluted into two pairs of doublets. The doublet peaks at 335.8 eV, and 340.8 eV correspond to Pd at zero-valence state, suggesting the successful incorporation of Pd^0 in the bimetallic Au-Ag nanocages. The doublet peaks at higher binding energies and with lower intensities than those of zero-valence Pd metal (337.1 eV and 342.5 eV) are attributed to the oxidized Pd states (Pd^{n+}) (**Figure 5.3C**) [95]. The x-ray diffraction (XRD) patterns of Au-Ag-Pd and Au-Ag nanocages indicate the presence of metallic Pd which is evident from the three distinct peaks at higher 2θ angles (40.4°, 46.9°, 68.4°) in Au-Ag-Pd compared to those of the Au-Ag nanocages (38.3°, 44.6°, 64.7°) (**Figure 5.3D**).

The electrochemical surface area (ECSA) of the Au-Ag-Pd nanoparticles is determined using a three-electrode cell with a rotating disk electrode (RDE) and performing cyclic voltammetry (CV) in an Ar-saturated 0.1M LiOH (aq.) at zero rotation rate at a scan rate of 50 mV s^{-1}. The $ECSA_{Pd}$ is calculated from the reduction peak of Pd oxide after double-layer correction and a charge density of 424 μC $cm^{-2}{}_{Pd}$ (**Figure 5.4A** and **Table 5.1**). The ECSAs of the nanoparticles are normalized to the Pd and Au loading on the working electrode, obtained from ICPES measurements (**Table 5.1**). Au-Ag-Pd-850 has a higher surface area (345.4 m^2 g^{-1}) compared to the Au-Ag-Pd-750 (291.4 m^2 g^{-1}). This can be attributed to the existence of a thick porous layer of Pd at the exterior surface of the Au-Ag-Pd-850 nanoparticles, which increases the ECSA for catalytic reactions. It is well known that rough surfaces are catalytically more active than smooth surfaces, as atoms present on rough surfaces are more thermodynamically active [13, 92]. The $ECSA_{Pd}$ obtained using our trimetallic Au-Ag-Pd-850 nanoparticles is approximately five times higher than the $ECSA_{Pd}$ of the commercial Pd/C catalysts [66, 81]. Although the reduction peak area of Pd oxide is remarkably higher than that of Ag oxide, due to the comparable reduction potentials of these two metal oxides, the reduction peak area of Ag oxide is subtracted from the actual reduction peak area centered at around 0.5 V vs. RHE to determine the $ECSA_{Pd}$ (**Figure 5.4A**). The observed negative shift in the electrochemical reduction of Pd oxide ($\sim$0.1 V) in our trimetallic nanostructures, compared to the pure Pd, is attributed

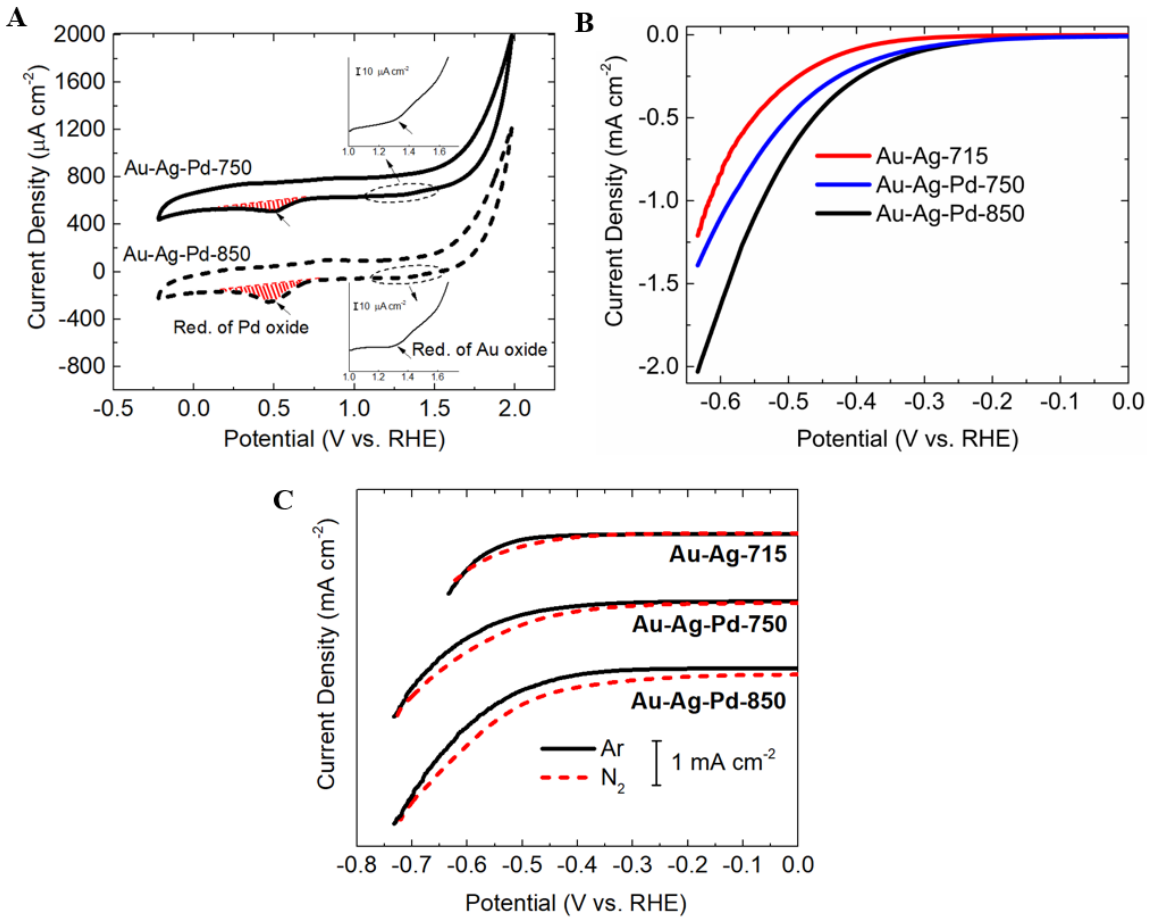

Figure 5.4: A) Cyclic voltammograms (CV) of Au-Ag-Pd-750 and Au-Ag-Pd-850 in Ar-saturated 0.1M LiOH (aq.) at a scan rate of 50 mV s^{-1}. The CV measurements were conducted in the rotating disk electrode (RDE) setup at the stagnant electrode condition at room temperature. B) Linear sweep voltammograms (LSV) of various catalysts in N_2-saturated 0.5 $LiClO_4$ (aq.). C) LSV tests of Au-Ag-Pd-750 and Au-Ag-Pd-850 in an Ar- and N_2-saturated 0.5 M $LiClO_4$ (aq.) under ambient conditions with the scan rate of 10 mV s^{-1}.

to the slight alloying of Pd and Ag at their interface during the galvanic replacement reaction [96]. The $ECSAs_{Au}$ of trimetallic Au-Ag-Pd nanoparticles is comparable (~0.93) to the $ECSAs_{Au}$ of bimetallic Au-Ag nanocages (**Table 5.1**) [68]. This indicates that the incorporation of Pd in bimetallic Au-Ag nanocages does not result in blocking the Au active sites for electrochemical NRR and confirms the preservation of the hollow structure in trimetallic nanoparticles where Au, Ag, and Pd can act as catalytically active centers for the reaction. Linear sweep voltammetry (LSV) tests are performed in N_2-saturated 0.5 M

Table 5.2: Selectivity performance of trimetallic Au-Ag-Pd nanoparticles with LSPR peak positions at 750 nm and 850 nm toward NRR.

Electrocatalyst	Potential (V vs. RHE)		
	-0.3	-0.4	-0.5
Au-Ag-Pd-750	56.8	58.8	34.1
Au-Ag-Pd-850	76.3	67.8	44.8

$LiClO_4$ (aq.) electrolyte in an H-type cell, where a proton exchange membrane separates anodic and cathodic compartments. A remarkably higher current density is achieved using Au-Ag-Pd-750 and Au-Ag-Pd-850 nanoparticles compared to the bimetallic Au-Ag-715 nanocages (the best bimetallic Au-Ag nanocatalyst with the highest electrocatalytic NRR activity) (**Figure 5.4B**). For instance, at an applied potential of -0.3V vs. RHE, the current density increases $\sim$4.8 and $\sim$3.7 times for Au-Ag-Pd-850 and Au-Ag-Pd-750 compared to the Au-Ag-715. This observation is consistent with significantly higher $ECSA_{Pd}$ compared to the $ECSA_{Au}$ (**Table 5.1**) in trimetallic Au-Ag-Pd nanoparticles, which provides more active sites for nitrogen adsorption and reduction. Although achieving high current density at low overpotentials does not necessarily indicate the high selectivity and activity of an electrocatalyst toward NRR, it is the primary step toward the high production rate that is mandatory for reaching the overarching goal of commercializing electrochemical NRR for sustainable ammonia production.

The selectivity performance ($\frac{I_{N_2}-I_{Ar}}{I_{N_2}} \times 100$) of trimetallic Au-Ag-Pd nanoparticles is evaluated toward NRR. For both electrocatalysts (i.e., Au-Ag-Pd-750 and Au-Ag-Pd-850), the higher current density was achieved in N_2-saturated electrolyte compared, to the Ar-saturated electrolyte, within the wide potential window (**Figure 5.4C**). Unlike the bimetallic Au-Ag nanocages demonstrated in previous chapters, the selectivity performance of electrocatalysts improves at low overpotentials (0 V to -0.3 V vs. RHE) toward NRR after the incorporation of Pd into the bimetallic Au-Ag nanocages (**Figure 5.4C**). In addition, both electrocatalysts are selective toward NRR until the high negative potential of

$\sim$-0.75 V vs. RHE, even with an enhanced current density that is achieved using trimetallic nanostructures. This expands the selectivity of an electrocatalyst toward NRR in negative potentials by 0.15 V over that of Au-Ag nanocages. Moving toward more negative potentials than -0.75V, a hydrogen evolution reaction (HER) becomes dominant. Here, I focus on the potential window of -0.3 to -0.5 V vs. RHE, which is a compromise of obtaining high current density and selectivity. It is important to note that achieving a high current density for NRR is crucial to decrease the capital cost, leading to the commercialization of electrochemical NRR. At all three applied potentials, the selectivity is higher for Au-Ag-Pd-850 than for the Au-Ag-Pd-750; this is attributed to the higher Pd content and lower Ag content of Au-Ag-Pd-850 nanoparticles (**Table 5.2**). Even though the selectivity is not substantially higher in trimetallic Au-Ag-Pd nanostructures than in the bimetallic Au-Ag nanocages, due to the enhanced current density obtained (I_{N_2}) using Au-Ag-Pd nanoparticles, the corresponding current density toward NRR (I_{N_2} - I_{Ar}) is much more pronounced after incorporation of Pd into Au-Ag nanocages.

Chronoamperometry (CA) tests are performed at a series of applied potentials using Au-Ag-Pd-750 and Au-Ag-Pd-850 nanoparticles to determine the ammonia yield rate and FE (**Figure 5.5A, B**). The highest ammonia yield rate (13.74 μg cm^{-2} h^{-1}) is obtained at -0.4 V corresponding to an FE of 44.11% while the highest FE (48.94%) is achieved at -0.3V (ammonia yield rate = 5.80 μg cm^{-2} h^{-1}) using Au-Ag-Pd-850. The higher ammonia yield rate but lower FE at -0.4V, compared with -0.3V, is attributed to the compromise between increasing current density and competitive selectivity toward HER rather than NRR. For all potentials tested, both the NH_3 yield rate and the FE are higher when Au-Ag-Pd-850 is used than when Au-Ag-Pd-750 is used. This result suggests that Pd content and $ECSA_{Pd}$ of nanoparticles have a role in promoting the electrocatalytic NRR activity (**Figure 5.5B**). In addition, greater Pd content in Au-Ag-Pd-850 compared to that of Au-Ag-Pd-750 results in an upshift of the d-band center ($E - E_f$) from -4.45 eV to -3.73 eV, which was determined via ultraviolet photoelectron spectroscopy (UPS) measurements (**Figure 5.6A, B**). This

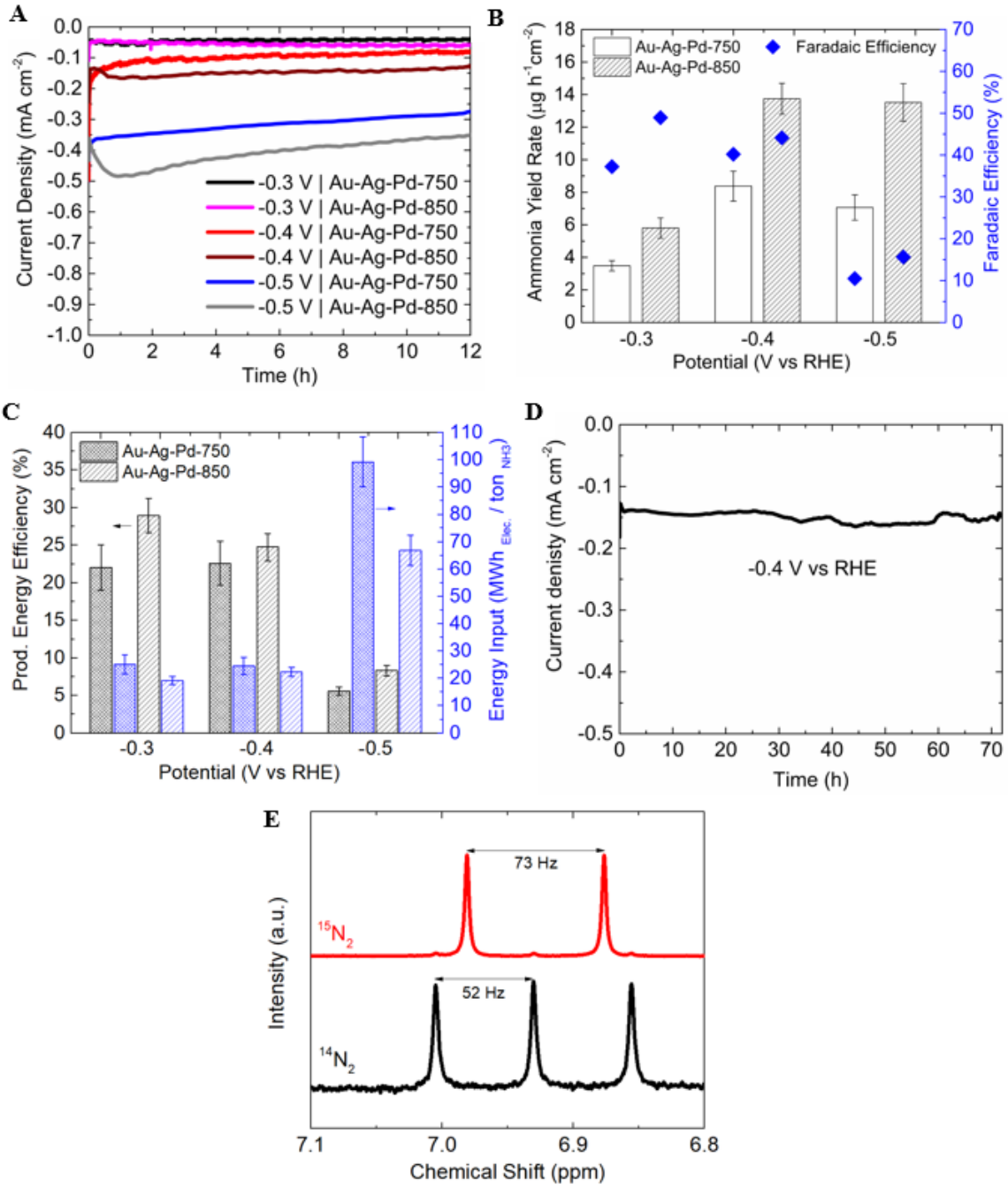

Figure 5.5: A) CA results of Au-Ag-Pd-750 and Au-Ag-Pd-850 nanocatalysts at a series of potentials. B) Ammonia yield rate and Faradaic efficiency at various potentials in 0.5 M $LiClO_4$ (aq.) solution using Au-Ag-Pd-750 and Au-Ag-Pd-850 nanocatalysts. C) Production energy efficiency and energy input at various applied potentials using Au-Ag-Pd-750 and Au-Ag-Pd-850 nanocatalysts. The intense bars (black bars show production energy efficiency and blue bars show energy input) represent Au-Ag-Pd-750 and the medium bars represent Au-Ag-Pd-850. D) CA test for the stability of the Au-Ag-Pd-850 at -0.4V vs. RHE in 0.5 M $LiClO_4$ (aq.) solution. E) 1H-NMR spectra of samples after electrochemical $^{15}N_2$ ($^{14}N_2$) reduction reaction at -0.4V vs. RHE for 4 h in 0.5M $LiClO_4$ (aq.) solution.

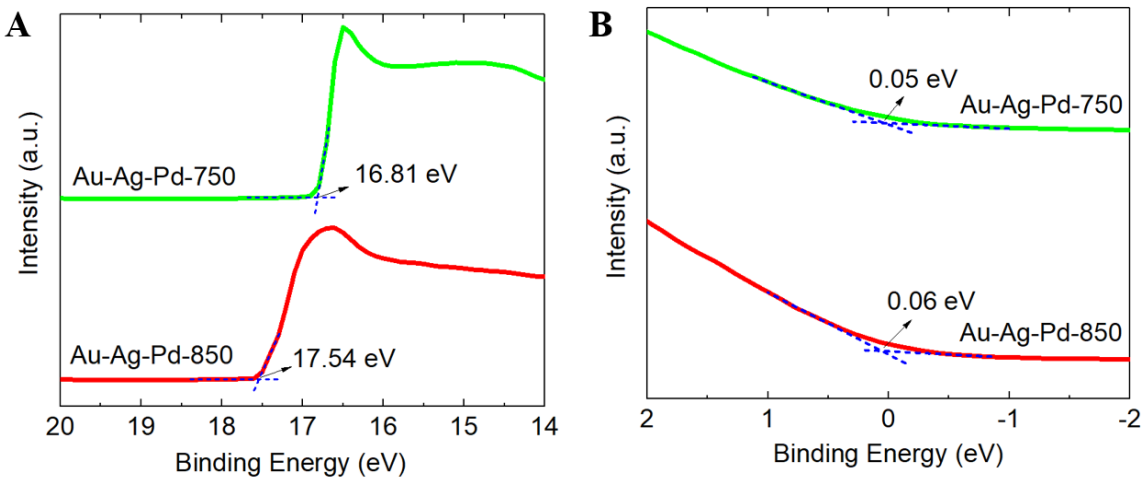

Figure 5.6: A) UPS spectra of trimetallic Au-Ag-Pd nanoparticles. A) The secondary electron cut-off ($E_{cut\text{-}off}$) and B) the Fermi edge (E_{FE}) are measured with He1 (21.22 eV) source radiation. The work function (ϕ) is calculated by 21.21 eV – ($E_{cut\text{-}off}$ – E_{FE}). The ϕ of Au-Ag-Pd-750 and Au-Ag-Pd-850 nanoparticles are determined to be 4.45 and 3.73 eV.

leads to improved binding strength of N-containing adsorbates with the catalyst surface, which is a crucial step for engineering selective and active NRR catalysts in an aqueous solution where selectivity is a major challenge.

Here, I also report the two critical parameters (i.e., production energy efficiency (%) and energy input (MWh $_{Elec.}$ / ton $_{NH_3}$) in evaluating the performance of the N_2 electrolysis system, which is neglected in most electrochemical NRR studies in the literature. The highest production energy efficiency (28.9%) is achieved using Au-Ag-Pd-850 at -0.3 V, which corresponds to the electrical energy input of 19.1 $MWh_{Elec.}$ / ton_{NH_3}. Moving toward more negative potentials, the production energy efficiency decreases to 24.8 % at -0.4V and 8.3% at -0.5V, mainly due to the significant increase in current density at more negative potentials, which increases the electrical energy input (**Figure 5.5C**). It is noted that the increase in the production energy efficiency is in line with the decrease in the electrical energy input for various applied bias. Similar to the electrocatalytic NRR activity results (**Figure 5.5B**), both production energy efficiency and energy input deteriorate for Au-Ag-Pd-750 compared to Au-Ag-Pd-850 in various applied potentials (**Figure 5.5C**). Currently, a significant portion of the input electrical energy (>75%) for all conditions is consumed

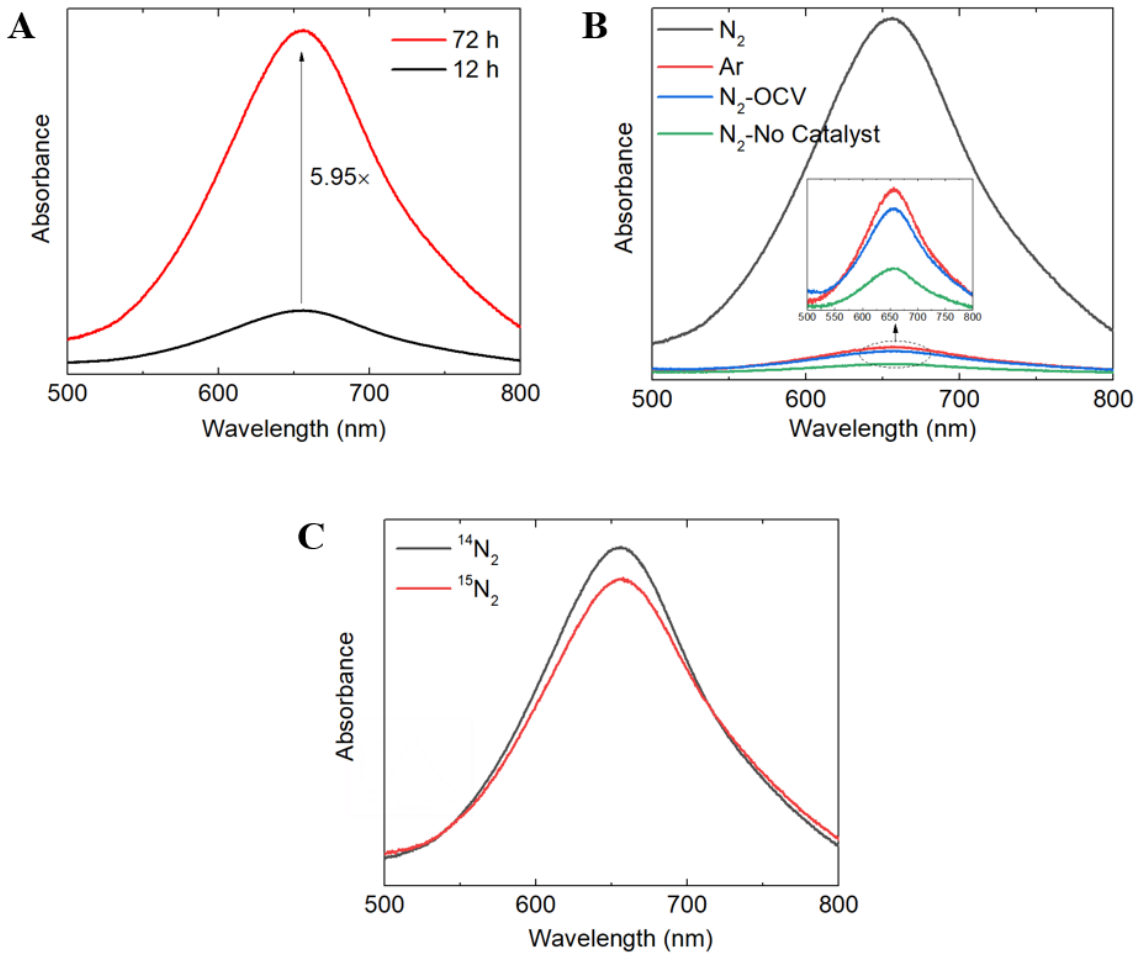

Figure 5.7: A) UV-vis absorption spectra of 0.5 M $LiClO_4$ (aq.) solution after electrolysis at -0.4V vs. RHE for 12 h using Au-Ag-Pd-850 nanoparticles obtained with indophenol blue method in various operating conditions (i.e., N_2, Ar, N_2 at OCV, N_2 with no catalyst). B) UV-vis absorption spectra of 0.5 M $LiClO_4$ (aq.) solution after electrochemical NRR with $^{14}N_2$ and $^{15}N_2$ at -0.4 V vs. RHE for 4 h. C) UV-vis absorption spectrum of 0.5 M $LiClO_4$ (aq.) solution after 72 h stability test at -0.4 V vs. RHE.

at the anode side, where oxygen evolution reaction (OER) takes place. Alternative use of organic-based electrolytes (e.g., glycerol) in the anodic half-reaction could remarkably lower the electricity consumption [97]. It is worth mentioning that the-state-of-the-art thermochemical process (Haber-Bosch) for ammonia synthesis consumes the energy of 7.8 MWh $_{Elec.}$ / ton $_{NH_3}$ (based on natural gas), and the target production energy efficiency of ARPA-E program (REFUEL) for electrochemical fuel production is greater than 60% [34].

A CA test is performed at -0.4V for 72 h to evaluate the stability of Au-Ag-Pd-850

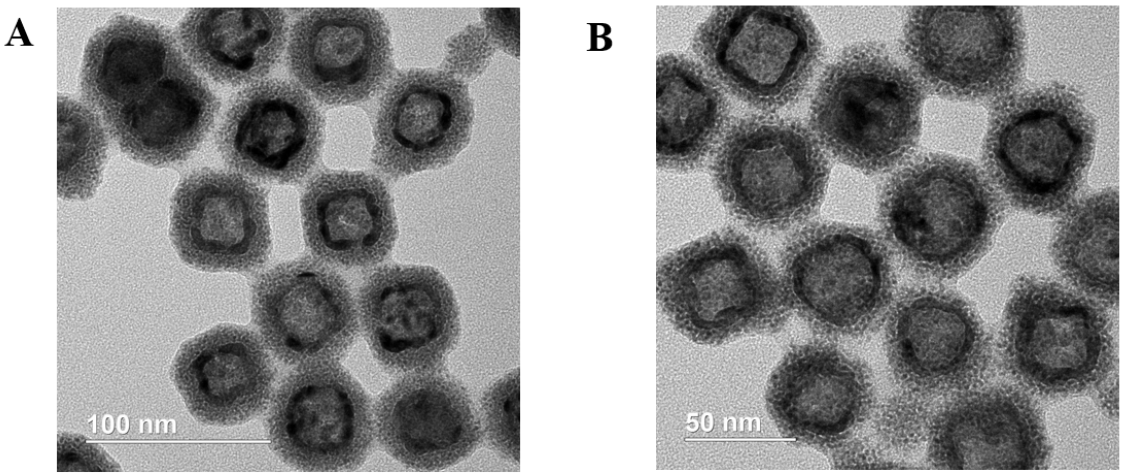

Figure 5.8: A) The TEM images A) before and B) after the electrocatalytic NRR stability test (72 h at -0.4V vs. RHE in 0.5M $LiClO_4$ (aq.) solution).

(**Figure 5.5D**). The electrocatalyst could maintain the NH_3 yield rate (13.62 μg cm^{-2} h^{-1}) and FE (43.5%) over 72 h, which is very close to the NRR activity of the catalyst in the initial 12 h test (**Figure 5.7A**). This performance corresponds to the turnover frequency (TOF) of 59 h^{-1} as per active Pd, Au, and Ag sites. Extensive control experiments are carried out following the instructions in the literature [98, 99, 100]. Control experiments (i.e., Ar, N_2 at OCV, N_2 with no catalyst) with conditions similar to those in **Figure 5.5B**, yield remarkably smaller amounts of NH_3 (Ar:$\sim$7.3% of N_2, N_2 at OCV:$\sim$6.1% of N_2, N_2 with no catalyst:$\sim$2.5% of N_2) (**Figure 5.7B**). The amount of ammonia produced in an isotopic labeling experiment using $^{15}N_2$ gas after a 4 h electrolysis test is close to that of $^{14}N_2$ (73.6 μM, 91% of $^{14}N_2$) (**Figure 5.7C**). Furthermore, the doublet and triplet couplings of $^{15}N_2$ and $^{14}N_2$ obtained from ^{1}H NMR measurement confirms that the supplied N_2 is the major source of ammonia formation in the system (**Figure 5.5E**). The amounts of ammonia measured using ^{1}H NMR are similar to the indophenol method (71.9 μM for $^{15}N_2$ and 78.4 μM for $^{14}N_2$). The TEM images after the stability test show the minor morphology change of nanoparticles after 72 h of the CA test (**Figure 5.8A, B**).

To probe the possible reaction mechanisms and track the intermediate species in elec-

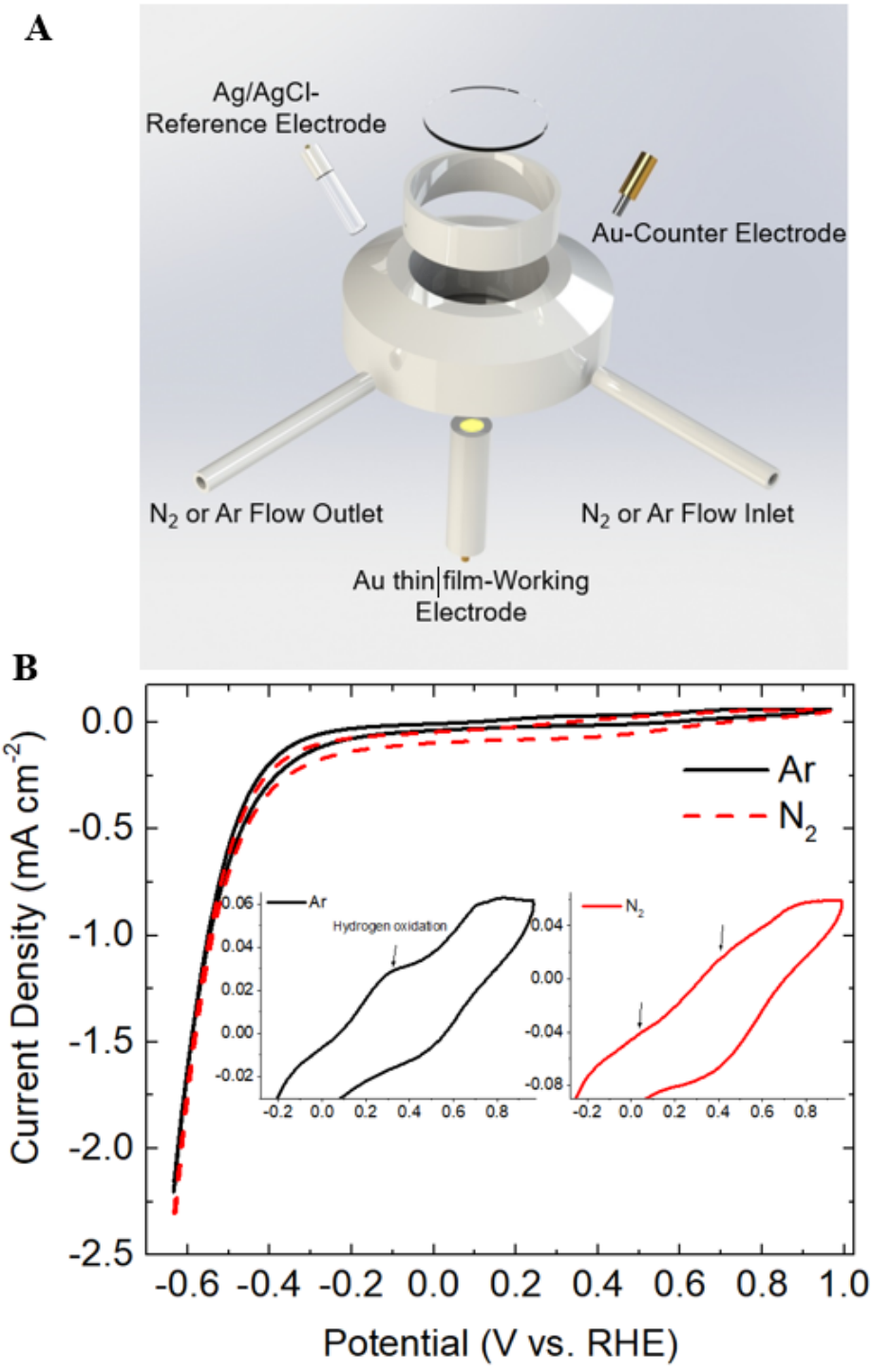

Figure 5.9: A) Schematic of the spectroelectrochemical setup for operando SERS measurements. B) CV curves of Au-Ag-Pd-850 in Ar- and N_2-saturated 0.5M $LiClO_4$ (aq.) solution at the scan rate of 2.5 mV s^{-1}. During the oxidation segment in Ar-saturated electrolyte, a strong peak centered on 0.3 V corresponds to the oxidation of hydrogen. This peak with the lower intensity and slight positive potential shift is also observed in N_2-saturated electrolyte. In addition, a new peak at around 0.05 V is observed in N_2-saturated electrolyte which might be attributed to the oxidation of N-containing species.

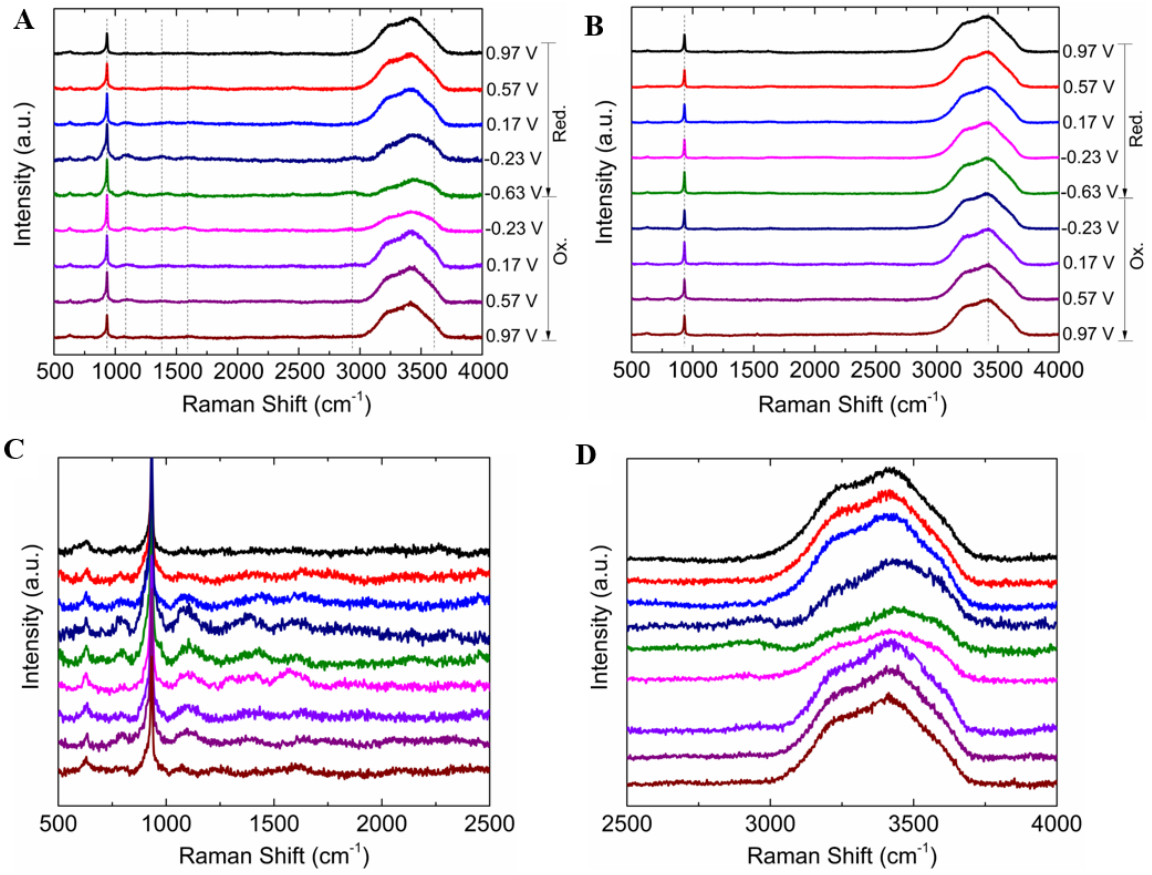

Figure 5.10: A) *Operando* SERS using Au-Ag-Pd-850 nanoparticles in N_2-saturated 0.5M $LiClO_4$ (aq.) solution at the scan rate of 2.5 mV s^{-1} with 532 nm laser. B) *Operando* SERS using Au-Ag-Pd-850 nanoparticles in Ar-saturated 0.5M $LiClO_4$ (aq.) solution at the scan rate of 2.5 mV s^{-1} with 532 nm laser. C) and D) Low and high Raman shift of SERS spectra in N_2-saturated electrolyte (Figure 5.10A).

trocatalytic NRR, *operando* SERS spectra are collected during the CV tests on the SERS active substrate, which is comprised of Au-Ag-Pd nanoparticles deposited on the Au thin film working electrode. The spectro-electrochemical setup and CV curves are shown in **Figures 5.9A, B**.

The SERS spectra in N_2- and Ar-saturated $LiClO_4$ (aq.) solution contain the vibrational band located at 932 cm^{-1}, which is attributed to the stretching mode of the ClO_4^- anion (**Figure 5.10A, B**). In addition, the wide vibrational band centered at 3415 cm^{-1} corresponds to O-H stretching. As the potential is swept to negative values in the reductive pathway (0.97 V to -0.23 V vs RHE), the faint evolution of three vibrational modes at 1094,

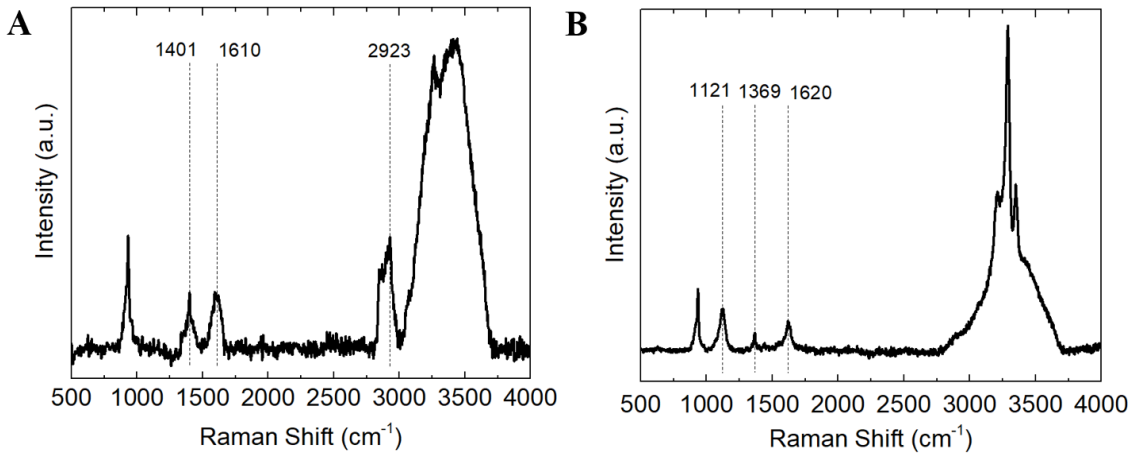

Figure 5.11: A) SERS spectrum of the standard ammonia solution (30 μM NH_4^+) in 0.5M $LiClO_4$ (aq.) solution. B) SERS spectrum of the standard hydrazine solution (60 μM N_2H_4 (aq.)) in 0.5M $LiClO_4$ (aq.) solution.

1393, 1601 cm^{-1} is observed, reaching their highest intensity at -0.23V; these can be classified as N-N stretching, H-N-H bending, and N-H wagging, and these suggest the formation of N_2H_4 as an intermediate species (**Figure 5.10A, C, D**) [53]. Two more peaks centered at 2937 cm^{-1} and 3605 cm^{-1} are evolved at -0.23V, corresponding to the N-H asymmetric and symmetric stretching modes, respectively. The evolution of these two peaks strongly supports the formation of NH_4^+ during the reductive potential sweep [53, 101, 102]. By moving toward more negative potentials during the reductive CV scan (-0.23 v to -0.63 V), the intensity of peaks at 1094, 1393, 1601 cm^{-1} (intermediates) decreases while the peak at 2937 cm^{-1} and the shoulder at 3605 cm^{-1} (NH_4^+) reach their highest intensities. This strongly suggests the formation of NH_3 from the intermediate species ($N_2 \rightarrow N_2H_4 \rightarrow NH_3$) (**Figure 5.10A, C, D**). Since the literature values used to assign these peaks were obtained using infrared (IR) spectroscopy, the wavenumbers are not expected to align precisely, as the excitation mechanisms are different in each type of spectroscopy. The intensity of the peaks ascribed to intermediates and ammonium decreases during the oxidative pathway due to the oxidation of the N-containing species (**Figure 5.10A, C, D**). The SERS spectra of the standard ammonia and hydrazine solutions in 0.5M $LiClO_4$ (aq.) confirm the band assign-

ment of various vibrational modes in NRR operando SERS measurements (**Figure 5.11A, B**). Furthermore, operando SERS measurements in Ar-saturated electrolyte with the electrocatalyst reveal no pronounced peaks, implying the peaks observed in N_2-saturated electrolyte with the electrocatalyst are solely related to the formation of N-containing species at the presence of the electrocatalyst (**Figure 5.10B**).

5.4 Conclusion

In this chapter, the role of incorporation of Pd in bimetallic Au-Ag nanocages on the electrocatalytic NRR selectivity and activity was investigated. TEM, EDX, ICPES measurements, and stoichiometric balance revealed that the reduction of Pd^{2+} to Pd^0 is accomplished through both an island-growth mode on Au as well as the galvanic replacement of Ag. The increase in the Pd content is controlled by monitoring the localized surface plasmon resonance (LSPR) peak position of the resulting trimetallic nanoparticles. The $ECSA_{Pd}$ achieved with our synthesized Au-Ag-Pd-850 nanoparticles is approximately 5 times higher than that of commercial Pd/C catalyst, which is mainly attributed to the formation of a rough and porous layer of Pd in trimetallic nanostructures. The correlation between the position of the d-band center of trimetallic nanoparticles and the Pd content was explored. Furthermore, the effect of Pd content on NRR current density, selectivity, and activity was discussed. The highest electrocatalytic NRR activity (FE=48.94% and NH_3 yield rate=5.80 μg cm^{-2} h^{-1}) was achieved at -0.3V vs. RHE. This corresponds to the production energy efficiency of 28.9% and the electrical energy input of 19.1 $MWh_{Elec.}$ / ton_{NH_3}. *Operando* SERS revealed that electrochemical NRR takes place on the catalyst surface through an associative mechanism with N_2H_4 as an intermediate species. This chapter highlights the importance of engineering the morphology and composition of nanocatalysts to improve the electrocatalytic NRR activity. In particular, it informs the crucial role of Pd with enhanced ECSA for increasing the rate of ammonia electrosynthesis. It also demonstrates the use of *operando* SERS as a powerful technique for unraveling reaction

mechanisms for the electrocatalytic phenomenon.

CHAPTER 6

PLASMON-ENHANCED PHOTOSYNTHESIS OF AMMONIA USING VISIBLE LIGHT RESPONSIVE HYBRID HOLLOW PLASMONIC NANOCAGES

6.1 Introduction

Photocatalytic nitrogen fixation for "green ammonia" synthesis, using water as a reducing reagent and sunlight under ambient conditions, provides an attractive route for clean, sustainable, and distributed ammonia synthesis. This approach might serve as an alternative to the Haber-Bosch process, particularly in remote areas where access to the centralized infrastructure or pipelines is limited [103]. To date, almost all photocatalysts for nitrogen reduction reaction (NRR) suffer from poor selectivity, low activity due to the difficulty in breaking the strong N≡N bond, competition with the more favorable hydrogen evolution reaction (HER), and inefficient utilization of the solar spectrum. Superior light absorption, efficient photo-excited charge separation, and transfer, and the ability to drive photocatalytic redox reactions are the key elements to the rational design of an efficient photocatalyst for the NRR [104]. The photocatalytic redox system using water as a reducing reagent comprises water oxidation at the valence band through the reaction of water with photo-generated holes (h^+) (Equation 6.1) and NRR at the conduction band through the reaction of N_2, protons (H^+), and photo-generated electrons (Equation 6.2) [105]:

$$3H_2O + 6h^+ \rightarrow \frac{3}{2}O_2 + 6H^+ \tag{6.1}$$

$$N_2 + 6H^+ + 6e^- \rightarrow 2NH_3 \tag{6.2}$$

The overall reaction, with the Gibbs free energy (ΔG^o) of 339 kJ mol^{-1} for ammonia formation from water and N_2, is:

$$N_2 + 3H_2O \rightarrow 2NH_3 + \frac{3}{2}O_2 \tag{6.3}$$

To date, most studies on photocatalytic nitrogen fixation have focused on wide bandgap semiconductors (usually metal oxides) such as TiO_2 (E_g=3.2 eV) owing to its abundance, and its high and stable light absorption capability in the UV region. TiO_2 has exhibited moderate NRR activity when incorporated with transition metal dopants (e.g., Fe, Mo, Ru) or through introducing oxygen vacancies at the surface of the photocatalyst [105, 106, 107, 108, 109, 110]. Wide bandgap semiconductors show weak absorption under visible and IR light and therefore, low NRR activity when the wavelength of the incident light is higher than 400 nm. It is important to note that only 5% of the solar irradiation spectrum received on earth's surface is UV (λ<400 nm), while 50% is in the visible region (400nm<λ<800 nm) and the remaining 45% is in the IR region (λ>800 nm). Therefore, the development of a photocatalyst that is active in the incident photon wavelength of greater than 400 nm is necessary to harvest most of the solar irradiation spectrum and enhance the solar-to-ammonia (STA) efficiency (η_{STA}). Recently, it was demonstrated that using oxygen vacancy rich BiOBr nanosheets can enhance the photocatalytic NRR activity under visible light in water, yet there is room to improve the apparent quantum efficiency (η_{AQE}) [111, 112, 113]. Under the stimulus of light, some noble metal nanoparticles, such as Au and Ag, undergo a process called localized surface plasmon resonance (LSPR), which is the collective oscillation of free electrons at the material's surface [104]. The strong electromagnetic plasmon fields generated under light illumination can be utilized for various applications in photocatalysis and sensing [114, 115, 116, 57, 117, 118, 119]. The placement of plasmonic nanostructures in close proximity (<10 nm) to each other results in an enhanced electromagnetic field in the interparticle gap [120].

In this chapter, hybrid Au-Ag_2O nanocages are synthesized through a facile oxidation process, allowing for the coupling of the plasmonic enhancement of Au nanocages with visible-light active p-type Ag_2O to achieve superior photocatalytic NRR performance under ambient conditions using water as an electron donor and sunlight without using sacrificial reagents. While several studies on photocatalytic NRR using hybrid plasmonic-semiconductor photocatalysts have been performed [59, 101, 121, 122], very few have coupled a plasmonic metal and semiconductor that are both active under visible light [118]. Combining the two increases the photo-generated electrons' concentration upon visible light illumination for photocatalytic NRR. In a photochemical system, atmospheric N_2 is converted to NH_3 under ambient conditions using visible light, and water as an electron donor. As the work function of the p-type semiconductor (Ag_2O) is higher than that of the Au plasmonic metal ($\phi_S > \phi_M$), a Schottky barrier is formed where the photo-generated holes of Ag_2O are transferred to the Au plasmonic metal at the metal-semiconductor interface so that the Fermi levels in the metal and semiconductor are aligned [123, 124]. Energy bands in Ag_2O bend downward to match the chemical potentials. Photo-generated electron transfer from the conduction band of Ag_2O to the surface of the Au nanoparticles occurs, or so-called "hot-electrons" are injected from the Au nanoparticle surface to the conduction band of Ag_2O. Both electron transfer processes are possible and competitive. It has been demonstrated that transition metal loaded titania results in smaller ammonia yield than bare titania if Ti^{3+} active sites on the surface are blocked by transition metals, giving experimental proof of these competing phenomenon [107]. In our nanocages, Au and Ag_2O nanoparticles are settled adjacent to each other whereby both can act as an active site in the interior or at the exterior surface of the nanocages for nitrogen adsorption and reduction, enabling us to achieve superior selectivity and efficiency for the NRR.

6.2 Experimental Methods

6.2.1 Photochemical Nitrogen Reduction

The photocatalytic NRR measurements were carried out in a single-compartment cell using various photoelectrodes comprised of indium tin oxide (ITO) supported nanoparticles immersed in N_2-saturated DI water with magnetic stirring under constant N_2 bubbling at the flow rate of 20 mL min^{-1}. Nitrogen (Ar gas for control experiments) gas was bubbled through the cell for 1 h before starting the photochemical measurements to remove dissolved oxygen gas. To prepare the photoelectrode for the photo(electro)chemical tests, 300 μL of nanoparticles of known concentrations (Table S1) and 1.5 μL of Nafion solution (5% wt.) were sonicated and drop casted onto a square of indium tin oxide (ITO) (1cm $\times$ 1cm) and then dried under N_2 atmosphere at 75°C for 1 h. The photoelectrode was then attached to Ni wire with conductive silver paint and isolated from the electrolyte using epoxy. The air mass (AM) 1.5-irradiance of 100 mW cm^{-2} was provided by a 300 W Xe light source. The illumination intensity near the sample surface was calibrated using a standard Si-solar cell and the distance was adjusted to 6 cm to achieve 1 sun illumination. The cell was placed in the water bath to maintain the reaction temperature constant during the experiment to 20°C and reduce thermal effects on the photocatalytic rate. The solar-to-ammonia efficiency (η_{STA}) is calculated according to the equation 6.4:

$$\eta_{STA}\,(\%) = \frac{\Delta G\ for\ ammonia\ generation\ (J\ mol^{-1}) \times ammonia\ generated\ (mol)}{input\ light\ energy\ (J\ s^{-1}) \times reaction\ time\ (s)} \times 100 \tag{6.4}$$

The free energy for NH_3 generation is 339 kJ mol^{-1} and the input light energy is 1000 J s^{-1}.

using Ag_2O-Au-685 for 2 h illumination under 1 sun, the amount of ammonia generated is 61.28 mg m^{-2}. The energy of ammonia produced is calculated by:

$$E_{NH_3} = \frac{61.28\ mg\ m^{-2} \times 0.0001\ m^2}{17000\ mg\ mol^{-1}} \times 339,000\ J\ mol^{-1} = 0.1222\ J \tag{6.5}$$

The total light energy input (one sun) is given by:

$$E_{light} = 1000\ W\ m^{-2} \times 0.0001\ m^2 \times 2 \times 3600 = 720\ J \tag{6.6}$$

Therefore, the η_{STA} is determined by:

$$\eta_{STA}(\%) = \frac{0.1222}{720} \times 100 = 0.017\% \tag{6.7}$$

By using a cutoff filter to provide visible light wavelength (400 nm$<\lambda<$800 nm), the ammonia production rate of 47.8 mg m^{-2} is obtained after 2 h visible light illumination. In addition, the visible light intensity is measured to be 455.2 W m^{-2}. By following the above calculation, the η_{STA} is calculated to be 0.029%.

$$\eta_{STA-Vis} = \frac{\frac{47.8\ mg\ m^{-2} \times 0.0001\ m^2}{17000\ mg\ mol^{-1}} \times 339,000\ J\ mol^{-1}}{455.2\ W\ m^{-2} \times 0.0001\ m^{-2} \times 2 \times 3600} \times 100 = 0.029\% \tag{6.8}$$

The apparent quantum efficiency (QE) of the NH_3 production using 685 nm bandpass filter with 15 nm FWHM is calculated as follows:

$$QE\ (\%) = \frac{NH_3\ generated\ (mol) \times 3}{the\ number\ of\ incident\ photons\ (mol)} \times 100 \tag{6.9}$$

The light intensity is measured to be 14 W m^{-2}, and NH_3 yield is measured after 2 h monochromatic light irradiation at 685 nm. The energy of each photon is determined by the following equation:

$$E = \frac{hc}{\lambda} = \frac{6.626 \times 10^{-34}\ J\ s \times 3 \times 10^8\ m\ s^{-1}}{685 \times 10^{-9}\ m} = 2.902 \times 10^{-19} J/photon \tag{6.10}$$

The local power densities at the distance of 6 cm from the light source under one sun illumination and with the monochromatic light irradiation at 685 nm with 15 nm bandwidth at full width half maximum (FWHM) are 1000 and 14 W m^{-2}, which are determined by the

standard Si-solar cell. The active surface area of the photoelectrode is 1 cm^2. Then, the energy is determined by:

$$E = 14\ W\ m^{-2} \times 0.0001\ m^2 = 0.0014\ J/s \tag{6.11}$$

The number of photons per second is determined by dividing Equation 6.11 by Equation 6.17:

$$The\ number\ of\ photons\ per\ second = \frac{0.0014\ J\ s^{-1}}{2.902 \times 10^{-19}\ J\ photon^{-1}} = 4.8243 \times 10^{15}\ photon/s \tag{6.12}$$

The total number of incident photons under 2 h illumination is given by:

$$N = 4.8243 \times 10^{15}\ photon/s \times 2 \times 3600\ s = 3.4735 \times 10^{19}\ photons \tag{6.13}$$

The number of moles of photons is then calculated by:

$$n = \frac{3.4735 \times 10^{19}}{6.022 \times 10^{23}} = 5.768 \times 10^{-5}\ moles\ of\ photons \tag{6.14}$$

The ammonia yield after 2 h illumination is obtained to be 39.11 mg m^{-2}.

$$moles\ of\ NH_3\ (mol) = \frac{39.11\ mg\ m^{-2} \times 10^{-4}\ m^2}{17000\ mg\ mol^{-1}} = 2.3 \times 10^{-7}\ mol \tag{6.15}$$

$$QE = 2.3 \times 10^{-7}\ mol \times 35.768 \times 10^{-5} \times 100 \simeq 1.2\ \% \tag{6.16}$$

6.2.2 Photoelectrochemical Measurements

All photoelectrochemical measurements were conducted at 20°C lab temperature in 0.5M $LiClO_4$ (aq.) electrolyte in a standard three-electrode system with the various prepared

nanoparticles deposited on the ITO substrate as the working electrode, Pt mesh as the counter electrode, and Ag/AgCl reference electrodes (3M, BASi, USA) using a CHI instrument potentiostat (CHI, 760D).

Transient Photocurrent Response

Before starting the photocurrent measurement, N_2 or Ar gas was purged through the cell into the $LiClO_4$ (aq.) solution to remove the dissolved oxygen gas for 1 h and purging continued during the photocurrent measurement at the open circuit voltage of the cell. A 300 W Xe light source provides the air mass (AM) 1.5-irradiance of 100 mW cm^{-2}.

Electrochemical Impedance Spectroscopy

Electrochemical impedance spectroscopy (EIS) was recorded by applying an alternating voltage of 5 mV amplitude in the frequency range of 10^5 Hz to 10^{-2} Hz with the open circuit voltage in 0.5M $LiClO_4$ (aq.) solution. A Mott-Schottky plot at a frequency of 1000 Hz was measured in 0.5M $LiClO_4$ (aq.) solution under the dark condition.

6.2.3 Determination of Valence Band Energy Level (E_{VBM}) and Band Gap Energy (E_g)

The bandgap energies (Eg) of Ag_2O-Au nanocages and Ag_2O nanocubes are determined based on the Kubelka-Munk theory. The absorption spectra collected by the UV-vis spectrophotometer is multiplied by the energy and raised to the power of the inverse bandgap transition exponent $(\alpha h\nu)^{\frac{1}{p}}$. α is the absorption coefficient, p is the bandgap transition dependent exponent (p=0.5 for Ag_2O) and hν is the energy per photon, calculated according to the following equation:

$$E = \frac{hc}{\lambda} \tag{6.17}$$

where h is the Plank's constant ($\sim$4.135 $\times$ 10^{-15} eV.s), C is the speed of light in vacuum ($\sim 3 \times 10^{17}$ nm s^{-1}), and λ is the wavelength (nm). To calculate the bandgap energy, $(\alpha h\nu)^{\frac{1}{p}}$ is plotted against hν, known as a Tauc plot. The bandgap energy is obtained by drawing an

inflection tangent in the linear region in the Tauc plot and its intersection on the energy axis where the linear portion crosses the x-axis. The position of the valence band maximum (E_{VBM}) is determined by the summation of the valence band offset at low binding energy (E_F-E_{VBM}) and the secondary electron onset, which is referenced to the 21.21 eV helium source energy (work function (ϕ), E_{VAC}-E_F); these are obtained by performing UPS. For example for the case of Ag_2O, E_{VBM} is calculated as follows:

$$(E_{\text{VAC}} - E_{\text{F}}) + (E_{\text{F}} - E_{\text{VBM}}) = (21.21 - 17.04) + (1.9 - 0) = 6.07\ eV \tag{6.18}$$

This energy level is converted to potential vs. RHE, assuming 4.5 eV at 0V vs. RHE

$$E_{\text{VBM}} = 6.07 - 4.5 = 1.57\ V\ vs.\ RHE \tag{6.19}$$

6.3 Results and Discussion

Bimetallic porous Au-Ag nanocages with various LSPR peak positions and pore sizes are prepared by adding $HAuCl_4$ (aq.) solution to the solid silver nanocubes (AgNCs) solution through the galvanic replacement method. By oxygenating the Au-Ag nanocages through purging the solution with pure oxygen gas, Ag is oxidized to silver (I) oxide (Ag_2O) at room temperature, an extremely stable metal oxide semiconductor in ambient conditions. After oxygen treatment of the Au-Ag nanocages, the LSPR peak position slightly redshifts (e.g., 15 nm for Au-Ag-670), suggesting the formation of Ag_2O in the cavity and successful synthesis of Ag_2O-Au nanocages. Ag_2O-Au nanocages with various LSPR peak positions (i.e., 655, 685, and 715 nm) are prepared by increasing the amount of Au^{3+} ions added to the AgNCs template (**Figure 6.1A**). As Ag atoms are etched and replaced by Au atoms, the LSPR peak position redshifts and the pore size at the walls and corners of the nanocages increases (**Figure 6.1B, C, D**). The detailed information regarding the LSPR peak values before and after oxygen treatment of bimetallic Au-Ag nanocages, and the nanocages' Au

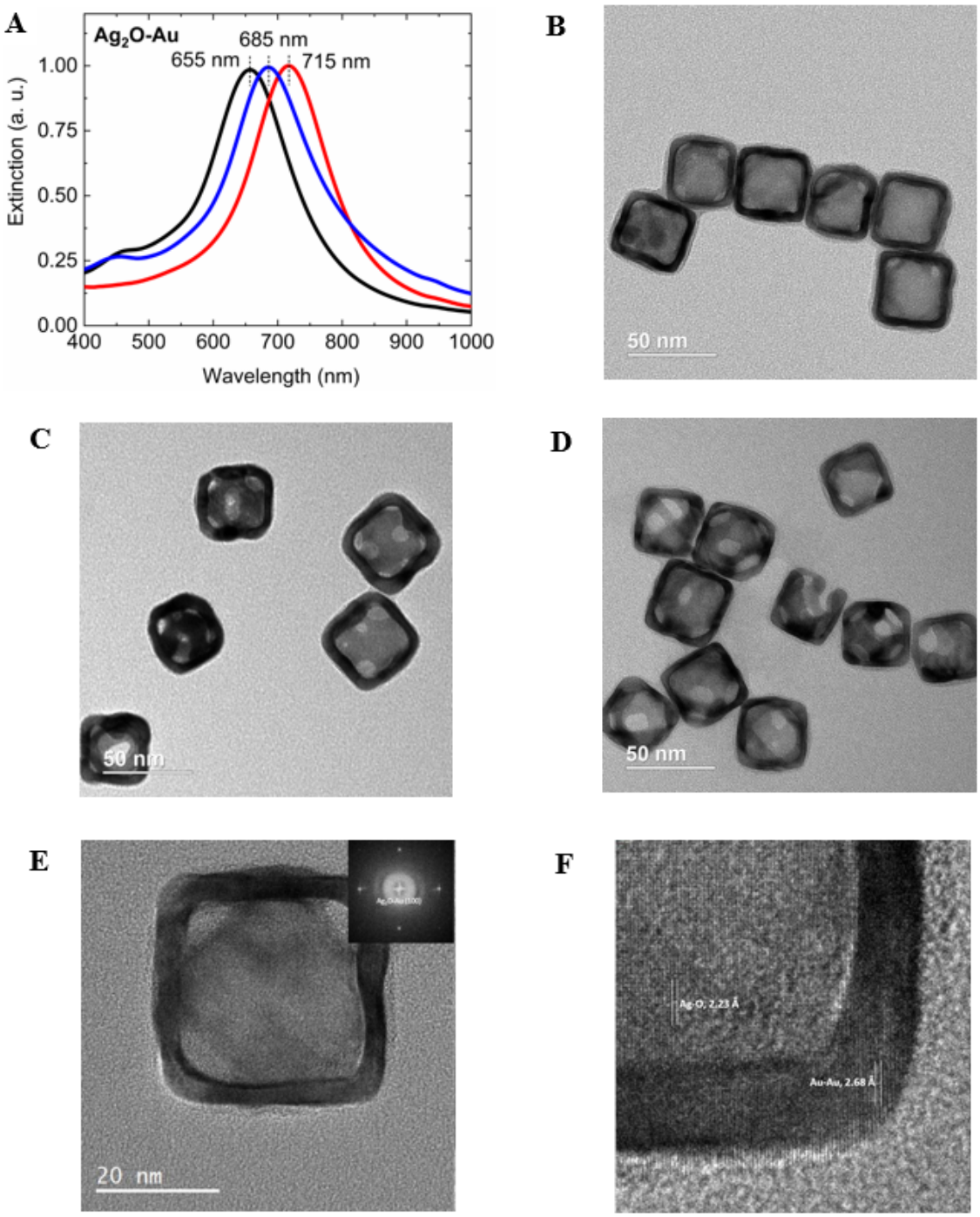

Figure 6.1: UV-vis extinction spectra of Ag_2O-Au nanocages with various LSPR peak values. B), C), and D) are the TEM images of Ag_2O-Au nanocages with LSPR peak values at 655nm, 685 nm, and 715 nm, respectively. As the LSPR peak redshifts from 655 nm to 715 nm, the pore size at the wall and corner of the nanocages increases. E) HR-TEM image of Ag_2O-Au with the LSPR peak value at 685 nm, the inset shows the Fast Fourier Transform (FFT) of the nanoparticle, confirming the formation of Ag_2O after oxygen treatment. F) Lattice spacing of Ag_2O (2.23 Å) and Au (2.68 Å) in the Ag_2O-Au-685 nanoparticle obtained from HRTEM.

Table 6.1: Au, Ag concentrations, Au content (mass % and at. %) of various type of nanoparticles (solid vs. hollow) and their corresponding LSPR peak position and transient photocurrent response.

photocatalyst	Type of nanoparticles	LSPR (nm)	Au Conc. (μg mL^{-1})	Ag Conc. (μg mL^{-1})	Au content (Mass %)	Au Cont. (Atom %)	photocurrent (nA cm^{-2})
Ag-Au	Hollow	645					33.7
			1.4	3.1	31.2	19.9	
Ag_2O-Au	Hollow	655					40.2
Ag-Au	Hollow	670					36.3
			2.0	3.43	37.0	24.2	
Ag_2O-Au	Hollow	685					53.8
Ag-Au	Hollow	710					24.0
			4.45	3.97	47.1	32.8	
Ag_2O-Au	Hollow	715					33.6
Ag_2O	Solid	430	0	0.7	0	0	36.1
Au	Solid NC	535	1.2	0	100	100	11.2
Au	Solid NS	530	0.95	0	100	100	10.1
Au	Solid NR	510, 746	0.5	0	100	100	19.7

and Ag content is provided in Table 6.1. High-resolution transmission electron microscopy (HRTEM) and the Fast Fourier Transform (FFT) of 100 oriented Ag_2O-Au nanocages reveals that Ag_2O has the same orientation as Au (**Figure 6.1E**). Furthermore, the measurement of lattice spacings of Ag_2O (Ag-O atomic spacing, 2.23 Å) and Au (Au-Au atomic spacing, 2.68 Å) in the Ag_2O-Au-685 nanoparticles obtained from HRTEM confirms the formation of Ag_2O after oxygen treatment; these measurements are also comparable with previously reported data obtained by extended x-ray absorption fine structure (EXAFS), (**Figure 6.1F**) [125, 126].

X-ray photoelectron spectroscopy (XPS) measurements are performed to investigate the surface elemental composition and the chemical states of the as-prepared Ag_2O, Ag-Au, and Ag_2O-Au nanoparticles. The XPS survey spectra reveal that Ag_2O-Au and Ag-Au nanocages contain Ag 3d, Au 4f, and O 1s, while Ag 3d and O 1s are observed for Ag_2O (**Figure 6.2A**). A pair of spin-orbit doublets with energy peaks at 84.0 eV and 87.7 eV correspond to Au $4f_{7/2}$ and Au $4f_{5/2}$, indicating the existence of Au^o (Au-Au bonding)

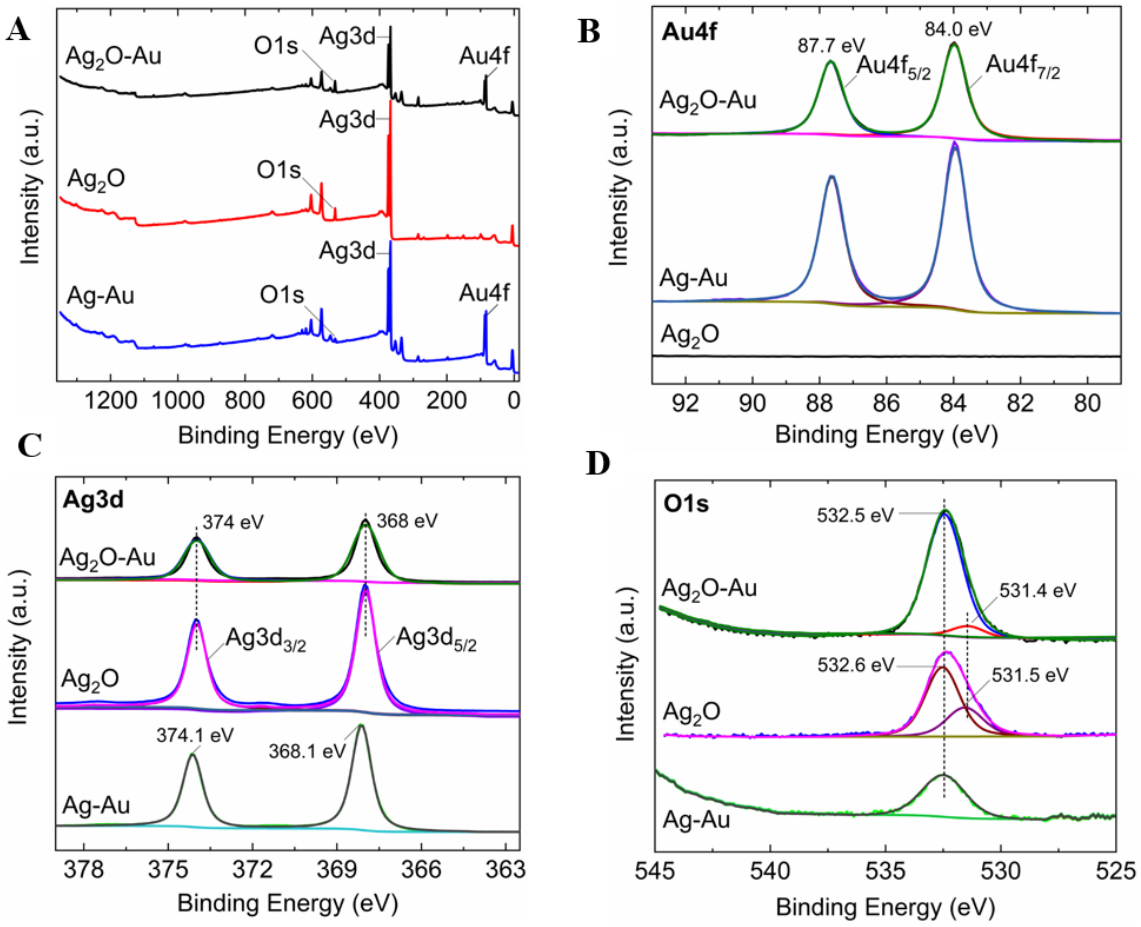

Figure 6.2: A) XPS survey spectra, B) XPS spectra of Au 4f, C) Ag 3d, and D) O1s for Ag_2O, Ag_2O-Au, and Ag-Au nanoparticles. All spectra were shift corrected using a standard reference C1s, C-C peak at 284.8 eV.

in Ag_2O-Au and Ag-Au nanocages, while as expected no Au bonding energy peaks are observed for Ag_2O from the high-resolution XPS spectra of Au 4f (**Figure 6.2B**) [54]. The doublet peaks at 368.0 eV and 374.0 eV are assigned to the Ag $3d_{5/2}$ and Ag $3d_{3/2}$, for Ag_2O-Au and Ag_2O, while a slight shift to high binding energy (0.1 eV) is observed for Ag-Au, which distinguishes between Ag^o (Ag-Ag bonding) and Ag^+ (Ag-O bonding) (**Figure 6.2C**) [73]. The O 1s profiles for Ag_2O and Ag_2O-Au are deconvoluted into two peaks centered at 531.5 eV and 532.6 eV (with 0.1 eV negative shift to lower binding energy for Ag_2O-Au), which are attributed to the lattice oxygen atoms of Ag_2O and the chemisorbed oxygen caused by the external –OH group or the water molecule adsorbed on

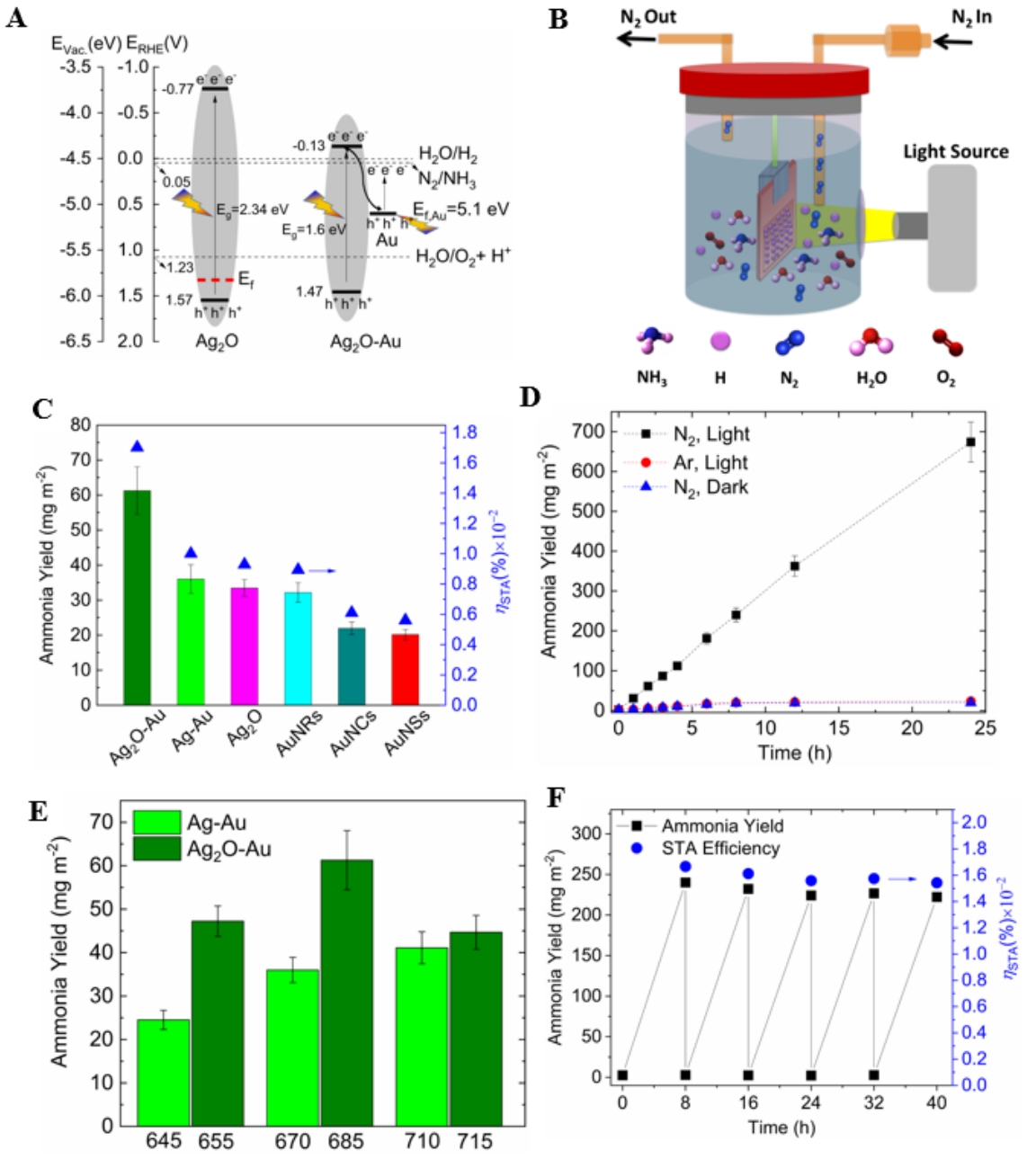

Figure 6.3: A) Electronic band structure of Ag_2O and Ag_2O-Au photocatalysts for nitrogen reduction reaction B) Schematic of photochemical cell for NRR. C) Ammonia yield and solar-to-ammonia (STA) efficiency of various photocatalysts under one sun illumination for 2 h in a N_2 saturated pure water. D) Ammonia yield of Ag_2O-Au-685 under various operating conditions over 24 h. E) Ammonia yield for photocatalysts with various LSPR peak values before (Ag-Au) and after (Ag_2O-Au) oxygen treatment. F) Stability test of Ag_2O-Au-685 photoelectrode for ammonia production. Five consecutive tests are carried out for the period of 8 h (total 40 h) using Ag_2O-Au-685 photoelectrode. The electrolyte solution was replaced before starting each cycle.

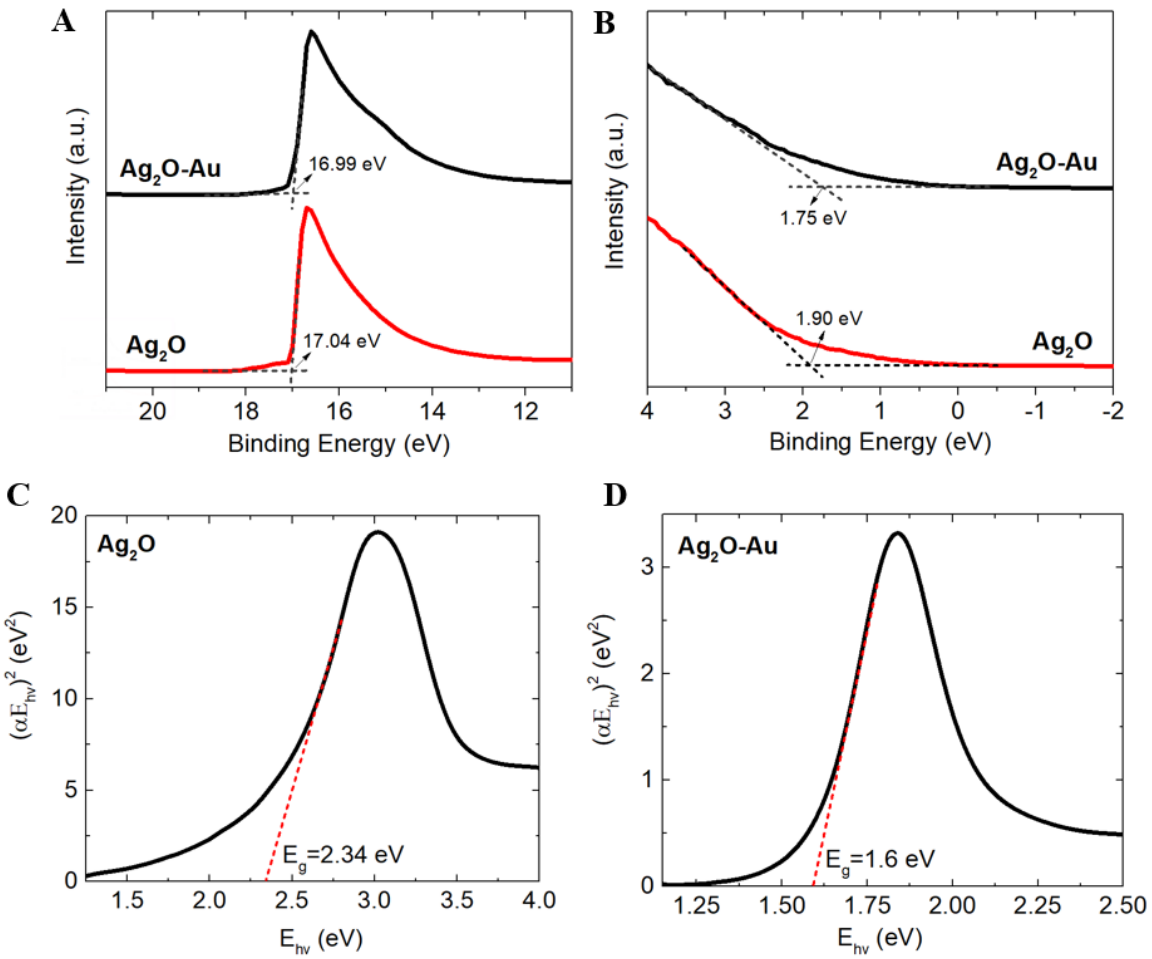

Figure 6.4: UPS spectra of Ag_2O nanocubes and Ag_2O-Au nanocages. The UPS spectra of A) the secondary electron edge and B) the valance bands are measured with He1 (21.22 eV) source radiation. C) and D) Bandgap determination of Ag_2O nanocubes and Ag_2O-Au nanocages using Kubelka-Munk theory.

the surface (**Figure 6.2D**) [73, 74]. The latter peak is also observed in the O 1s profile for Ag-Au nanocages.

The electronic band structures of Ag_2O and Ag_2O-Au-685 nanocages are determined by optical band gaps and ultraviolet photoelectron spectroscopy (UPS) results (**Figure 6.3A**). The summation of the valence band offset at low binding energy (E_F-E_{VBM}) and the secondary electron onset, referenced to the 21.21 eV helium source energy (work function (ϕ), E_{VAC}-E_F), provides the position of the valence band maximum (E_{VBM}) (**Figure 6.4A, B**). The Fermi level of Au has been reported to be 5.1 eV [117]. The optical band gap is calcu-

lated by measuring UV-vis spectra of the photocatalysts. The UV-vis spectra are analyzed by the Kubelka-Munk (KM) theory, where an inflection tangent is drawn in the linear portion of the KM function versus the energy of light absorbed (**Figure 6.4C, D**) [127, 128, 129]. The band gap energies (E_g) of Ag_2O and Ag_2O-Au are calculated to be 2.34 and 1.6 eV, suggesting that both photocatalysts are visible-light responsive. It is important to note that the modified band gap of 1.6 eV corresponds to the hybrid Ag_2O-Au after structural and chemical modifications of AgNCs and Ag-Au nanocages. The E_{VBM} levels of Ag_2O (1.57 V) and Ag_2O-Au (1.47 V) are more positive than 1.23 V vs. RHE, indicating that both photocatalysts can drive water oxidation (**Equation 6.1**) through photo-generated holes, a necessary reaction to provide protons for NRR (**Equation 6.2**). In addition, the energy levels of the conduction band minimum (E_{CBM}) for Ag_2O (-0.77 V) and Ag_2O-Au (-0.13 V) are more negative than the NRR potential (0.05 V vs. RHE), suggesting that direct photocatalytic nitrogen reduction is possible on the surface of photocatalysts without the need for the sacrificial reagent. The E_{VBM} of photocatalysts is not favorable for the nitrogen oxidation reaction (N_2/NO), as nitrogen's oxidation potential is more positive (1.68 V vs. RHE) than the E_{VBM} of photocatalysts. The flat band potential (E_{fb}) of Ag_2O was determined to be 1.31 V vs. RHE, which is close to the E_{VBM} of Ag_2O (1.57 V vs. RHE) as shown in Figure 4.4C. The negative slope of the Mott–Schottky curve confirms that Ag_2O is a p-type semiconductor whose Fermi level energy is lower than that of Au plasmonic metal, indicating the downward bending of the Ag_2O conduction band when it is in contact with Au. Here Au not only provides active catalytic centers for water oxidation and nitrogen reduction through generating hot holes and electrons upon LSPR excitation, but it also collects photo-generated electrons from the Ag_2O semiconductor, retards electron-hole recombination and enhances charge transfer efficiency for NRR.

The photochemical nitrogen fixation tests are carried out in a single-compartment cell using photoelectrodes comprised of indium tin oxide (ITO) supported nanoparticles immersed in N_2-saturated DI water with magnetic stirring under constant N_2 bubbling. The

Table 6.2: The photocatalytic activity of Ag_2O-Au-685 photocatalyst after 2h illumination under full solar spectrum, visible light, and 685 nm bandpass filter with 15 nm FWHM.

Photocatalyst	Ammonia Yield (mg m^{-2})		
	Full solar spectrum	Visible Light ($400<\lambda<800$)	685 nm
Ag_2O-Au-685	61.28±6.8	47.8±4.1	39.11±2.9

external light source shines through a one-inch quartz window placed in the front side of the cell (**Figure 6.3B**). A 300 W Xe light source provides the air mass (AM) 1.5-irradiance of 100 mW cm^{-2}. The illumination intensity near the sample surface is calibrated using a standard Si-solar cell, and the distance is adjusted to 6 cm to achieve one sun illumination. The cell is placed in the water bath to maintain the reaction temperature constant during the experiment to 20°C and reduce thermal effects on the photocatalytic rate. The ammonia yield is measured by using the indophenol blue method.

Among all photoelectrodes tested (i.e., Ag_2O-Au, Ag-Au, Ag_2O, Au), Ag_2O-Au-685 nanocages showed the highest activity, with the ammonia yield of 61.3 mg m^{-2} and η_{STA} of 0.017% after 2 h illumination (**Figure 6.3C**). This high activity is attributed to the combined effects of generated hot electrons by Au nanoparticles and photo-generated electrons by Ag_2O semiconductor that enhanced the photocatalytic NRR activity. The photocatalytic NH_3 production is further investigated by using a cutoff filter to provide visible light irradiation ($400nm<\lambda<800nm$). The NH_3 production rate of 47.8 mg m^{-2} is obtained after 2 h visible light illumination with the visible light intensity of 455.2 W m^{-2}, resulting to a $\eta_{STA\text{-}Vis}$ of 0.029% (see the methods section for the detailed calculation, **Table 6.2**). The Ag-Au nanocages (ammonia yield: 36 mg m^{-2}, η_{STA}: 0.01%) exhibit a higher NRR activity than Ag_2O (ammonia yield: 33.5 mg m^{-2}, η_{STA}: 0.0093%). Although it was shown that Ag is not an active site for NRR, Ag-Au nanocages benefit from the "cage effect" and higher active surface area compared with solid Ag_2O nanocubes, which have higher light absorption capability [130]. It should be noted that among all solid Au plasmonic nanoparticles

(i.e., nanorods (AuNRs), nanocubes (AuNCs), and nanospheres (AuNSs)), AuNRs reveal the highest NRR activity (ammonia yield: 33.5 mg m^{-2}, η_{STA}: 0.0089%). This is attributed to the two plasmon peaks (transverse (510 nm) and longitudinal (746 nm) modes) observed for AuNRs which brings advantage in light absorption compared with one plasmon peak of AuNCs or AuNSs when all other operating conditions are the same (**Figure 6.3C**). In addition, through the oxygen treatment of AgNCs, solid Ag_2O nanocubes are obtained. Even though the current study does not utilize AuNRs, remarkably higher NRR activity is achieved through hybrid nanocages oppose to pure Au nanoparticles. Ag_2O-Au-685 nanocages are further tested throughout 24 h illumination. The ammonia yield rate of 28.2 mg m^{-2} h^{-1} is obtained with N_2 under illumination (N_2, light) (**Figure 6.3D**). Significantly lower ammonia yield rates are achieved in Ar-saturated water with illumination (0.98 mg m^{-2} h^{-1}) and N_2-saturated water without illumination (0.83 mg m^{-2} h^{-1}), indicating that N_2 is the only source of NH_3 obtained by photocatalytic NRR (**Figure 6.3D**). The small amounts of ammonia measured in control experiments could be attributed to the interaction of the adsorbed N_2 at the catalyst surface with water and the leakage of N_2 from the atmosphere into the cell [107, 131]. Ag-Au nanocages with various LSPR peak values (i.e., 645, 670, and 710 nm) and pore sizes are tested for photocatalytic NRR for 2 h illumination before (Ag-Au) and after O_2 treatment (Ag_2O-Au) (**Figure 6.3E**).

For all nanocages, the ammonia yield increases after O_2 treatment of Ag-Au nanocages, suggesting that the formation of Ag_2O enhances the photocatalytic NRR activity for NH_3 production. In addition, among Ag-Au nanocages with various LSPR peak values before O_2 treatment, the ammonia yield increases as LSPR redshifts from 645 nm to 710 nm. This is attributed to the fact that as LSPR redshifts, Ag is replaced with Au through the galvanic replacement, and the Ag content of the nanoparticles decreases (**Table 6.1**). This is favorable for increasing photocatalytic activity, as Au is an active nanocatalyst for NRR. Ag_2O-Au-685 nanocages showed the highest photocatalytic NRR activity. This is ascribed to the compromise between the pore size, the active surface area of the nanoparticle, and the

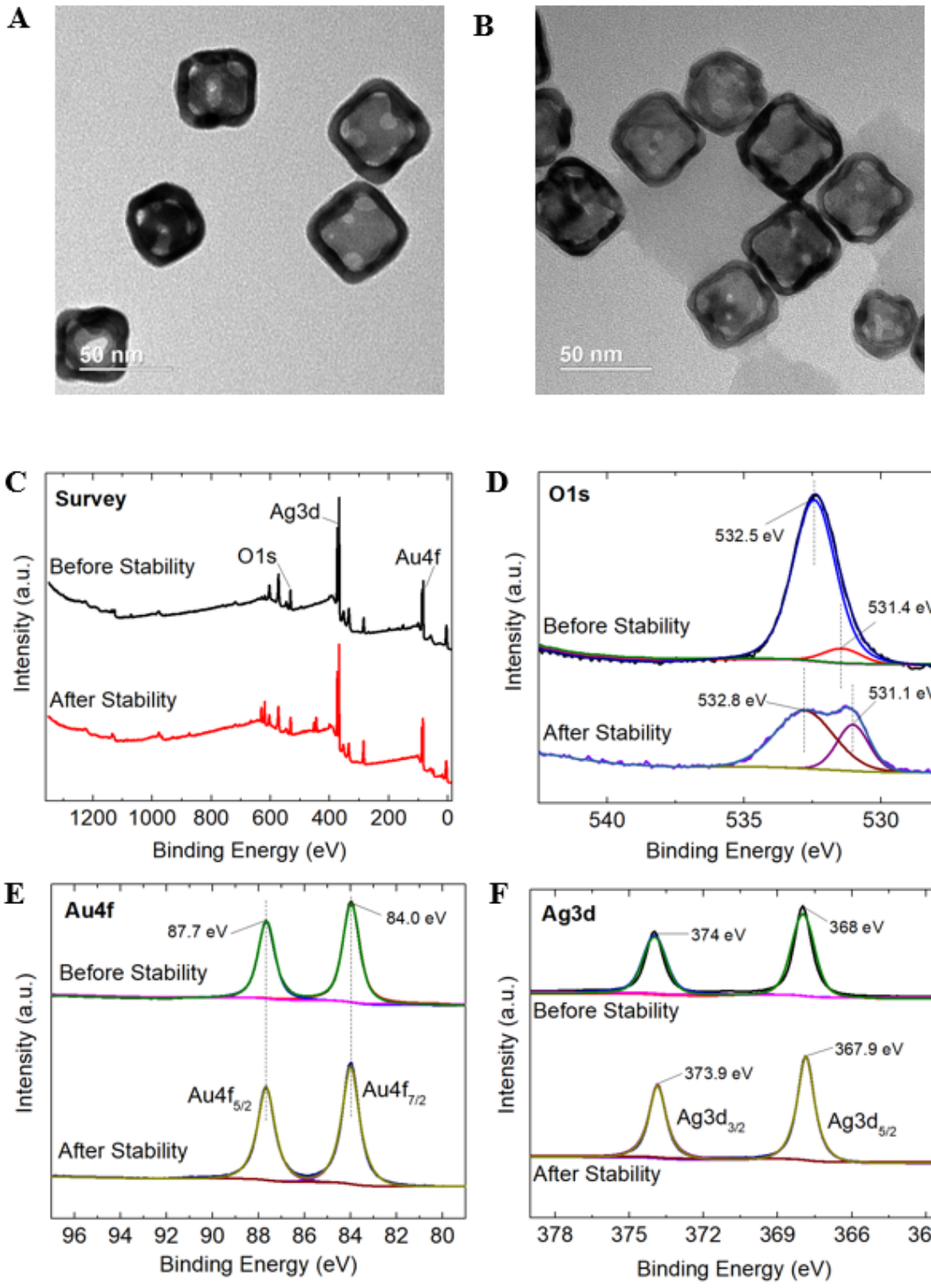

Figure 6.5: TEM images of Ag_2O-Au-685 nanocages A) before and B) after the stability test in the photocatalytic reaction. XPS spectra of Ag_2O-Au-685 photocatalyst before and after the stability test. C) XPS survey spectra, D) XPS spectra of O 1s, E) Au 4f, and F) Ag 3d. All spectra were shift corrected using a standard reference C1s, C-C peak at 284.8 eV.

Ag content (transformed to Ag_2O after O_2 treatment) of Ag_2O-Au nanocages. Here, higher Ag content (Ag_2O-Au-655 has the highest Ag content, See **Table 6.1**) is beneficial, as it is transformed to Ag_2O after O_2 treatment, which provides photo-excited electrons for NRR. In addition, in order to enhance photocatalytic NRR, it is necessary to engineer the optimum pore size; this can be done by tuning the LSPR peak position to obtain the highest active surface area while reactants and products can diffuse in and out of the cavity without restrictions. Here, an optimum Ag content and a pore size that maximizes photocatalytic NRR for NH_3 production are achieved by using Ag_2O-Au-685 nanocages (**Figure 6.3E**). The apparent quantum efficiency (η_{AQE}) is calculated to be 1.2% for Ag_2O-Au-685 nanocages using 685 nm bandpass filter with 15 nm bandwidth at full-width half-maximum (FWHM) which is greater than the highest values currently reported in the literature. The light intensity is measured by a standard Si-solar cell, and the NH_3 yield is measured after 2 h of monochromatic light irradiation at 685 nm (See the methods section for detailed calculations of η_{STA} and η_{AQE}). The stability of Ag_2O-Au-685 for photocatalytic NH_3 production is evaluated for 40 h by conducting five consecutive cycles, each for 8 h (assuming 8 h of daylight per day), (**Figure 6.3F**). The photocatalyst could maintain continuous NH_3 formation with a stable NH_3 yield and η_{STA} (92.5% performance retention). In addition, the TEM images and XPS spectra of the photocatalyst before and after the durability test show that the morphology and chemical states of nanoparticles are reasonably maintained after a 40 h photochemical test (**Figure 6.5**).

The transient photocurrent responses are measured for Ag_2O-Au nanocages with various LSPR peak values supported on the ITO substrate, in N_2-saturated 0.5M $LiClO_4$ (aq.) solution to evaluate the interfacial charge kinetics (**Figure 6.6A**). The schematic of the photoelectrochemical setup is shown in **Figure 6.7**. Ag_2O-Au-685 exhibits the highest photocurrent response, suggesting the efficient charge separation and transfer process using this photocatalyst. This result is in line with the greater photocatalytic activity of NRR for NH_3 production using Ag_2O-Au-685 nanocages. Furthermore, the photocurrent re-

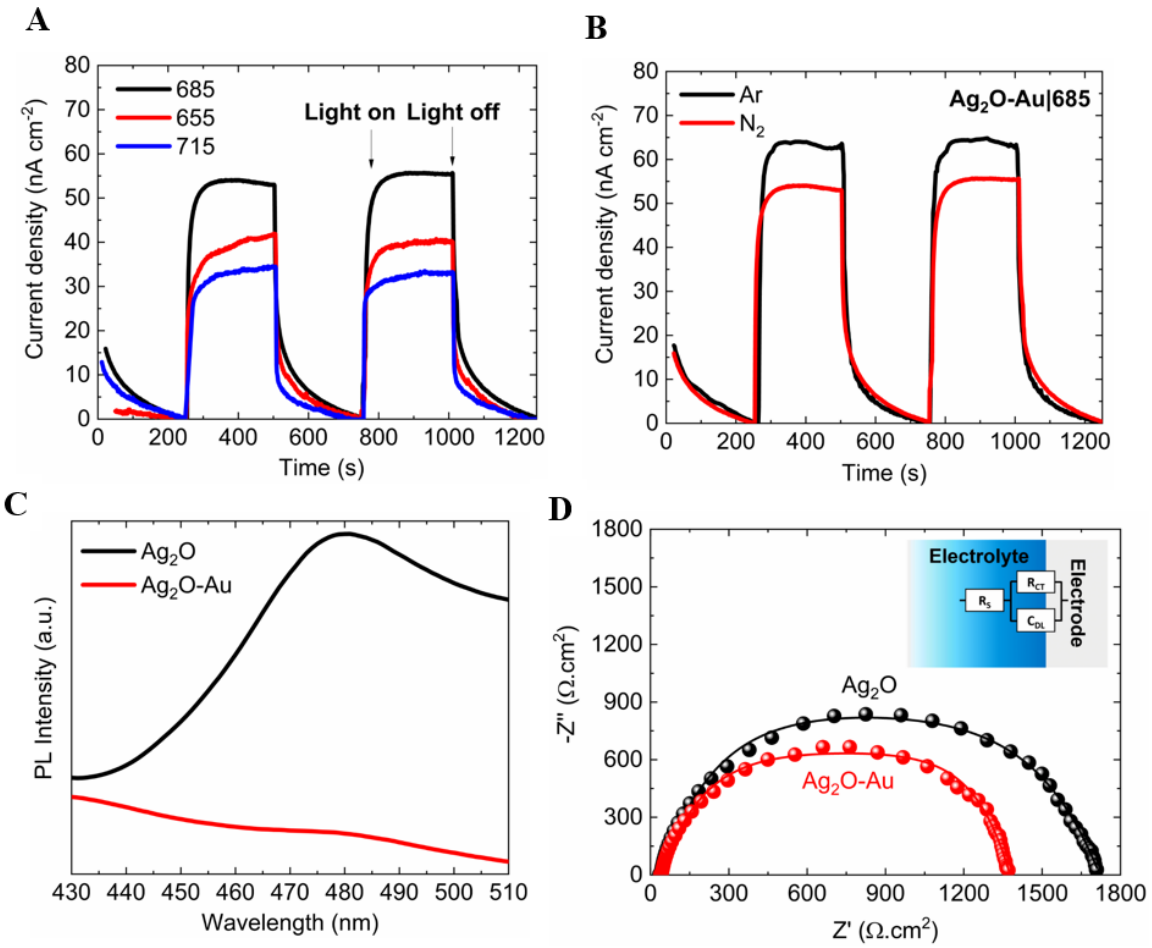

Figure 6.6: Transient photocurrent response of Ag_2O-Au with various LSPR peak values. B) Transient photocurrent response of Ag_2O-Au-685 in N_2 and Ar saturated 0.5M $LiClO_4$ (aq.) solution under 1 sun illumination. Photocurent responses are measured at the open circuit voltage of the cell. C) Photoluminescence spectra of Ag_2O and Ag_2O-Au-685 photocatalysts. Both samples were excited with 375 nm excitation source. D) Nyquist plots of the Ag_2O-Au-685 under photoirradiation at an applied potential of 0.5 V (vs Ag/AgCl) in 0.5M $LiClO_4$ (aq.) solution. The equivalent circuit model in the inset comprises charge transfer resistance (R_{CT}), double layer capacitance (C_{DL}), and ohmic resistance (R_S). R_{CT} was obtained from the diameter of semicircles for each photocatalyst.

sponses are compared in Ar- and N_2-saturated electrolyte using an Ag_2O-Au-685 photoelectrode (**Figure 6.6B**). The higher photocurrent response in Ar-saturated electrolyte (64.3 nA cm^{-2}), compared with N_2-saturated electrolyte (54.1 nA cm^{-2}), is attributed to the two possible pathways for photo-induced electrons in an N_2 atmosphere, where they can either be transferred to the ITO surface (photocurrent response) or to the adsorbed N_2 molecules

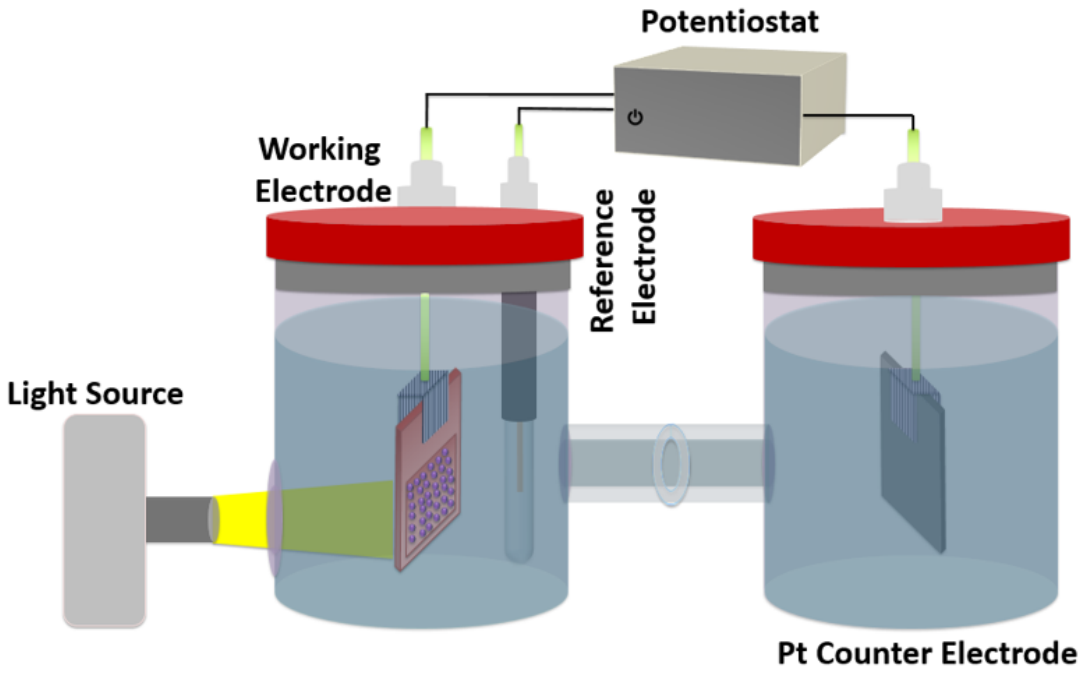

Figure 6.7: The schematic of the photoelectrochemical setup for performing transient photocurrent and EIS measurements. The electrolyte is N_2- or Ar-saturated 0.5M $LiClO_4$ (aq.) solution. Pt counter electrode and Ag/AgCl reference electrode were used for measurements. The light source is 300 W Xe lamp with one sun illumination intensity (100 mW cm^{-2}).

at the electrode-electrolyte interface. This decreases the number of electrons transferred to the ITO and therefore lowers the photocurrent response in an N_2 atmosphere compared with an Ar atmosphere, where only one electron pathway from the photocatalyst to the ITO surface is feasible (**Figure 6.6B**) [128, 132]. The values of the transient photocurrent responses of all nanoparticles are provided in the supporting information (**Table 6.1**). It is important to note that ammonia yield does not change dramatically under visible light illumination (47.8 mg m^{-2}) and on-plasmon resonance excitation at 685 nm (39.11 mg m^{-2}) (**Table 6.2**). The difference between these two values (8.69 mg m^{-2}) is the sole contribution of the Ag_2O semiconductor, which is excited by off-plasmon resonance but has sufficient photon energy to stimulate the Ag_2O. This strongly signifies the plasmonic excitation effect, which is further promoted by charge separation at the plasmonic metal-semiconductor

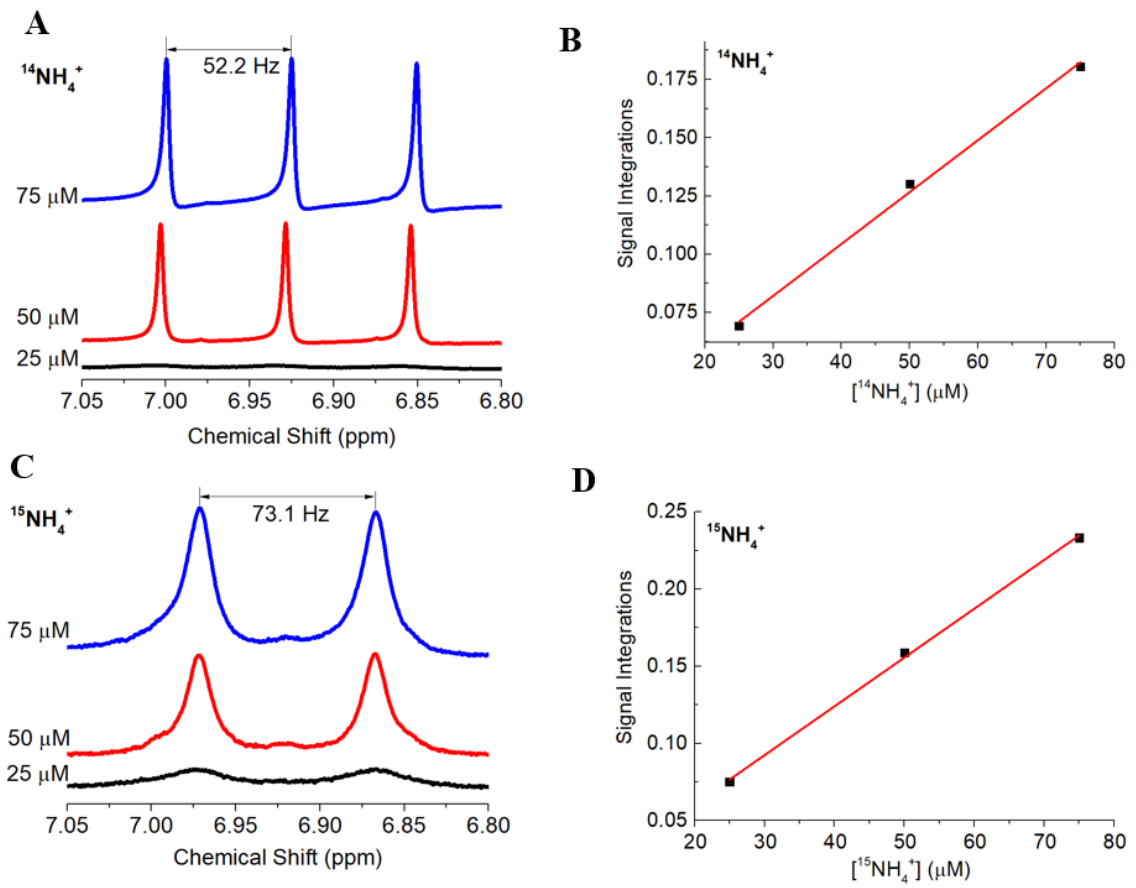

Figure 6.8: A) ^{1}H NMR spectra for the standard $^{14}NH_4^+$ solutions with various concentrations. B) Peak area calibration curve of the ^{1}H NMR signal at 6.93 ppm for standard solutions of $^{14}NH_4^+$ (25, 50, 75 μM). C) ^{1}H NMR spectra for the standard $^{15}NH_4^+$ solutions with various concentrations. D) Peak area calibration curve of the ^{1}H NMR signal at 6.97 ppm for standard solutions of $^{15}NH_4^+$ (25, 50, 75 μM). All peak areas were normalized to the DMSO-d^6 area peak at 2.49 ppm.

interface. Photoluminescence (PL) measurements are performed to examine the charge transfer for Ag_2O and Ag_2O-Au-685 photocatalysts, and emissions are measured using 375 nm excitation wavelength (**Figure 6.6C**). The emission intensity in the PL spectrum of Ag_2O-Au is remarkably lower than that of Ag_2O, which is attributed to the fluorescence quenching by the Au nanoparticles. Furthermore, Nyquist plots are obtained by performing electrochemical impedance spectroscopy (EIS) under illumination (**Figure 6.6D**). The charge transfer resistance (R_{CT}) of Ag_2O-Au (1.34 kΩ.cm^2) is smaller than that of Ag_2O (1.68 kΩ.cm^2), suggesting an enhanced transfer of photo-generated charge carriers, which

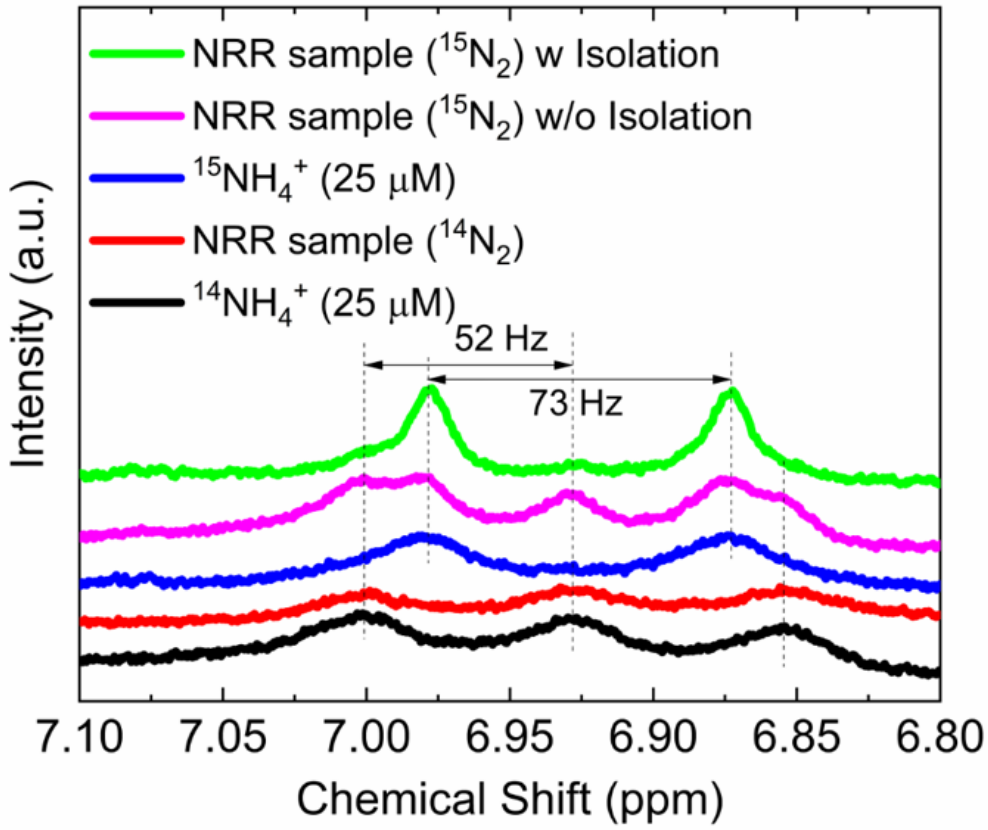

Figure 6.9: ^{1}H NMR spectra of samples after photochemical $^{15}N_2$ ($^{14}N_2$) reduction reaction under 1-sun illumination for 4 h using Ag_2O-Au-685 nanocages and standard $^{15}NH_4^+$ and $^{14}NH_4^+$ samples.

could promote an efficient photocatalytic NRR.

Isotopic labeling experiments using $^{15}N_2$ gas are performed to further confirm the source of NH_3 formation in photochemical NRR tests. The amounts of ammonia produced with $^{14}N_2$ and $^{15}N_2$ after photo-irradiation for 4 h is 16.5 μM and 17.1 μM which were analyzed using the indophenol method. The amount of ammonia is further measured by the NMR method. Calibration curves of the ^{1}H NMR signal for standard solutions of $^{15}NH_4^+$ and $^{14}NH_4^+$ are shown in **Figure 6.8**. ^{1}H NMR spectrum obtained from the sample in the photochemical $^{14}N_2$ reduction experiment lie at a chemical shift of triplet coupling of $^{14}N_2$ similar to that of standard $^{14}NH_4^+$ samples (J-coupling:52 Hz). Doublet coupling of $^{15}N_2$ (J-coupling:73 Hz) is obtained after photochemical $^{15}N_2$ reduction reaction which agrees

well with the standard $^{15}NH_4^+$ solution. A small amount of $^{14}NH_4^+$ is observed ($\sim 4\mu$M) after $^{15}N_2$ reduction experiments, indicating the possible leakage of $^{14}N_2$ from the atmosphere into the cell (**Figure 6.9**). By carefully isolating the cell and maintaining a slight positive pressure of $^{15}N_2$ through connecting the cell's headspace to the gas sampling bag, we successfully decreased the leakage of $^{14}N_2$ (**Figure 6.9**) [131]. The amount of ammonia quantified using ^{1}H NMR measurement is very close to the amount of ammonia measured using indophenol method (16.9 μM for $^{14}NH_4^+$ and 16.6 μM for $^{15}NH_4^+$ using ^{1}H NMR measurements) which further confirms that the supplied N_2 gas is the major source of NH_3 formation in our system.

6.4 Conclusion

Photo(electro)catalytic nitrogen fixation was demonstrated in a pure water system without using sacrificial reagents, under atmospheric pressure and room temperature, and using a visible-light-responsive hybrid hollow plasmonic-semiconductor photocatalyst. At a peak LSPR of 685 nm, a η_{STA} of 0.017% and a η_{AQE} of 1.2% after 2 h monochromatic light irradiation at 685 nm was achieved. The Ag content and pore size were shown to be the key elements for optimizing the photocatalytic activity of NRR using Ag_2O-Au nanocages with various LSPR peak positions. Furthermore, the enhanced activity of Ag_2O-Au compared with Ag-Au is attributed to the contribution of photo-generated electrons after photoexcitation, owing to the formation of Ag_2O after O_2 treatment of Ag-Au nanocages, which were revealed by photochemical testing. The work presented in this chapter opens up a new avenue for the design of an efficient visible-light responsive hybrid hollow plasmonic-semiconductor photoelectrode with broad applications in the photo(electro)chemical energy conversion systems.

CHAPTER 7

FUTURE OUTLOOK

It is essential to compare the input cost in electrochemical NRR (i.e., electricity) method for ammonia synthesis with Industrial Haber-Bosch ammonia production process (i.e., natural gas). This helps to better understand the challenges and opportunities for commercialization of green ammonia synthesis through electrochemical NRR. Detailed cost analysis of these two methods including capital, operation, and maintenance cost is beyond the scope of this chapter. The amount of electricity which is required to produce a ton of ammonia (1000 kg ammonia) is determined according to the following equation:

$$E_{Elec.} = \frac{i \times V \times t \times 2.78 \times 10^{-10}}{NH_3\ yield\ rate \times t \times A} \tag{7.1}$$

where i is the average current denisty during CA test (A), V is the full cell potential in the electrolysis (V), t is the operation time (s), A is the electrode area (cm^2), and 2.78×10^{-10} is the conversion factor from J to MWh. This gives an input renewable electricity required to make a ton of ammonia in the electrochemical system. Through the rational design of electrode-electrolyte with the aim to decrease the amount of electricity consumption in the electrolysis system, further input cost reduction could be achieved. In the Haber-Bosch process, approxiamtely 1000 m^3 (35314.7 ft^3) of natural gas is needed to make one ton of ammonia. With respect to the price volatility of natural gas throughout the year, the input cost of natural gas to make a ton of ammonia is 143 ± 13.8 dollars (US natural gas industrial price is taken from US Energy Information Addministration (EIA) report). This suggests that green ammonia synthesis in the electrochemical cell will be cost competitive with the Haber-Bosch process if we can decrease the renewable electricity price to less than \$30 per MWh or \$0.03 per KWh and if we can have an electrochemical cell with the energy input

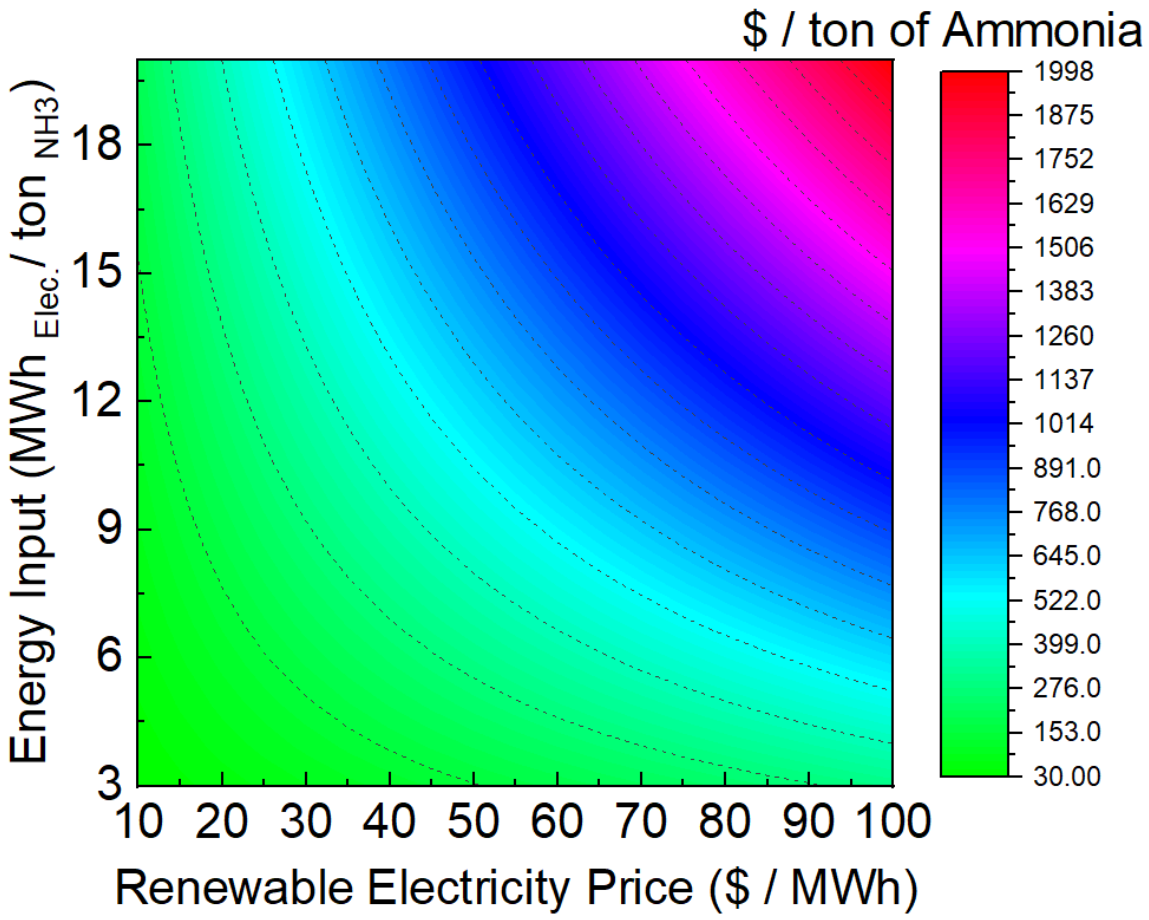

Figure 7.1: Input electricity cost for making one ton of green ammonia as a function of renewable electricity price. The input natural gas cost for making a ton of ammonia in the Haber-Bosch process is relatively constant and is about 150 dollars while for green ammonia there is a substantial room to decrease the renewable electricity price and therefore be cost competitive with the Haber-Bosch process.

< 5 MWh $_{\text{Elec.}}$ / ton $_{NH_3}$ (**Figure 7.1**). This is an optimistic but realistic target to achieve this performance metrics particularly the electricity price from renewable sources such as solar and wind from the current price of about \$0.04-0.05 per kWh.

The US Wind Power market generated \$11.6 B in revenue in 2018, expected to grow to \$19.9 B at a compounded annual growth rate (CAGR) of 11.4% in the next five years to 2023. Likewise, the US Solar Power market generated \$7.5 B in revenue in 2018 and is expected to grow at 13.8% CAGR in the next five years to 2023. In one manner of approximating the market size for energy storage, we can consider Georgia Power's "Nights

& Weekends" concept whereby users pay \$0.2 per kWh during peak load times (2-7 pm weekdays) and pay \$0.05 per kWh at all other times. Since peak load energy commands a $4\times$ price premium, if we conservatively assume that storing renewable energy for sale at peak hours leads to a $3\times$ price premium, our sales available markets would be equal to the size of the targeted renewable markets (consisting of the value-add of that storage). Natural gas energy production was a \$50 B industry in 2018, and since storage and combustion infrastructure can be converted to ammonia, this will not be a limiting factor to our total addressable market. Since wind power is particularly intermittent, we believe this makes a good target market, with a value of \$11.6 B to our customers, if our technology can increase the value of the generated wind power by $3\times$ through storage for peak demand.

Appendices

APPENDIX A

CHEMICALS AND MATERIALS

Silver nitrate ($AgNO_3$), poly(vinylpyrrolidone) (PVP, MW ~55,000 and 10,000), ethylene glycol (EG), sodium sulfide nonahydrate ($Na_2S.9H_2O$), potassium chloride (KCl), sodium borohydride ($NaBH_4$), ascorbic acid, hexadecyltrimethylammonium bromide (CTAB), potassium sodium tartrate solution ($C_4H_4KNaO_6$, 1.5M in H_2O), salicylic acid (ACS reagent, $\geq$99.0%, $C_7H_6O_3$), sodium citrate dihydrate ($\geq$99.0%, $C_6H_5Na_3O_7{\cdot}2H_2O$), potassium tetrachloropalladate (II) (99.99%, K_2PdCl_4), sodium hydroxide (97%, NaOH), sodium nitroprusside dihydrate (ACS reagent, $\geq$99.0%, $C_5FeN_6Na_2O{\cdot}2H_2O$), sodium hypochlorite solution (reagent grade, available chlorine 10-15%, NaClO), nafion solution (5% wt.), ammonium-^{15}N chloride ($^{15}NH_4Cl$, $\geq$98 atom % ^{15}N, $\geq$99% (CP)), and $^{15}N_2$ (98 atom % ^{15}N, 5L) were purchased from Sigma-Aldrich. The $^{15}N_2$ gas was purified before its use in the experiment by passing through the absorber (1mM H_2SO_4) followed by DI water to remove any NO_x and NH_3 contamination in the $^{15}N_2$. Ammonia standard solution (1 mg L^{-1}) and Nessler reagent ($K_2[HgI_4]$) was purchased from Hach Co. Hydrogen tetrachloroaurate (III) trihydrate (ACS, 99.99% (metals basis), Au 49.0% min, $HAuCl_4.3H_2O$) was purchased from Alfa Aesar. Indium tin oxide (ITO) coated one surface (4-8 Ω, Delta Technologies, USA), Ar (UHP, 100%, Airgas, USA), N_2 (UHP, 100%, Airgas, USA), O_2 (UHP, 100%, Airgas, USA), Platinum (100 mesh, 99.9% trace metal basis, Sigma-Aldrich, USA), Ni wire (0.5 mm, $\geq$99.9% trace metals basis, Sigma-Aldrich), and conductive silver paint (Ted Pella Inc.) were used for experiments.

APPENDIX B

INSTRUMENTATION

TEM imaging was performed using a Hitachi HT7700 TEM with the acceleration voltage of 120 kV. An FEI Tecnai F30 super-twin field-emission-gun transmission electron microscope operating at 300 kV was used to acquire the high-resolution TEM (HRTEM) images. HRTEM images were recorded by a Gatan One-View camera. The exposure time of each HRTEM image was 0.04 s. UV-vis spectroscopy was carried out using an Ocean optics spectrophotometer (HR4000Cg-UV-NIR) with 1 cm path length cuvettes in the wavelength range of 200-1000 nm. The SERS spectra of nanoparticles were collected with 1200 lines per mm grating using a Renishaw InVia Raman spectrometer. The sample was focused by a 50$\times$ (0.75 N. A.) objective, and the back-scattered signals were collected at an integration time of the 20 s. The XPS measurements were performed using a Thermo K-Alpha XPS instrument equipped with a monochromated Al Kα radiation source with a 400-μm diameter spot size and 15 W X-ray gun power. The base pressure of the chamber was 2×10^{-8} mbar, and the pressure of the chamber is maintained around 2.5×10^{-7} mbar during the experiment. The analyzer pass energy was set to 50 eV with the energy step size of 0.1 eV and a dwell time of 50 ms. The sample was flooded with a mix of low-energy electrons and an Ar-ion gun using the flood gun for charge compensation. The surface atoms of the sample were sputtered away with Ar^+ ion gun with an energy of 500 eV for 20 s using a sputter gun, and the residual surface was analysed. All spectra were shift corrected using a standard reference C1s, C-C peak at 284.8 eV. The UPS spectra were collected by UPS (Axis UltraDLD, Kratos Analytical) instrument using He I radiation (energy = 21.21 eV). The steady-state photoluminescence was carried out using a photon technology international setup with 375 nm excitation wavelength. The ammonia produced in photochemical experiments was quantified by conducting a ^{1}H-NMR measurement on a Bruker NMR700.

The ^{1}H-NMR signal of ^{14}N produces a triplet (J-coupling constant=52.2 Hz) at the chemical shift of $\sim$7 ppm while ^{15}N is split into a doublet near 7 ppm (J-coupling constant=73.1 Hz). $^{14}NH_4$ is quantified from its signal at 6.93 ppm and a calibration curve is obtained by the integration of this signal (6.93 ppm) as a function of concentration using $^{14}NH_4$ standard solutions made up from $^{14}NH_4Br$. $^{15}NH_4$ is quantified from its signal at 6.97 ppm and a calibration curve is obtained by the integration of this signal (6.97 ppm) as a function of concentration using $^{14}NH_4^+$ standard solutions made up from $^{15}NH_4Cl$. 500 μL of sample is mixed thoroughly with 100 μL of DMSO-d^6 (VWR, USA) as a locking reagent. All experiments were carried out with water suppression and 1000 scans. All peak areas were normalized to the DMSO-d^6 area peak at 2.49 ppm.

REFERENCES

[1] L. N. Lewis and N. Lewis, "Platinum-catalyzed hydrosilylation-colloid formation as the essential step," *Journal of the American Chemical Society*, vol. 108, no. 23, pp. 7228–7231, 1986.

[2] P. L. Freund and M. Spiro, "Colloidal catalysis: The effect of sol size and concentration," *The Journal of Physical Chemistry*, vol. 89, no. 7, pp. 1074–1077, 1985.

[3] R. Rioux, H. Song, J. Hoefelmeyer, P Yang, and G. Somorjai, "High-surface-area catalyst design: Synthesis, characterization, and reaction studies of platinum nanoparticles in mesoporous sba-15 silica," *The Journal of Physical Chemistry B*, vol. 109, no. 6, pp. 2192–2202, 2005.

[4] T. S. Ahmadi, Z. L. Wang, T. C. Green, A. Henglein, and M. A. El-Sayed, "Shape-controlled synthesis of colloidal platinum nanoparticles," *Science*, vol. 272, no. 5270, pp. 1924–1925, 1996.

[5] Y. Sun and Y. Xia, "Shape-controlled synthesis of gold and silver nanoparticles," *science*, vol. 298, no. 5601, pp. 2176–2179, 2002.

[6] C. Burda, X. Chen, R. Narayanan, and M. A. El-Sayed, "Chemistry and properties of nanocrystals of different shapes," *Chemical reviews*, vol. 105, no. 4, pp. 1025–1102, 2005.

[7] R. Narayanan and M. A. El-Sayed, "Shape-dependent catalytic activity of platinum nanoparticles in colloidal solution," *Nano letters*, vol. 4, no. 7, pp. 1343–1348, 2004.

[8] S Abbet, A. M. Ferrari, L Giordano, G Pacchioni, H Hakkinen, U Landman, and U Heiz, "Pd1/mgo (100): A model system in nanocatalysis," *Surface science*, vol. 514, no. 1-3, pp. 249–255, 2002.

[9] R. Narayanan and M. A. El-Sayed, "Carbon-supported spherical palladium nanoparticles as potential recyclable catalysts for the suzuki reaction," *Journal of Catalysis*, vol. 234, no. 2, pp. 348–355, 2005.

[10] R. Narayanan, C. Tabor, and M. A. El-Sayed, "Can the observed changes in the size or shape of a colloidal nanocatalyst reveal the nanocatalysis mechanism type: Homogeneous or heterogeneous?" *Topics in Catalysis*, vol. 48, no. 1-4, p. 60, 2008.

[11] R. Narayanan and M. A. El-Sayed, "FTIR study of the mode of binding of the reactants on the pd nanoparticle surface during the catalysis of the suzuki reaction," *The Journal of Physical Chemistry B*, vol. 109, no. 10, pp. 4357–4360, 2005.

[12] R. Narayana and M. A. El-Sayed, "Changing catalytic activity during colloidal platinum nanocatalysis due to shape changes: Electron-transfer reaction," *Journal of the American Chemical Society*, vol. 126, no. 23, pp. 7194–7195, 2004.

[13] M. A. Mahmoud, R. Narayanan, and M. A. El-Sayed, "Enhancing colloidal metallic nanocatalysis: Sharp edges and corners for solid nanoparticles and cage effect for hollow ones," *Accounts of chemical research*, vol. 46, no. 8, pp. 1795–1805, 2013.

[14] M. Mahmoud, F Saira, and M. El-Sayed, "Experimental evidence for the nanocage effect in catalysis with hollow nanoparticles," *Nano letters*, vol. 10, no. 9, pp. 3764–3769, 2010.

[15] M. Mahmoud and M. El-Sayed, "Time dependence and signs of the shift of the surface plasmon resonance frequency in nanocages elucidate the nanocatalysis mechanism in hollow nanoparticles," *Nano letters*, vol. 11, no. 3, pp. 946–953, 2011.

[16] M. A. Mahmoud, "Surface-enhanced raman spectroscopy of double-shell hollow nanoparticles: Electromagnetic and chemical enhancements," *Langmuir*, vol. 29, no. 21, pp. 6253–6261, 2013.

[17] Y. Sun, B. Mayers, and Y. Xia, "Metal nanostructures with hollow interiors," *Advanced Materials*, vol. 15, no. 7-8, pp. 641–646, 2003.

[18] C. Chen, Y. Kang, Z. Huo, Z. Zhu, W. Huang, H. L. Xin, J. D. Snyder, D. Li, J. A. Herron, M. Mavrikakis, *et al.*, "Highly crystalline multimetallic nanoframes with three-dimensional electrocatalytic surfaces," *Science*, vol. 343, no. 6177, pp. 1339–1343, 2014.

[19] J. Zeng, Q. Zhang, J. Chen, and Y. Xia, "A comparison study of the catalytic properties of au-based nanocages, nanoboxes, and nanoparticles," *Nano letters*, vol. 10, no. 1, pp. 30–35, 2010.

[20] G. Weng, M. A. Mahmoud, and M. A. El-Sayed, "Nanocatalysts can change the number of electrons involved in oxidation–reduction reaction with the nanocages being the most efficient," *The Journal of Physical Chemistry C*, vol. 116, no. 45, pp. 24 171–24 176, 2012.

[21] C. Yen, M. Mahmoud, and M. El-Sayed, "Photocatalysis in gold nanocage nanoreactors," *The Journal of Physical Chemistry A*, vol. 113, no. 16, pp. 4340–4345, 2009.

[22] M. Yadav, T. Akita, N. Tsumori, and Q. Xu, "Strong metal–molecular support interaction (smmsi): Amine-functionalized gold nanoparticles encapsulated in silica nanospheres highly active for catalytic decomposition of formic acid," *Journal of Materials Chemistry*, vol. 22, no. 25, pp. 12 582–12 586, 2012.

[23] M. Eddaoudi, J. Kim, N. Rosi, D. Vodak, J. Wachter, M. O'Keeffe, and O. M. Yaghi, "Systematic design of pore size and functionality in isoreticular mofs and their application in methane storage," *Science*, vol. 295, no. 5554, pp. 469–472, 2002.

[24] M. Graeser, E. Pippel, A. Greiner, and J. H. Wendorff, "Polymer core- shell fibers with metal nanoparticles as nanoreactor for catalysis," *Macromolecules*, vol. 40, no. 17, pp. 6032–6039, 2007.

[25] J. C. Park, J. U. Bang, J. Lee, C. H. Ko, and H. Song, "Ni@ sio 2 yolk-shell nanoreactor catalysts: High temperature stability and recyclability," *Journal of Materials Chemistry*, vol. 20, no. 7, pp. 1239–1246, 2010.

[26] J. E. Macdonald, M. B. Sadan, L. Houben, I. Popov, and U. Banin, "Hybrid nanoscale inorganic cages," *Nature materials*, vol. 9, no. 10, pp. 810–815, 2010.

[27] L. Rodriguez-Lorenzo, R. A. Alvarez-Puebla, I. Pastoriza-Santos, S. Mazzucco, O. Stephan, M. Kociak, L. M. Liz-Marzan, and F. J. Garcia de Abajo, "Zeptomol detection through controlled ultrasensitive surface-enhanced raman scattering," *Journal of the American Chemical Society*, vol. 131, no. 13, pp. 4616–4618, 2009.

[28] J. F. Li, Y. F. Huang, Y. Ding, Z. L. Yang, S. B. Li, X. S. Zhou, F. R. Fan, W. Zhang, Z. Y. Zhou, B. Ren, *et al.*, "Shell-isolated nanoparticle-enhanced raman spectroscopy," *nature*, vol. 464, no. 7287, pp. 392–395, 2010.

[29] K. N. Heck, B. G. Janesko, G. E. Scuseria, N. J. Halas, and M. S. Wong, "Using catalytic and surface-enhanced raman spectroscopy-active gold nanoshells to understand the role of basicity in glycerol oxidation," *ACS Catalysis*, vol. 3, no. 11, pp. 2430–2435, 2013.

[30] V. Smil, *Enriching the earth: Fritz Haber, Carl Bosch, and the transformation of world food production*. MIT press, 2004.

[31] J. A. Ober, "Mineral commodity summaries 2016," US Geological Survey, Tech. Rep., 2016.

[32] V. Smil, "Detonator of the population explosion," *Nature*, vol. 400, no. 6743, pp. 415–415, 1999.

[33] R. Lan and S. Tao, "Ammonia as a suitable fuel for fuel cells," *Frontiers in energy research*, vol. 2, p. 35, 2014.

[34] S Giddey, S. Badwal, C Munnings, and M Dolan, "Ammonia as a renewable energy transportation media," *ACS Sustainable Chemistry & Engineering*, vol. 5, no. 11, pp. 10 231–10 239, 2017.

[35] T. Hua, R. Ahluwalia, J.-K. Peng, M. Kromer, S. Lasher, K. McKenney, K. Law, and J. Sinha, "Technical assessment of compressed hydrogen storage tank systems for automotive applications," *International Journal of Hydrogen Energy*, vol. 36, no. 4, pp. 3037–3049, 2011.

[36] R. Strait and M. Nagvekar, "Carbon dioxide capture and storage in the nitrogen and syngas industries," *Nitrogen+ Syngas*, vol. 303, pp. 1–3, 2010.

[37] G. Soloveichik, "Electrochemical synthesis of ammonia as a potential alternative to the haber–bosch process," *Nature Catalysis*, vol. 2, no. 5, pp. 377–380, 2019.

[38] T. Spatzal, M. Aksoyoglu, L. Zhang, S. L. Andrade, E. Schleicher, S. Weber, D. C. Rees, and O. Einsle, "Evidence for interstitial carbon in nitrogenase femo cofactor," *Science*, vol. 334, no. 6058, pp. 940–940, 2011.

[39] C Zamfirescu and I Dincer, "Using ammonia as a sustainable fuel," *Journal of Power Sources*, vol. 185, no. 1, pp. 459–465, 2008.

[40] A. Klerke, C. H. Christensen, J. K. Nørskov, and T. Vegge, "Ammonia for hydrogen storage: Challenges and opportunities," *Journal of Materials Chemistry*, vol. 18, no. 20, pp. 2304–2310, 2008.

[41] R. Lan, J. T. Irvine, and S. Tao, "Synthesis of ammonia directly from air and water at ambient temperature and pressure," *Scientific reports*, vol. 3, no. 1, pp. 1–7, 2013.

[42] S. Chen, S. Perathoner, C. Ampelli, C. Mebrahtu, D. Su, and G. Centi, "Electrocatalytic synthesis of ammonia at room temperature and atmospheric pressure from water and nitrogen on a carbon-nanotube-based electrocatalyst," *Angewandte Chemie International Edition*, vol. 56, no. 10, pp. 2699–2703, 2017.

[43] G.-F. Chen, X. Cao, S. Wu, X. Zeng, L.-X. Ding, M. Zhu, and H. Wang, "Ammonia electrosynthesis with high selectivity under ambient conditions via a li+ incorporation strategy," *Journal of the American Chemical Society*, vol. 139, no. 29, pp. 9771–9774, 2017.

[44] Y. Liu, Y. Su, X. Quan, X. Fan, S. Chen, H. Yu, H. Zhao, Y. Zhang, and J. Zhao, "Facile ammonia synthesis from electrocatalytic n2 reduction under ambient con-

ditions on n-doped porous carbon," *ACS Catalysis*, vol. 8, no. 2, pp. 1186–1191, 2018.

[45] L. Hu, A. Khaniya, J. Wang, G. Chen, W. E. Kaden, and X. Feng, "Ambient electrochemical ammonia synthesis with high selectivity on fe/fe oxide catalyst," *ACS Catalysis*, vol. 8, no. 10, pp. 9312–9319, 2018.

[46] S. Licht, B. Cui, B. Wang, F.-F. Li, J. Lau, and S. Liu, "Ammonia synthesis by n2 and steam electrolysis in molten hydroxide suspensions of nanoscale fe2o3," *Science*, vol. 345, no. 6197, pp. 637–640, 2014.

[47] J. M. McEnaney, A. R. Singh, J. A. Schwalbe, J. Kibsgaard, J. C. Lin, M. Cargnello, T. F. Jaramillo, and J. K. Nørskov, "Ammonia synthesis from n 2 and h 2 o using a lithium cycling electrification strategy at atmospheric pressure," *Energy & Environmental Science*, vol. 10, no. 7, pp. 1621–1630, 2017.

[48] A. R. Singh, B. A. Rohr, J. A. Schwalbe, M. Cargnello, K. Chan, T. F. Jaramillo, I. Chorkendorff, and J. K. Nørskov, *Electrochemical ammonia synthesis-the selectivity challenge*, 2017.

[49] J. H. Montoya, C. Tsai, A. Vojvodic, and J. K. Nørskov, "The challenge of electrochemical ammonia synthesis: A new perspective on the role of nitrogen scaling relations," *ChemSusChem*, vol. 8, no. 13, pp. 2180–2186, 2015.

[50] G. Qing and T. W. Hamann, "New electrolytic devices produce ammonia with exceptional selectivity," *Joule*, vol. 3, no. 3, pp. 634–636, 2019.

[51] R. Hawtof, S. Ghosh, E. Guarr, C. Xu, R. M. Sankaran, and J. N. Renner, "Catalyst-free, highly selective synthesis of ammonia from nitrogen and water by a plasma electrolytic system," *Science advances*, vol. 5, no. 1, eaat5778, 2019.

[52] D. Bao, Q. Zhang, F.-L. Meng, H.-X. Zhong, M.-M. Shi, Y. Zhang, J.-M. Yan, Q. Jiang, and X.-B. Zhang, "Electrochemical reduction of n2 under ambient conditions for artificial n2 fixation and renewable energy storage using n2/nh3 cycle," *Advanced materials*, vol. 29, no. 3, p. 1 604 799, 2017.

[53] Y. Yao, S. Zhu, H. Wang, H. Li, and M. Shao, "A spectroscopic study on the nitrogen electrochemical reduction reaction on gold and platinum surfaces," *Journal of the American Chemical Society*, vol. 140, no. 4, pp. 1496–1501, 2018.

[54] M.-M. Shi, D. Bao, B.-R. Wulan, Y.-H. Li, Y.-F. Zhang, J.-M. Yan, and Q. Jiang, "Au sub-nanoclusters on tio2 toward highly efficient and selective electrocatalyst for n2 conversion to nh3 at ambient conditions," *Advanced Materials*, vol. 29, no. 17, p. 1 606 550, 2017.

[55] T. K. Sau and C. J. Murphy, "Room temperature, high-yield synthesis of multiple shapes of gold nanoparticles in aqueous solution," *Journal of the American Chemical Society*, vol. 126, no. 28, pp. 8648–8649, 2004.

[56] B. Nikoobakht and M. A. El-Sayed, "Preparation and growth mechanism of gold nanorods (nrs) using seed-mediated growth method," *Chemistry of Materials*, vol. 15, no. 10, pp. 1957–1962, 2003.

[57] M. A. Mahmoud, D. O'Neil, and M. A. El-Sayed, "Hollow and solid metallic nanoparticles in sensing and in nanocatalysis," *Chemistry of Materials*, vol. 26, no. 1, pp. 44–58, 2014.

[58] J. A. Bordley and M. A. El-Sayed, "Enhanced electrocatalytic activity toward the oxygen reduction reaction through alloy formation: Platinum–silver alloy nanocages," *The Journal of Physical Chemistry C*, vol. 120, no. 27, pp. 14 643–14 651, 2016.

[59] T. Oshikiri, K. Ueno, and H. Misawa, "Selective dinitrogen conversion to ammonia using water and visible light through plasmon-induced charge separation," *Angewandte Chemie International Edition*, vol. 55, no. 12, pp. 3942–3946, 2016.

[60] P. L. Stiles, J. A. Dieringer, N. C. Shah, and R. P. Van Duyne, "Surface-enhanced raman spectroscopy," *Annu. Rev. Anal. Chem.*, vol. 1, pp. 601–626, 2008.

[61] S. R. Panikkanvalappil, M. A. Mackey, and M. A. El-Sayed, "Probing the unique dehydration-induced structural modifications in cancer cell dna using surface enhanced raman spectroscopy," *Journal of the American Chemical Society*, vol. 135, no. 12, pp. 4815–4821, 2013.

[62] R. A. Kydd and R. P. Cooney, "Raman spectra of adsorbed ammonia on carbon-overlayered silver electrodes," *Journal of the Chemical Society, Faraday Transactions 1: Physical Chemistry in Condensed Phases*, vol. 79, no. 12, pp. 2887–2897, 1983.

[63] J.-L. Dong, X.-H. Li, L.-J. Zhao, H.-S. Xiao, F. Wang, X. Guo, and Y.-H. Zhang, "Raman observation of the interactions between nh4+, so42-, and h2o in supersaturated (nh4) 2so4 droplets," *The Journal of Physical Chemistry B*, vol. 111, no. 42, pp. 12 170–12 176, 2007.

[64] F. Zhou, L. M. Azofra, M. Ali, M. Kar, A. N. Simonov, C. McDonnell-Worth, C. Sun, X. Zhang, and D. R. MacFarlane, "Electro-synthesis of ammonia from nitrogen at ambient temperature and pressure in ionic liquids," *Energy & Environmental Science*, vol. 10, no. 12, pp. 2516–2520, 2017.

[65] Z. Zhang, L. Xin, and W. Li, "Supported gold nanoparticles as anode catalyst for anion-exchange membrane-direct glycerol fuel cell (aem-dgfc)," *international journal of hydrogen energy*, vol. 37, no. 11, pp. 9393–9401, 2012.

[66] J. Nash, X. Yang, J. Anibal, J. Wang, Y. Yan, and B. Xu, "Electrochemical nitrogen reduction reaction on noble metal catalysts in proton and hydroxide exchange membrane electrolyzers," *Journal of The Electrochemical Society*, vol. 164, no. 14, F1712–F1716, 2017.

[67] L. Suo, O. Borodin, T. Gao, M. Olguin, J. Ho, X. Fan, C. Luo, C. Wang, and K. Xu, "Water-in-salt electrolyte enables high-voltage aqueous lithium-ion chemistries," *Science*, vol. 350, no. 6263, pp. 938–943, 2015.

[68] M. Nazemi and M. A. El-Sayed, "Electrochemical synthesis of ammonia from n2 and h2o under ambient conditions using pore-size-controlled hollow gold nanocatalysts with tunable plasmonic properties," *The journal of physical chemistry letters*, vol. 9, no. 17, pp. 5160–5166, 2018.

[69] M. Nazemi, S. R. Panikkanvalappil, and M. A. El-Sayed, "Enhancing the rate of electrochemical nitrogen reduction reaction for ammonia synthesis under ambient conditions using hollow gold nanocages," *Nano Energy*, vol. 49, pp. 316–323, 2018.

[70] G. I. Waterhouse, G. A. Bowmaker, and J. B. Metson, "The thermal decomposition of silver (i, iii) oxide: A combined xrd, ft-ir and raman spectroscopic study," *Physical Chemistry Chemical Physics*, vol. 3, no. 17, pp. 3838–3845, 2001.

[71] L. Polavarapu, D. Zanaga, T. Altantzis, S. Rodal-Cedeira, I. Pastoriza-Santos, J. Perez-Juste, S. Bals, and L. M. Liz-Marzan, "Galvanic replacement coupled to seeded growth as a route for shape-controlled synthesis of plasmonic nanorattles," *Journal of the American Chemical Society*, vol. 138, no. 36, pp. 11 453–11 456, 2016.

[72] B. Goris, L. Polavarapu, S. Bals, G. Van Tendeloo, and L. M. Liz-Marzán, "Monitoring galvanic replacement through three-dimensional morphological and chemical mapping," *Nano letters*, vol. 14, no. 6, pp. 3220–3226, 2014.

[73] L. Shi, L. Liang, J. Ma, F. Wang, and J. Sun, "Enhanced photocatalytic activity over the ag 2 o–gc 3 n 4 composite under visible light," *Catalysis Science & Technology*, vol. 4, no. 3, pp. 758–765, 2014.

[74] M. Xu, L. Han, and S. Dong, "Facile fabrication of highly efficient g-c3n4/ag2o heterostructured photocatalysts with enhanced visible-light photocatalytic activity," *ACS applied materials & interfaces*, vol. 5, no. 23, pp. 12 533–12 540, 2013.

[75] Q. Qin, T. Heil, M. Antonietti, and M. Oschatz, "Single-site gold catalysts on hierarchical n-doped porous noble carbon for enhanced electrochemical reduction of nitrogen," *Small Methods*, vol. 2, no. 12, p. 1 800 202, 2018.

[76] J. Zheng, Y. Lyu, M. Qiao, R. Wang, Y. Zhou, H. Li, C. Chen, Y. Li, H. Zhou, S. Wang, *et al.*, "Photoelectrochemical synthesis of ammonia on the aerophilic-hydrophilic heterostructure with 37.8% efficiency," *Chem*, vol. 5, no. 3, pp. 617–633, 2019.

[77] X. Wang, W. Wang, M. Qiao, G. Wu, W. Chen, T. Yuan, Q. Xu, M. Chen, Y. Zhang, X. Wang, *et al.*, "Atomically dispersed au1 catalyst towards efficient electrochemical synthesis of ammonia," *Science bulletin*, vol. 63, no. 19, pp. 1246–1253, 2018.

[78] J. Yang, Y. Guo, W. Lu, R. Jiang, and J. Wang, "Emerging applications of plasmons in driving co2 reduction and n2 fixation," *Advanced Materials*, vol. 30, no. 48, p. 1 802 227, 2018.

[79] F. Akagi, T. Matsuo, and H. Kawaguchi, "Dinitrogen cleavage by a diniobium tetrahydride complex: Formation of a nitride and its conversion into imide species," *Angewandte Chemie International Edition*, vol. 46, no. 46, pp. 8778–8781, 2007.

[80] T. Shima, S. Hu, G. Luo, X. Kang, Y. Luo, and Z. Hou, "Dinitrogen cleavage and hydrogenation by a trinuclear titanium polyhydride complex," *Science*, vol. 340, no. 6140, pp. 1549–1552, 2013.

[81] J. Wang, L. Yu, L. Hu, G. Chen, H. Xin, and X. Feng, "Ambient ammonia synthesis via palladium-catalyzed electrohydrogenation of dinitrogen at low overpotential," *Nature communications*, vol. 9, no. 1, pp. 1–7, 2018.

[82] K. Kim, S. J. Lee, D.-Y. Kim, C.-Y. Yoo, J. W. Choi, J.-N. Kim, Y. Woo, H. C. Yoon, and J.-I. Han, "Electrochemical synthesis of ammonia from water and nitrogen: A lithium-mediated approach using lithium-ion conducting glass ceramics," *ChemSusChem*, vol. 11, no. 1, pp. 120–124, 2018.

[83] P. Wang, F. Chang, W. Gao, J. Guo, G. Wu, T. He, and P. Chen, "Breaking scaling relations to achieve low-temperature ammonia synthesis through lih-mediated nitrogen transfer and hydrogenation," *Nature chemistry*, vol. 9, no. 1, p. 64, 2017.

[84] N. Lazouski, Z. J. Schiffer, K. Williams, and K. Manthiram, "Understanding continuous lithium-mediated electrochemical nitrogen reduction," *Joule*, vol. 3, no. 4, pp. 1127–1139, 2019.

[85] J. K. Nørskov, T. Bligaard, B. Hvolbæk, F. Abild-Pedersen, I. Chorkendorff, and C. H. Christensen, "The nature of the active site in heterogeneous metal catalysis," *Chemical Society Reviews*, vol. 37, no. 10, pp. 2163–2171, 2008.

[86] O. Zandi and T. W. Hamann, "Determination of photoelectrochemical water oxidation intermediates on haematite electrode surfaces using operando infrared spectroscopy," *Nature chemistry*, vol. 8, no. 8, p. 778, 2016.

[87] Y. Deng and B. S. Yeo, "Characterization of electrocatalytic water splitting and co2 reduction reactions using in situ/operando raman spectroscopy," *Acs Catalysis*, vol. 7, no. 11, pp. 7873–7889, 2017.

[88] Y. Deng, A. D. Handoko, Y. Du, S. Xi, and B. S. Yeo, "In situ raman spectroscopy of copper and copper oxide surfaces during electrochemical oxygen evolution reaction: Identification of cuiii oxides as catalytically active species," *ACS Catalysis*, vol. 6, no. 4, pp. 2473–2481, 2016.

[89] M. Nazemi and M. A. El-Sayed, "The role of oxidation of silver in bimetallic gold–silver nanocages on electrocatalytic activity of nitrogen reduction reaction," *The Journal of Physical Chemistry C*, vol. 123, no. 18, pp. 11 422–11 427, 2019.

[90] M. Nazemi, J. Padgett, and M. C. Hatzell, "Acid/base multi-ion exchange membrane-based electrolysis system for water splitting," *Energy Technology*, vol. 5, no. 8, pp. 1191–1194, 2017.

[91] M. Nazemi, L. Soule, M. Liu, and M. A. El-Sayed, "Ambient ammonia electrosynthesis from nitrogen and water by incorporating palladium in bimetallic gold–silver nanocages," *Journal of The Electrochemical Society*, vol. 167, no. 5, p. 054 511, 2020.

[92] M. Mahmoud and M. El-Sayed, "Metallic double shell hollow nanocages: The challenges of their synthetic techniques," *Langmuir*, vol. 28, no. 9, pp. 4051–4059, 2012.

[93] C.-W. Yi, K Luo, T Wei, and D. Goodman, "The composition and structure of pd-au surfaces," *The Journal of Physical Chemistry B*, vol. 109, no. 39, pp. 18 535–18 540, 2005.

[94] G.-T. Fu, C. Liu, Q. Zhang, Y. Chen, and Y.-W. Tang, "Polyhedral palladium–silver alloy nanocrystals as highly active and stable electrocatalysts for the formic acid oxidation reaction," *Scientific reports*, vol. 5, p. 13 703, 2015.

[95] L. Nahar, A. A. Farghaly, R. J. A. Esteves, and I. U. Arachchige, "Shape controlled synthesis of au/ag/pd nanoalloys and their oxidation-induced self-assembly into electrocatalytically active aerogel monoliths," *Chemistry of Materials*, vol. 29, no. 18, pp. 7704–7715, 2017.

[96] J. Chen, B. Wiley, J. McLellan, Y. Xiong, Z.-Y. Li, and Y. Xia, "Optical properties of pd- ag and pt- ag nanoboxes synthesized via galvanic replacement reactions," *Nano letters*, vol. 5, no. 10, pp. 2058–2062, 2005.

[97] S. Verma, S. Lu, and P. J. Kenis, "Co-electrolysis of co 2 and glycerol as a pathway to carbon chemicals with improved technoeconomics due to low electricity consumption," *Nature Energy*, vol. 4, no. 6, p. 466, 2019.

[98] S. Z. Andersen, V. Čolić, S. Yang, J. A. Schwalbe, A. C. Nielander, J. M. McEnaney, K. Enemark-Rasmussen, J. G. Baker, A. R. Singh, B. A. Rohr, *et al.*, "A rigorous electrochemical ammonia synthesis protocol with quantitative isotope measurements," *Nature*, vol. 570, no. 7762, pp. 504–508, 2019.

[99] B. H. Suryanto, H.-L. Du, D. Wang, J. Chen, A. N. Simonov, and D. R. MacFarlane, "Challenges and prospects in the catalysis of electroreduction of nitrogen to ammonia," *Nature Catalysis*, vol. 2, no. 4, pp. 290–296, 2019.

[100] L. F. Greenlee, J. N. Renner, and S. L. Foster, *The use of controls for consistent and accurate measurements of electrocatalytic ammonia synthesis from dinitrogen*, 2018.

[101] C. Li, T. Wang, Z.-J. Zhao, W. Yang, J.-F. Li, A. Li, Z. Yang, G. A. Ozin, and J. Gong, "Promoted fixation of molecular nitrogen with surface oxygen vacancies on plasmon-enhanced tio2 photoelectrodes," *Angewandte Chemie International Edition*, vol. 57, no. 19, pp. 5278–5282, 2018.

[102] A. D. Fortes, I. G. Wood, D. Alfè, E. R. Hernández, M. J. Gutmann, and H. A. Sparkes, "Structure, hydrogen bonding and thermal expansion of ammonium carbonate monohydrate," *Acta Crystallographica Section B: Structural Science, Crystal Engineering and Materials*, vol. 70, no. 6, pp. 948–962, 2014.

[103] P. Arora, I. Sharma, A. Hoadley, S. Mahajani, and A. Ganesh, "Remote, small-scale,'greener'routes of ammonia production," *Journal of Cleaner Production*, vol. 199, pp. 177–192, 2018.

[104] S. Linic, P. Christopher, and D. B. Ingram, "Plasmonic-metal nanostructures for efficient conversion of solar to chemical energy," *Nature materials*, vol. 10, no. 12, pp. 911–921, 2011.

[105] G. Schrauzer and T. Guth, "Photolysis of water and photoreduction of nitrogen on titanium dioxide," *Journal of the American Chemical Society*, vol. 99, no. 22, pp. 7189–7193, 2002.

[106] G. N. Schrauzer, "Photoreduction of nitrogen on tio 2 and tio 2-containing minerals," in *Energy Efficiency and Renewable Energy Through Nanotechnology*, Springer, 2011, pp. 601–623.

[107] H. Hirakawa, M. Hashimoto, Y. Shiraishi, and T. Hirai, "Photocatalytic conversion of nitrogen to ammonia with water on surface oxygen vacancies of titanium dioxide," *Journal of the American Chemical Society*, vol. 139, no. 31, pp. 10 929–10 936, 2017.

[108] O. Rusina, O. Linnik, A. Eremenko, and H. Kisch, "Nitrogen photofixation on nanostructured iron titanate films," *Chemistry–A European Journal*, vol. 9, no. 2, pp. 561–565, 2003.

[109] O. Rusina, A. Eremenko, G. Frank, H. P. Strunk, and H. Kisch, "Nitrogen photofixation at nanostructured iron titanate films," *Angewandte Chemie International Edition*, vol. 40, no. 21, pp. 3993–3995, 2001.

[110] X. Chen, N. Li, Z. Kong, W.-J. Ong, and X. Zhao, "Photocatalytic fixation of nitrogen to ammonia: State-of-the-art advancements and future prospects," *Materials Horizons*, vol. 5, no. 1, pp. 9–27, 2018.

[111] H. Li, J. Shang, Z. Ai, and L. Zhang, "Efficient visible light nitrogen fixation with biobr nanosheets of oxygen vacancies on the exposed 001 facets," *Journal of the American Chemical Society*, vol. 137, no. 19, pp. 6393–6399, 2015.

[112] J. Li, H. Li, G. Zhan, and L. Zhang, "Solar water splitting and nitrogen fixation with layered bismuth oxyhalides," *Accounts of chemical research*, vol. 50, no. 1, pp. 112–121, 2017.

[113] X. Xue, R. Chen, H. Chen, Y. Hu, Q. Ding, Z. Liu, L. Ma, G. Zhu, W. Zhang, Q. Yu, *et al.*, "Oxygen vacancy engineering promoted photocatalytic ammonia synthesis on ultrathin two-dimensional bismuth oxybromide nanosheets," *Nano letters*, vol. 18, no. 11, pp. 7372–7377, 2018.

[114] S. V. Boriskina, H. Ghasemi, and G. Chen, "Plasmonic materials for energy: From physics to applications," *Materials Today*, vol. 16, no. 10, pp. 375–386, 2013.

[115] K. Saha, S. S. Agasti, C. Kim, X. Li, and V. M. Rotello, "Gold nanoparticles in chemical and biological sensing," *Chemical reviews*, vol. 112, no. 5, pp. 2739–2779, 2012.

[116] W. A. Murray and W. L. Barnes, "Plasmonic materials," *Advanced materials*, vol. 19, no. 22, pp. 3771–3782, 2007.

[117] C. Clavero, "Plasmon-induced hot-electron generation at nanoparticle/metal-oxide interfaces for photovoltaic and photocatalytic devices," *Nature Photonics*, vol. 8, no. 2, p. 95, 2014.

[118] M. Ali, F. Zhou, K. Chen, C. Kotzur, C. Xiao, L. Bourgeois, X. Zhang, and D. R. MacFarlane, "Nanostructured photoelectrochemical solar cell for nitrogen reduction using plasmon-enhanced black silicon," *Nature communications*, vol. 7, no. 1, pp. 1–5, 2016.

[119] C. Hu, X. Chen, J. Jin, Y. Han, S. Chen, H. Ju, J. Cai, Y. Qiu, C. Gao, C. Wang, *et al.*, "Surface plasmon enabling nitrogen fixation in pure water through a dissociative mechanism under mild conditions," *Journal of the American Chemical Society*, vol. 141, no. 19, pp. 7807–7814, 2019.

[120] M. K. Gupta, T. König, R. Near, D. Nepal, L. F. Drummy, S. Biswas, S. Naik, R. A. Vaia, M. A. El-Sayed, and V. V. Tsukruk, "Surface assembly and plasmonic properties in strongly coupled segmented gold nanorods," *Small*, vol. 9, no. 17, pp. 2979–2990, 2013.

[121] T. Oshikiri, K. Ueno, and H. Misawa, "Plasmon-induced ammonia synthesis through nitrogen photofixation with visible light irradiation," *Angewandte Chemie International Edition*, vol. 53, no. 37, pp. 9802–9805, 2014.

[122] J. Yang, Y. Guo, R. Jiang, F. Qin, H. Zhang, W. Lu, J. Wang, and J. C. Yu, "High-efficiency "working-in-tandem" nitrogen photofixation achieved by assembling plasmonic gold nanocrystals on ultrathin titania nanosheets," *Journal of the American Chemical Society*, vol. 140, no. 27, pp. 8497–8508, 2018.

[123] E. Shi, Y. Gao, B. P. Finkenauer, A. H. Coffey, L. Dou, *et al.*, "Two-dimensional halide perovskite nanomaterials and heterostructures," *Chemical Society Reviews*, vol. 47, no. 16, pp. 6046–6072, 2018.

[124] H. Cheng, B. Huang, and Y. Dai, "Engineering biox (x= cl, br, i) nanostructures for highly efficient photocatalytic applications," *Nanoscale*, vol. 6, no. 4, pp. 2009–2026, 2014.

[125] A. Kafizas, S. A. Parry, A. V. Chadwick, C. J. Carmalt, and I. P. Parkin, "An exafs study on the photo-assisted growth of silver nanoparticles on titanium dioxide thin-films and the identification of their photochromic states," *Physical Chemistry Chemical Physics*, vol. 15, no. 21, pp. 8254–8263, 2013.

[126] D. B. Akolekar, S. K. Bhargava, and G. Foran, "Exafs studies on gold nanoparticles over novel catalytic materials," *Radiation Physics and Chemistry*, vol. 75, no. 11, pp. 1948–1952, 2006.

[127] Y. Chao, P. Zhou, N. Li, J. Lai, Y. Yang, Y. Zhang, Y. Tang, W. Yang, Y. Du, D. Su, *et al.*, "Ultrathin visible-light-driven mo incorporating in2o3–znin2se4 z-scheme nanosheet photocatalysts," *Advanced Materials*, vol. 31, no. 5, p. 1 807 226, 2019.

[128] C. Xu, P. Qiu, L. Li, H. Chen, F. Jiang, and X. Wang, "Bismuth subcarbonate with designer defects for broad-spectrum photocatalytic nitrogen fixation," *ACS applied materials & interfaces*, vol. 10, no. 30, pp. 25 321–25 328, 2018.

[129] D. P. Kumar, E. H. Kim, H. Park, S. Y. Chun, M. Gopannagari, P Bhavani, D. A. Reddy, J. K. Song, and T. K. Kim, "Tuning band alignments and charge-transport properties through mose2 bridging between mos2 and cadmium sulfide for enhanced hydrogen production," *ACS applied materials & interfaces*, vol. 10, no. 31, pp. 26 153–26 161, 2018.

[130] M. Nazemi and M. A. El-Sayed, "Plasmon-enhanced photo (electro) chemical nitrogen fixation under ambient conditions using visible light responsive hybrid hollow au-ag2o nanocages," *Nano Energy*, vol. 63, p. 103 886, 2019.

[131] X. Yang, J. Nash, J. Anibal, M. Dunwell, S. Kattel, E. Stavitski, K. Attenkofer, J. G. Chen, Y. Yan, and B. Xu, "Mechanistic insights into electrochemical nitrogen reduction reaction on vanadium nitride nanoparticles," *Journal of the American Chemical Society*, vol. 140, no. 41, pp. 13 387–13 391, 2018.

[132] N. Zhang, A. Jalil, D. Wu, S. Chen, Y. Liu, C. Gao, W. Ye, Z. Qi, H. Ju, C. Wang, *et al.*, "Refining defect states in w18o49 by mo doping: A strategy for tuning n2 activation towards solar-driven nitrogen fixation," *Journal of the American Chemical Society*, vol. 140, no. 30, pp. 9434–9443, 2018.